Dopaminergic modulation of prefrontal cortex subpopulations

By

Caitlin Miya Vander Weele

B.S. Psychology

University of Michigan, 2011

Submitted to the Department of Brain and Cognitive Sciences

In partial fulfillment of the requirements for the degree of

DOCTOR OF PHILOSOPHY IN NEUROSCIENCE

at the

MASSACHUSETTS INSTITUTE OF TECHNOLOGY

~~April 2018~~ [June 2018]

Signature of Author: Signature redacted

Department of Brain and Cognitive Sciences

April 13, 2018

Certified by: Signature redacted

Kay M. Tye, Ph.D.

Associate Professor, Picower Institute, Department of Brain and Cognitive Sciences

Thesis Supervisor

Accepted by: Signature redacted

Matthew A. Wilson, Ph.D.

Sherman Fairchild Professor of Neuroscience

Director of Graduate Education for Brain and Cognitive Sciences

Dopaminergic modulation of prefrontal cortex subpopulations

By

Caitlin M. Vander Weele

Submitted to the Department of Brain and Cognitive Sciences on March 30, 2018

in partial fulfillment of the requirements for the degree of

DOCTOR OF PHILOSOPHY IN NEUROSCEINCE

Abstract

Despite abundant evidence that dopamine modulates medial prefrontal cortex (mPFC) activity to mediate diverse behavioral functions, the precise circuit computations remain elusive. One potentially unifying theoretical model by which dopamine can modulate functions from working memory to schizophrenia is that dopamine serves to increase the signal-to-noise ratio in mPFC neurons, where neuronal activity conveying sensory information (signal) are amplified relative to spontaneous firing (noise). To connect theory to biology, we lack direct evidence for dopaminergic modulation of signal-to-noise in neuronal firing patterns *in vivo* and a mechanistic explanation of how such computations would be transmitted downstream to instruct specific behavioral functions. Here, we demonstrate that dopamine increases signal-to-noise ratio in mPFC neurons projecting to the dorsal periaqueductal gray (dPAG) during the processing of an aversive stimulus. First, using electrochemical approaches, we reveal the precise time course of tail pinch-evoked dopamine release in the mPFC. Second, we show that dopamine signaling in the mPFC biases behavioral responses to punishment-predictive stimuli, rather than reward-predictive cues. Third, in contrast to the well-characterized mPFC-NAc projection, we show that activation of mPFC-dPAG neurons is sufficient to drive place avoidance and defensive behaviors. Fourth, to determine the natural dynamics of individual mPFC neurons, we performed single-cell projection-defined microendoscopic calcium imaging to reveal a robust preferential excitation of mPFC-dPAG, but not mPFC-NAc, neurons to aversive stimuli. Finally, photostimulation of VTA dopamine terminals in the mPFC revealed an increase in signal-to-noise ratio in mPFC-dPAG neuronal activity during the processing of aversive, but not rewarding stimuli. Together, these data unveil the utility of dopamine in the mPFC to effectively filter sensory information in a valence-specific manner.

Thesis Supervisor: Kay M. Tye
Title: Associate Professor of Neuroscience
Picower Institute of Learning and Memory
Department of Brain and Cognitive Sciences

To my mom, sister, and brother
You are my world

Acknowledgements

"*We love ourselves in the things we love. We find ourselves there, too*" ~ Kristin Martz

To my teachers and mentors.

My Ph.D. mentor, **Dr. Kay M. Tye**, thank you for your relentless belief in my potential over the past 7 years. I never could have imagined the things I would accomplish under your supervision and support. You have grown a stronger, smarter, and more confident woman. To my committee members, **Drs. Li-Huei Tsai, Matt Wilson,** and **Ki Goosens**, for leaving me encouraged and determined to continue this path after every meeting. You've made me the best scientist I can be. My undergraduate mentors, **Drs. Brandon Aragona** and **Shanna Harkey-Resendez**, for nourishing my mind and soul at all stages over the past decade.

To my team, for sticking with me.

To my partner in crime, **Cody Siciliano**. From hooking up imaging animals to evenings over Bookers, you've inspired, comforted, and encouraged me during some of my most difficult times. Thank you for dragging me over the finish line— while making me laugh the entire way. **Gillian Matthews,** you are such a rock star. You've taught me tenacity and aesthetic. Thanks for patching an insane number of cells over an equally insane number of conditions. To all of my other co-authors, **Edward Nieh, Praneeth Namburi, Isabella Espinel, Ehsan Izadmehr, Anna Beyeler, Romy Wichmann, Eyal Kimchi, Nancy Padilla, Tony Burgos-Robles, Evelien Schut,** and **Kay Tye**, I couldn't be prouder of the things we've accomplished together. Thank you for the deepest parts of my heart.

To my friends, for believing in, supporting, and inspiring me.

All members of the Tye lab, past & present. In particular, **Cody Siciliano, Craig Wildes, Anna Beyeler, Gwendolyn Calhoon, Edward Nieh, Praneeth Namburi,** and **Gillian Matthew**s – for my being my Boston family. **Craig Wildes**, someday you will miss me and appreciate the value of the beanbag. Special thanks to favorite bartenders, **Tony Yohe** and **Curt Hancock,** and the entire staff at Catalyst, for feeding me and making me smile after long lab days. My Ph.D. role models and confidants, **Steve Ramirez, Emily Doucette,** and **Pedro Tsividis**. My digital support system, my science Twitter community and Interstellate contributors and sponsors, for helping me find and cultivate a passion for science communication.

To my family, for everything. Always.

My parents, **Kitty Flaherty** and **Rick Vander Weele** for raising me to follow my dreams and supporting my decisions at every step. I am incomplete without my siblings **Meagan** and **Eric Vander Weele**, who give me identity and strength. To others in my extended family, **Ken Smith** and **Patrick Metzger**. Finally, to **Pasquale D'Silva** for teaching me to dream bigger, love deeper, and laugh harder. I love you.

I would also like to thank all of the BCS and animal care staff for providing support in various ways, both big and small.

Finally, to all the rodents who have given their lives to further our understanding of the brain.

Table of Contents

Chapter 1: Background
Functions of the prefrontal cortex 10
Prefrontal anatomy 12
The mesolimbic dopamine system 13
Dopaminergic mechanisms of action in the prefrontal cortex 16
Dopaminergic modulation of prefrontal function and physiology 18
Summary 20

Chapter 2: Aversive stimuli increase dopamine in the prefrontal cortex and activation of dopamine terminals in the prefrontal cortex biases behavior towards aversion
Introduction 23
Results 24
Experimental procedures 42
Summary 54
Author contributions 54

Chapter 3: Prefrontal projections to the striatum and periaqueductal gray are distinct and differentially encode and promote reward and aversion
Introduction 55
Results 57
Experimental procedures 85
Summary 99
Author contributions 99

Chapter 4: Dopamine enhances neuronal responses to aversive stimuli in periaqueductal gray-projecting prefrontal neurons and inhibits striatal-projecting neurons
Introduction 101
Results 102
Experimental procedures 131
Summary 149
Author contributions 150

Chapter 5: Conclusions - Dopamine in the prefrontal cortex enhances signal-to-noise for aversive stimuli via projections to the periaqueductal gray
Summary 151
Discussion 151
Caveats 156
Implications for mental health 158

Chapter 6: References 159

List of Figures

Figure 1. Peer-reviewed studies of dopamine in appetitive and aversive motivation 22

Figure 2. Dopamine terminals are densest in deep layers of the prefrontal cortex 25

Figure 3. LC inactivation does not alter catecholamine release in the mPFC in response to tail pinch 28

Figure 4. VTA DA inhibition attenuates catecholamine release in response to tail pinch 32

Figure 5. Activation of dopamine terminals in the mPFC does not support real-time or conditioned place preference / aversion 35

Figure 6. Activation of dopamine terminals in the mPFC biases behavior towards aversion during competitive stimulus presentations 38

Figure 7. Putative connection strength of mPFC projections to downstream targets 58

Figure 8. mPFC-dPAG and mPFC-NAc projector populations are distinct 61

Figure 9. Collateralization of mPFC-NAc and mPFC-dPAG projector subpopulations 64

Figure 10. Activation of mPFC-NAc neurons does not support real-time or conditioned placed preference / aversion 66

Figure 11. Activation of mPFC-dPAG neurons supports real-time or conditioned placed aversion 69

Figure 12. Activation of mPFC-dPAG neurons increases marble burying 73

Figure 13. Activation of mPFC terminals in the dPAG evokes marble burying 76

Figure 14. mPFC-NAc neurons exhibit heterogeneous responses to rewarding and aversive stimuli, while mPFC-dPAG neurons preferentially respond to aversive stimuli 80

Figure 15. *In vivo* calcium imaging re-analyzed with a background subtracted ROI approach 83

Figure 16. mPFC-dPAG and mPFC-NAc projectors have different electrophysiological properties 103

Figure 17. Dopamine inhibits NAc-projectors via D2-receptors 107

Figure 18. mPFC-dPAG projectors largely do not express dopamine receptors 110

Figure 19. Investigation of VTA projections to the dPAG for simultaneous epifluorescent imaging in mPFC-dPAG neurons and excitation of VTA^{DA} terminals ……...113

Figure 20. Stimulation of dopamine terminals in the mPFC increase calcium transient amplitude and decreases frequency in dPAG-projectors ……..115

Figure 21. *Ex vivo* latency validation for head-fixed electrophysiological recordings with phototagging ……118

Figure 22. mPFC-dPAG neurons are excited to airpuff ……121

Figure 23. Representative mPFC-dPAG units ……..125

Figure 24. Dopamine selectively enhances mPFC-dPAG responses to airpuff ……127

Figure 23. Dopamine increase baseline firing rate, but not stimulus-evoked responses in photoinhibited mPFC neurons ……129

Chapter 1

Background

Functions of the prefrontal cortex

The medial prefrontal cortex (mPFC) is a heterogeneous brain region implicated in a diverse range of cognitive and behavioral functions— including attention, decision-making, working memory, long-term memory, emotional control, inhibitory control, motivation, among many others (Arnsten, 2009; Bechara et al., 2000; Miller and Cohen, 2001; Ridderinkhof et al., 2004). While these functions may appear disparate, they all are related to cognitive control, or the ability to coordinate emotions and actions to support internally held goals (Miller and Cohen, 2001). Lesions of the mPFC result in robust deficits in performance in tasks that require one to adapt behavior to contexts or tasks with dynamic or unexpected rules (Dias et al., 1996a, 1996b, 1997; Gregoriou et al., 2014; Milner, 1963; Rossi et al., 2007; Wilkinson et al., 1997). While many brain regions, neurotransmitter systems, and neural circuits support goal-directed behavior, the mPFC is well positioned to act as an anatomical hub coordinating adaptive behavioral output.

At a basic level, successfully seeking rewards and avoiding punishments is critical for survival, and a defining characteristic of adaptive behavior. To mediate these behaviors, neural systems must integrate internal motivational states with external information to orchestrate approach and avoidance of rewarding and aversive stimuli, respectively. For example, an animal engaging in foraging behavior for food must constantly evaluate its environment for potential threats, which necessitate a transition from reward-seeking to threat avoidance. While the mPFC is not critical for basic stimulus-driven unconditioned behaviors, such as those found in subcortical structures like the periaqueductal gray (Assareh et al., 2016; Bandler and Carrive,

1988; Bandler et al., 1985a, 1985b; Carrive et al., 1987; Deng et al., 2016; Meyer et al., 2017; Tovote et al., 2016; Zhang et al., 1990) and hypothalamus (Anand and Brobeck, 1951; Betley et al., 2015; Burton et al., 1976; Jennings et al., 2015; Nieh et al., 2015, 2016), the mPFC plays a substantial role in deciphering ambiguous situations. In the example above, the foraging animal must not only perceive the environmental threat, but also evaluate its importance in relation to its ongoing efforts (e.g., How far away is the threat? How severe is the threat? How hungry am I? When will I be able to forage again?).

There is substantial evidence supporting a crucial role of the mPFC in decision-making in the context of risk and reward, particularly in situations involving competition (i.e., when both rewarding and aversive stimuli are simultaneously present) (Bechara et al., 1994, 2005; Botvinick et al., 2004; Burgos-Robles et al., 2017; Mansouri et al., 2009; Milham et al., 2001). In rodents, pharmacological inactivation of the mPFC produces deficits in the coordination of reward-seeking and threat avoidance (Sangha et al., 2014; Sierra-Mercado et al., 2011). In humans, mPFC activity is modulated by the proximity of threat (Mobbs et al., 2007) suggesting a role in coordinating behavioral coping strategies. Not surprisingly, mPFC neuronal activity is robustly modulated by motivationally-relevant stimuli— including reward-delivery, reward-expectation, omission of reward, pain, and pain-predictive cues (for review, see: Euston et al., 2012)— and mPFC activity is highly correlated with aspects of reward- and fear-motivated behavioral output (Burgos-Robles et al., 2009, 2013). In competitive situations, neurons encoding different information compete for representation and subsequent expression of behavior. However, it is still unknown if these neural responses carrying competing valence-defined information can be mapped onto specific mPFC circuits, what modulates their competitive interactions, and how the competition results are translated into behavior.

Prefrontal anatomy

Consistent with the idea that the mPFC is crucial for cognitive control, this neocortical region is most developed in primates and animals that have elaborate behavioral repertoires (Adolphs, 2009; Dunbar, 2009; Kerney et al., 2017; Noonan et al., 2018). Understanding the mPFC and its functional relevance relies on an understanding of its complex macro- and micro-anatomical organization. The mPFC is often subdivided into four distinct subregions – medial precentral / second frontal area (PrCM / Fr2), the anterior cingulate cortex (ACC), the prelimbic cortex (PL), and infralimbic cortex (IL) – based on afferent / efferent connections and cytoarchitectural differences (Heidbreder and Groenewegen, 2003). However based on afferent and efferent connectivity the ventral portion of the PL and dorsal part of the IL are often combined and referred to as the ventral medial PFC (vmPFC). For simplicity, the remainder of this manuscript will use vmPFC synonymously with mPFC, as manipulations and recordings in this region often contained the ventral aspect of the PL and dorsal aspect of the IL.

The local mPFC network consists of excitatory, glutamatergic pyramidal cells and inhibitory GABAergic interneurons, representing ~80-90% and 10-20% of the population, respectively (Gabbott et al., 1997, 2005). Traditionally it has been thought that pyramidal neurons comprise the majority of the long-range projection neurons in the mPFC while GABAergic interneurons powerfully regulate their activity locally. However, recently long-range GABAergic projections have also been characterized (Lee et al., 2014a). Both of these populations can be further dissected based on functional, laminar, morphological, and molecular properties (Gabbott et al., 1997, 2005).

Similar to other cortical structures, the mPFC is laminarly organized (Douglas and Martin, 2004; Gabbott et al., 2005; Kritzer and Goldman-Rakic, 1995). The mPFC receives diverse sensory and limbic afferent connections (Hoover and Vertes, 2007) arriving predominantly in superficial Layers 1 and 2/3 (Douglas and Martin, 2004; Romanski et al.,

1999a, 1999b). mPFC afferent connections are equally robust projecting to cortical and subcortical brain regions (Gabbott et al., 2005; Groenewegen et al., 1997; Heidbreder and Groenewegen, 2003; Sesack et al., 1989; Vertes, 2004). Long-range efferent projections originate mainly from the deep layers (Layers 5 and 6), while projections to other cortical areas are located in superficial Layer 2/3 (DeFelipe and Fariñas, 1992; Douglas and Martin, 2004; Gabbott et al., 2005). Notably, downstream connections appear to be densest to brain regions involved in emotional and autonomic control— including the amygdala, ventral striatum, insula, hypothalamus, periaqueductal gray, habenula, and midline thalamic structures (Gabbott et al., 2005; Heidbreder and Groenewegen, 2003; Vertes, 2004). Through this dense interconnectivity, the mPFC is thought to exert top-down processing of rewarding and aversive stimuli and subsequent emotional regulation and control of actions. However precise, causal investigations of these mPFC outputs are still lacking. It is unclear which specific mPFC connections convey valence-defined information and under what conditions.

The mesolimbic dopamine system

The mPFC also maintains reciprocal connectivity with a wide range of neuromodulatory systems known to be involved in adaptive responses to rewarding and aversive events— including the midbrain dopamine system (Gabbott et al., 2005; Heidbreder and Groenewegen, 2003; Vertes, 2004). Dopamine neurons originate in both the ventral tegmental area (VTA, also known as A10) and substantia nigra pars compacta (SNc, also known as A9) (for review, see: Björklund and Dunnett, 2007), which are both anatomically and functionally distinct populations. While VTA dopamine neurons regulate motivation and encode reward expectation, substantia nigra neurons appear to be more involved in motor functions via connections to the dorsal striatum / caudate putamen (Berridge, 2007; Björklund and Dunnett, 2007; Michel et al., 2016; Schultz et al., 1997; York, 1973). VTA dopamine neurons send dense projections to the ventral

striatum (including the nucleus accumbens [NAc]) and sparser projections to the mPFC, amygdala, and hippocampus (for review, see: Haber and Fudge, 1997).

VTA dopamine neurons transmit signals in two modes: 1) "tonic" characterized by a consistent, pacemaker-like 2-5 Hz firing rate, and 2) "phasic" characterized by transient bursts of high frequency 10-20 Hz firing lasting 100-500 ms (Bunney et al., 1991; Grace and Bunney, 1984, 1984; Grace et al., 2007). Tonic firing maintains a consistent basal, extracellular level of dopamine in downstream targets. On the other hand, bursting rapidly and transiently increases dopamine levels, estimated to be ~100 μM in the synapse (Garris and Wightman, 1994; Grace et al., 2007), termed 'phasic dopamine release' or dopamine 'transients' (for review, see: Robinson et al., 2003). Dopamine release in target regions modulates the activity of specific populations of neurons expressing postsynaptic dopamine receptors (see below for more detailed discussion) (Dreyer et al., 2010, 2016). However, it is important to note that bursting (i.e., dopamine neuron action potentials) may not evoke dopamine neurotransmission considering dopamine terminals are influenced by local inputs and autoreceptors (Cachope and Cheer, 2014; Cachope et al., 2012; Cragg and Rice, 2004; Dreyer and Hounsgaard, 2013; Rice and Cragg, 2004; Zhang and Sulzer, 2004). As such, it is important to use multidisciplinary approaches to appreciate the complex and dynamic interactions between somatic activity, dopamine release, and reuptake.

Phasic dopamine neuron activity and phasic dopamine release have been studied extensively in the context of reward (Berridge, 2007; Berridge and Robinson, 1998; Fields et al., 2007; Grace et al., 2007; Ikemoto, 2007; Robinson et al., 2003; Schultz, 2013; Schultz et al., 1997; Volkow et al., 2017; Wise, 2006, 2008). In a seminal study by Schultz and colleagues (1997), dopamine neurons were found to change their activity based on reward expectation. Here, dopamine neurons increased their firing to unexpected reward delivery, but shifted this response to cues that predict reward delivery after pairing. Further, VTA dopamine neurons

exhibited a decrease in firing if an expected reward (i.e., predicted by a conditioned stimulus) was omitted. Together, these neurons have been described as encoding "reward prediction error" (RPE) by signaling discrepancies between expected and received reward. As such, RPEs provide a mechanism for learning the outcomes of predictive stimuli and updating their internal representations when the magnitude or valence of their predicted outcomes are altered. Considering this, and dopamine's role in other appetitive motivational functions, VTA dopamine has been extensively studied in the context of reward – particularly through its connections with the striatum (Berridge, 2007; Berridge and Robinson, 1998; Hamid et al., 2016; Howe et al., 2013; Niv, 2007; Phillips et al., 2003; Salamone and Correa, 2012).

There is considerable debate over dopamine's role in the processing of aversive stimuli. As previously mentioned, several theories have suggested that phasic dopamine responses primarily encode reward-related events— including food reward, water reward, social targets, sex, and drugs of abuse (for review, see: Berridge, 2007; Berridge and Robinson, 1998; Fields et al., 2007; Robinson et al., 2003; Salamone and Correa, 2012; Schultz et al., 1997). Further, consistent with the reward prediction hypothesis, some studies report inhibition of dopamine activity in response to aversive events (Cohen et al., 2012; Roitman et al., 2008; Schultz et al., 1997; Ungless et al., 2004). However, dopamine responses have also been reported to various salient and aversive stimuli— including surprising events, stress, pain, and fear-predictive cues (Badrinarayan et al., 2012; Brischoux et al., 2009; Budygin et al., 2012; Horvitz, 2000; Mantz et al., 1989; Matsumoto and Hikosaka, 2009; McCutcheon et al., 2012; Salamone and Correa, 2012). As a result, new theories of dopamine function have suggested roles in alerting (Bromberg-Martin et al., 2010), invigoration of ongoing behaviors (Niv, 2007; Salamone et al., 2007; da Silva et al., 2018), or encoding the value of work (Hamid et al., 2016) (for review, see: Salamone and Correa, 2018; Schultz et al., 2017).

It remains unclear whether reward-encoding dopaminergic signals recorded in denser terminal regions, like the striatum, are also transmitted to regions like the mPFC. Heterogeneity observed within the VTA might result from distinct dopamine neuron subpopulations defined by projection target. Indeed, growing evidence supports distinct behavioral roles of VTA dopamine subpopulations depending on their ascending forebrain projection (e.g., "projection-defined") (Gunaydin et al., 2014; Kim et al., 2016; Lammel et al., 2011, 2012; Roeper, 2013). This notion is anatomically supported by the finding that the majority of VTA dopamine neurons do not collateralize and send independent, non-overlapping ascending projections to target regions (Albanese and Minciacchi, 1983; Fallon, 1981). These projection-defined VTA dopamine subpopulations maintain unique molecular signatures (Bannon and Roth, 1983; Bannon et al., 1981; Lammel et al., 2008), electrophysiological properties (Chiodo et al., 1984; Lammel et al., 2008), anatomical locations (Lammel et al., 2012), afferent connectivity (Lammel et al., 2012), and responses to valence-defined stimuli (see below for discussion) (Abercrombie et al., 1989; Badrinarayan et al., 2012; Bassareo et al., 2002; Kim et al., 2016; Lammel et al., 2011; Mantz et al., 1989).

Dopaminergic mechanisms of action

In the mPFC, dopaminergic terminals contact both pyramidal neurons (Goldman-Rakic et al., 1989; Séguéla et al., 1988; Zhang et al., 2010) and GABAergic interneurons (Verney et al., 1990). Postsynaptically, dopamine exerts its effects on neuronal activity via two main types of receptors— D1-type (including D1 and D5) and D2-type (including D2, D3, and D4) (de Almeida et al., 2008; Lidow et al., 1991; Santana and Artigas, 2017; Seamans and Yang, 2004; Sesack and Bunney, 1989). Both D1 and D2 sub-types are G-protein-coupled receptors, exerting slow, metabotropic modulation of postsynaptic cells (for review, see: Seamans and Yang et al., 2004). Activation of D1 receptors in the mPFC exerts excitatory effects through

sodium (Na+), potassium (K+), and calcium (Ca2+) currents (González-Burgos et al., 2002; Gorelova and Yang, 2000; Henze et al., 2000; Yang and Seamans, 1996; Yang et al., 1996). In contrast, activation of mPFC D2 receptors exerts an inhibitory effect through the modulation of glutamaterigic receptors and Na+ conductances (Gorelova and Yang, 2000; Gulledge and Jaffe, 1998, 2001). In both cases, activation of receptors can produce long-lasting (~30 min) changes in excitability (Gorelova and Yang, 2000; Gulledge and Jaffe, 1998, 2001; Seamans et al., 2001a, 2001b).

In the mouse mPFC, D1 and D2 receptors are expressed in both pyramidal neurons and GABAergic interneurons (Gaspar et al., 1995; Lee et al., 2014b; Vincent et al., 1993). D1 receptors are primarily located on the dendritic spines and shafts of pyramidal neurons and on the axon terminals of putative GABAergic interneurons (Bergson et al., 1995a, 1995b; Muly et al., 1998). Further, D1 immunoreactivity is present on axon terminals that form asymmetric (i.e., putative glutamatergic) synapses with mPFC dendrites (Paspalas and Goldman-Rakic, 2005), suggesting that dopamine may influence the excitability of mPFC neurons both directly and indirectly. In pyramidal neurons, D1 and D2 receptors are expressed in Layer 5 (Gaspar et al., 1995; Gee et al., 2012; Santana et al., 2009; Seong and Carter, 2012) – one of the major output layers of the mPFC. D1 receptors are expressed in 20% Layer 5 neurons, whereas 25% express D2 (Santana et al., 2009). Dopamine has been reported by some investigators to increase (Henze et al., 2000; Penit-Soria et al., 1987; Yang and Seamans, 1996) and by others to decrease (Bunney and Aghajanian, 1976; Gulledge and Jaffe, 1998; Sesack and Bunney, 1989) the excitability mPFC neurons – suggesting differential modulation by dopamine depending on mPFC cell-type or projection target. However, the relatively low expression level of dopamine receptors in mPFC projection neurons suggest that a larger portion of Layer 5 pyramidal neurons are not directly modulated by dopamine, but may be subject to dopaminergic modulation of presynaptic inputs (Seamans et al., 2001b; Tritsch and Sabatini, 2012).

Dopaminergic modulation of prefrontal functions and physiology

Although dopaminergic terminals in the mPFC are sparse (Descarries et al., 1987) and correspondingly, dopamine release is lower compared to other forebrain regions, such as the NAc (Garris and Wightman, 1994), dopamine has a profound impact on mPFC-dependent cognition and behavior. The role of dopamine in the medial prefrontal cortex (mPFC) has been linked to basic functions such as working memory (Brozoski et al., 1979; Sawaguchi and Goldman-Rakic, 1991; Zahrt et al., 1997) and attention (Chudasama and Robbins, 2004; Granon et al., 2000), and is also associated with disease states such as schizophrenia (Creese et al., 1976; Nolan et al., 2004; Okubo et al., 1997a, 1997b; Rolls et al., 2008; Weinberger et al., 1988a, 1988b), depression (Di Chiara et al., 1999; Tanda et al., 1994), and stress/anxiety (Abercrombie et al., 1989; Arnsten, 2009; Finlay et al., 1995; Gunaydin et al., 2014; Mizoguchi et al., 2000; Thierry et al., 1976). However, effects of mPFC dopamine on top-down regulation of rewarding and aversive stimuli remain controversial given several lines of paradoxical reports.

In an important series of studies by Lammel and colleagues, they demonstrated that projection-defined VTA dopamine neurons differentially respond to rewarding and aversive stimuli. More specifically, these studies have suggested that VTA dopamine neurons projecting to the NAc encode aspects of reward or reinforçement, while VTA dopamine neurons projecting to the mPFC may encode aspects of aversion (Lammel et al., 2011, 2012). First, Lammel and colleagues (2011) show that enhanced synaptic plasticity onto VTA dopamine neurons following rewarding and aversive events depends on projection-defined subpopulations. *In vitro* AMPA/NMDA ratios, as a measure of synaptic strength, are enhanced in VTA dopamine neurons projecting to the NAc medial shell after cocaine exposure – a highly rewarding and reinforcing experience (Calipari et al., 2015, 2016; Deroche et al., 1999; Nomikos and Spyraki, 1988; Roberts et al., 1977). In contrast, aversive stimulus experience — formalin injection into the paw (Dubuisson and Dennis, 1977) – did not change AMPA/NMDA ratios in NAc medial

shell-projecting VTA dopamine neurons. The opposite pattern of results was observed in VTA dopamine neurons projecting to the mPFC: synaptic plasticity was enhanced following aversive experience but not after rewarding experience (Lammel et al., 2011).

Measurements of neurotransmitter release and neuronal activity show the mPFC dopamine pathway is activated by both rewarding (Ahn and Phillips, 1999; Bassareo et al., 2002; Ellwood et al., 2017; St Onge et al., 2012) and aversive stimuli (Abercrombie et al., 1989; Kim et al., 2016; Mantz et al., 1989; Thierry et al., 1976). However, several studies have suggested that the mPFC dopamine system is preferentially sensitive to aversive stimuli. For example, in addition to the aforementioned Lammel studies (2011, 2012), dopamine neurotransmission measured by *in vivo* microdialysis is robustly elevated following tail pinch, compared to release in the dorsal and ventral portions of the striatum, despite significantly denser striatal innervation (Abercrombie et al., 1989). Further, bulk calcium signals from dopamine axon terminals recorded simultaneously in the mPFC and NAc with *in vivo* fiber photometry show divergent responsivity to rewarding and aversive stimuli (Kim et al., 2016). Here, VTA dopamine terminals in the NAc were activated by water reward and inhibited by tail shock, whereas terminals in the mPFC were activated by tail shock and not robustly responsive to water reward (Kim et al., 2016). Finally, *in vivo* electrophysiological recordings of putative mPFC- and NAc-projecting VTA dopamine neurons revealed preferential responsivity of the mesocortical pathway to tail pinch – with 65% exhibiting excitation and 25% inhibition – whereas NAc-projecting units were largely non-responsive (Mantz et al., 1989).

The impact of dopamine neurotransmission on reward- and aversion-motivated behaviors also suggests functional differences, although this is still debated and likely dependent on many factors including stress-levels, context, and stimulus characteristics. In a second study by Lammel and colleagues (2012) they show that activation of inputs onto VTA neurons projecting to either NAc or mPFC with optogenetics resulted in reinforcement and

aversion, respectively. Further, direct activation of VTA dopamine terminals in the mPFC has been shown to support conditioned place avoidance and promote anxiety-related behavior (Gunaydin et al., 2014) and destruction of dopaminergic innervation of the mPFC disrupts escape behavior (Sokolowski et al., 1994). Yet the role of mesocortical dopamine in aversive motivation remains controversial. For example, Ellwood and colleagues (2017) recently reported that neither phasic nor tonic optical activation of VTA dopamine axon terminals supports conditioned place preference / aversion (Ellwood et al., 2017), in contrast to Gunaydin and colleagues (2014). Popescu and colleagues (2016), show that activation of VTA DA terminals promotes stimulus-discrimination for reward-predictive cues, suggesting a role in reward-learning (Popescu et al., 2016). These seemingly contradictory reports fail to provide a cohesive understanding of the functional role of dopamine in the mPFC. Importantly, these studies do not explore dopaminergic modulation of competitive situations where both rewarding and aversive stimuli are simultaneously presented – which may profoundly impact the functional role of dopamine in the mPFC considering its importance to higher-order cognition and decision-making.

Summary

Dopamine neurotransmission from midbrain VTA dopamine neurons are critically involved in modulating neural circuits responsible for appetitive and aversive motivation. While the impact of dopamine release within the striatum has been extensively studied, particularly in the context of reward-related behaviors, the mesocortical pathway's role in motivation has been vastly understudied (**Figure 1**). Mounting evidence suggests that under certain conditions, the sensitivity of the mesocortical system to aversive stimuli may promote avoidance or escape behaviors. Further, considering mPFC neurons are responsive to both rewarding and aversive stimuli (Burgos-Robles et al., 2009, 2013; Euston et al., 2012), it is possible that mPFC neuronal

circuits encoding aversive or rewarding events are differentially modulated by dopamine, resulting in a vast array of computations and behavioral outcomes. Here we seek to identify the neural circuit mechanisms and environmental conditions in which dopamine modulates valence-encoding in the mPFC and subsequent behavioral output.

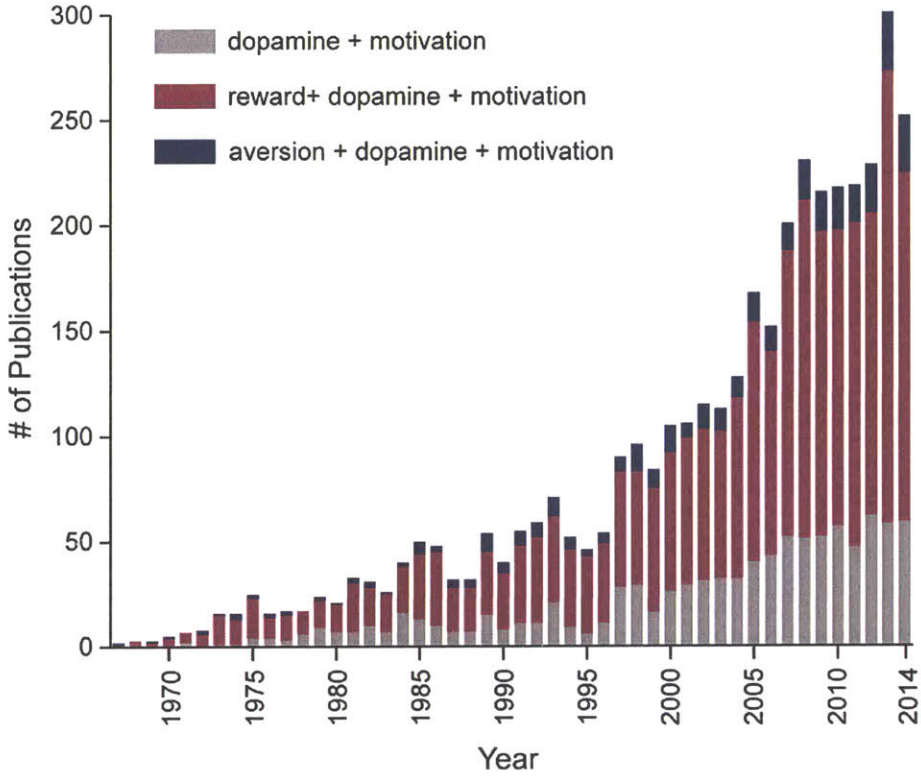

Figure 1. Peer-reviewed studies of dopamine in appetitive and aversive motivation.

Results of PubMed search, April 2015.

Chapter 2

Aversive stimuli increase dopamine in the prefrontal cortex and activation of dopamine terminals in the prefrontal cortex biases behavior towards aversion

Introduction

Aversive and stressful stimuli robustly increase dopamine release in the mPFC (Abercrombie et al., 1989; Thierry et al., 1976). However, the techniques used in these cardinal studies, lack temporal resolution and it remains unclear how noxious stimuli affect rapid dopamine release in the mPFC. As such, this slow time course does not allow us to determine whether dopamine is released in a time-locked manner (sub-second) or whether it is released in response to the slower stress response (minutes) following the aversive stimulus. Considering behaviorally-relevant stimuli are often discrete, aversive stimuli must rapidly evoke dopamine release in order to influence real-time behavioral responses. Recently, dopaminergic terminals in the mPFC were shown to respond to shock, while no change in activity was observed after receipt of a water reward using fiber photometry to measure calcium signals (Kim et al., 2016). However, increased axonal calcium is an indirect measure of neurotransmitter release and cannot dissociate dopamine release from other neurotransmitters that are co-released (Stuber et al., 2011; Tritsch and Sabatini, 2012) or assess rates of dopamine uptake. As such, methodological constraints have made it has been impossible to selectively study how dopamine neurotransmission within the mPFC may elicit aversive behavior.

Fast-scan cyclic voltammetry (FSCV) is an electrochemical technique that is capable of measuring "real-time" (i.e., 10 Hz) catecholamine release *in vivo*. While FSCV offers a direct measurement of catecholamine neurotransmission with precise temporal resolution, it is rarely used outside the NAc (for review, see: Robinson et al., 2003) (but see: Garris and Wightman,

1994; Garris et al., 1993; Matthews et al., 2016) due to difficulty in discriminating between norepinephrine and dopamine (Heien et al., 2003) – which has limited its application to brain regions like the mPFC which receive both dopaminergic and noradrenergic innervation. Thus, the time course and source of dopamine release in the mPFC upon aversive stimuli presentation is unknown. In this line of research, we will use electrochemical, optogenetic, pharmacological, and behavioral approaches to: 1) characterize the topography of catecholaminergic innervation in the mPFC, 2) record rapid dopamine signaling in the mPFC during aversive stimulation, 3) causally manipulate dopamine release in the mPFC to assess its impact on a variety of behaviors.

Results

To assess noradrenergic and dopaminergic terminal density in the mPFC, we injected a Cre-dependent virus carrying a fluorescent protein (eYFP or mCherry, counter balanced) into the VTA and locus coeruleus (LC) of transgenic DAT-Cre mice to selectively express two distinct fluorescent tags in VTA dopamine (DA) neurons and LC norepinephrine (NE) neurons (**Figure 2a-b**). After 8 weeks of incubation, terminal fluorescence was observed in the mPFC (**Figure 2c**) and quantified across cortical layers (**Figure 2d-e**). VTA-DA terminals were densest in deep layers (5 and 6), consistent with previous reports (Berger et al., 1976; Sesack et al., 1998; Zhang et al., 2010) while LC-NE terminals were densest in the superficial layers (**Figure 2f**). These data suggest that dopamine is acting in the deep layers of the mPFC.

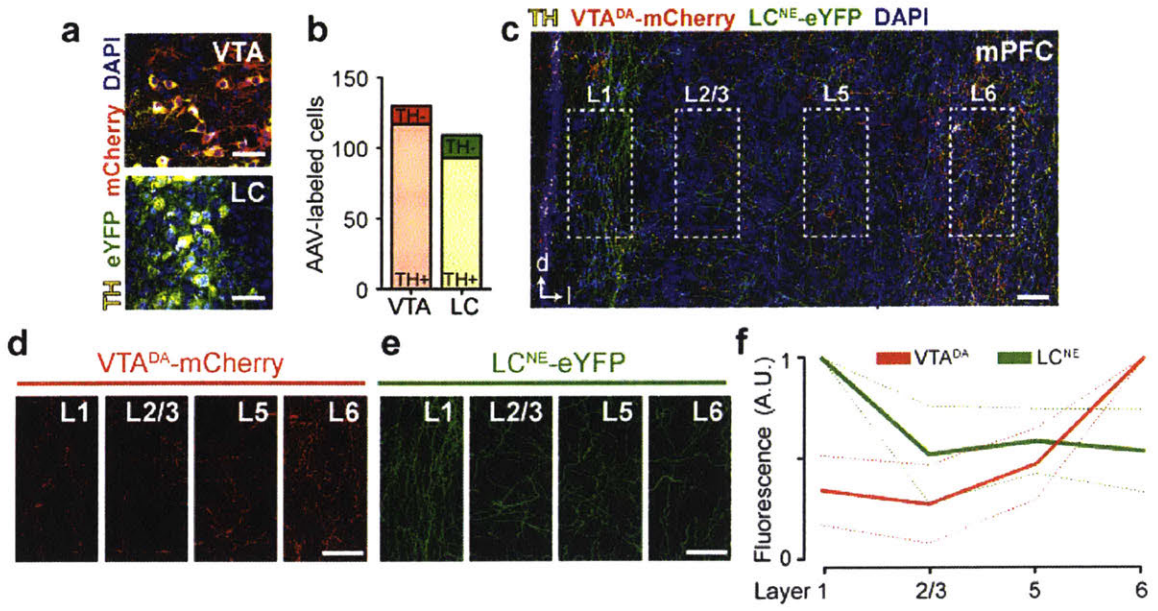

Figure 2. Dopamine terminals are densest in deep layers of the prefrontal cortex.

(a) Injection of viral constructs enabling Cre-dependent expression into the LC and VTA of TH::Cre mice (n = 3).

(b) Fluorescent labeling of TH positive (TH+) noradrenergic (NE) neurons in the LC and dopaminergic neurons in the VTA.

(c) Examination of VTA^{DA} and LC^{NE} fluorescent terminal labeling in the mPFC.

(d) VTA^{DA} terminals (from inset) across cortical layers in the prelimbic subregion of the mPFC.

(e) LC^{NE} terminals (from inset) across cortical layers in the prelimbic subregion of the mPFC.

(f) VTA^{DA} terminals were densest in the deep (5 and 6) layers of the mPFC, while LC^{NE} terminals were denser in superficial (1 and 2/3) layers.

To investigate the time course of dopamine release, we injected a viral vector enabling Cre-dependent expression of channelrhodopsin-2 (ChR2) in the VTA of transgenic tyrosine hydroxylase (TH)::Cre rats (Witten et al., 2011) and inserted carbon-fiber electrodes into the prelimbic subregion of the mPFC for *in vivo* FSCV measurements (**Figure 3a-c**). To convert recorded changes in current to changes in catecholamine concentration and to eliminate contributions from transient pH fluctuations, chemometric and principal component analyses were performed (**Figure 3d-f**) (Keithley and Wightman, 2011; Keithley et al., 2009; Vander Weele et al., 2014). Electrodes were aimed at the deep layers (5-6) where VTA dopaminergic terminals in the mPFC (VTA^{DA}-mPFC) were densest, compared to norepinephrine (NE) locus coeruleus (LC) terminals (**Figure 3g-h**) and secured in locations, which supported optically-evoked dopamine release upon stimulation of VTA^{DA} neurons (**Figure 3i-j**). To investigate how an aversive stimulus impacts rapid catecholamine release, we performed a 10 s tail pinch and observed a reliable catecholaminergic signal, which peaked just after tail pinch offset and lingered for ~40 s (**Figure 3l-n**). Given the relatively slow decay kinetics, our data are consistent with other reports suggesting that dopamine reuptake is slower in the mPFC than in the striatum (Cass and Gerhardt, 1995; Garris and Wightman, 1994; Garris et al., 1993; Käenmäki et al., 2010; Sesack et al., 1998) (**Figure 4c**). This is consistent with reports indicating that mesocortical dopamine neurons lack D2-type autoreceptors, which provide negative feedback and autoinhibit the activity of dopamine neurons (Bannon et al., 1981; Chiodo et al., 1984). In addition, dopamine transporter (DAT) expression is low (Sesack et al., 1998), resulting in slower dopamine reuptake in the mPFC.

Since norepinephrine release in the mPFC has also been reported using microdialysis in the minutes following an aversive stimulus (Finlay et al., 1995) we sought to eliminate LC norepinephrine contribution. To do this, we repeated this experiment immediately after infusing the sodium-channel blocker, tetrodotoxin (TTX) into the LC (**Figure 3k-o**) and observed

catecholamine release before and after LC inactivation were indistinguishable (**Figure 3p-r**). TTX microinfusions were co-injected with fast green for cover and spread visualization, which were inspected and noted during tissue sectioning. We speculate that the previously reported LC signal measured in the minutes following an aversive stimulus (Finlay et al., 1995) may have a slower onset and may be related to the subsequent stress response rather than the detection of the noxious stimulus itself.

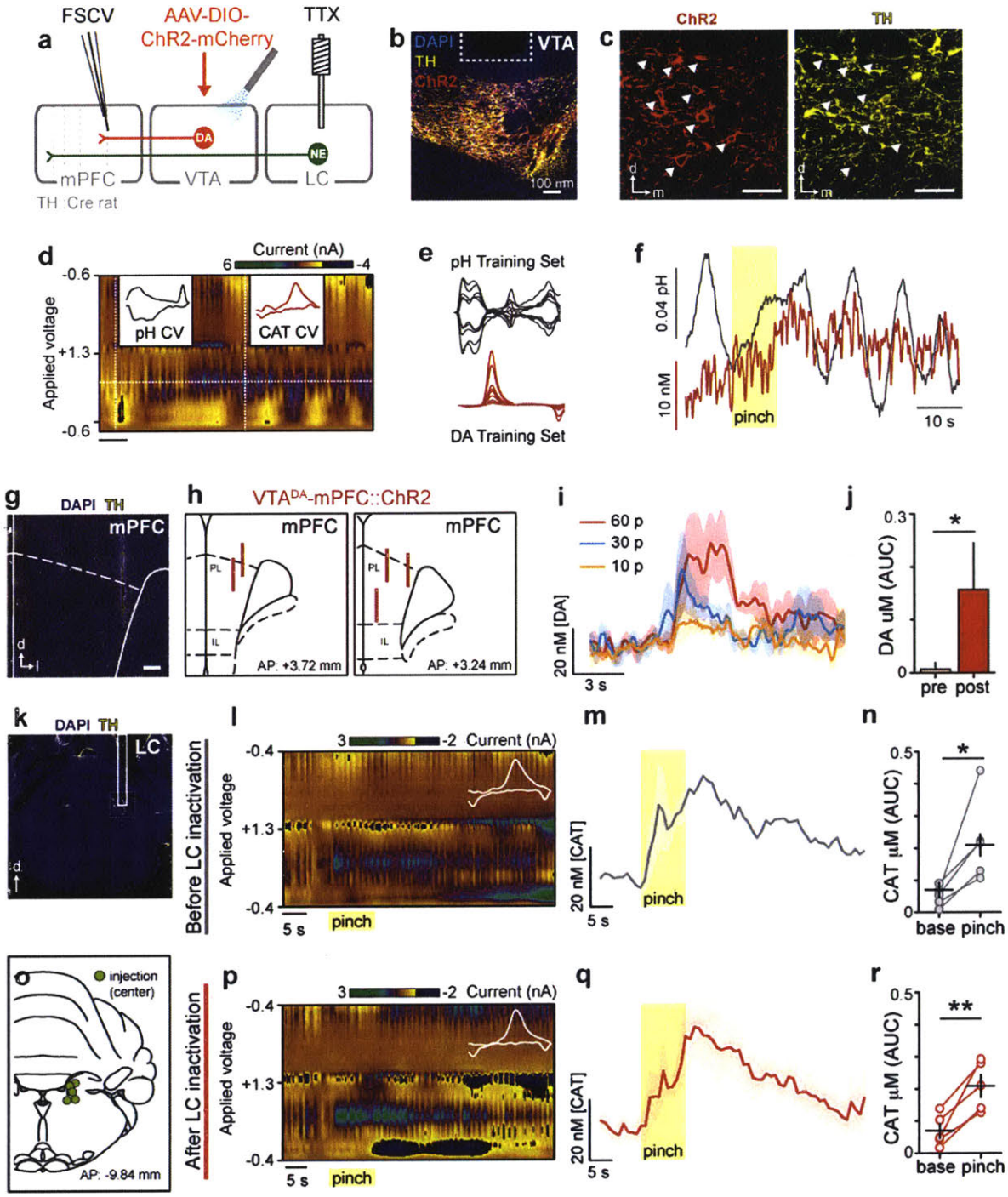
a
FSCV
AAV-DIO-
ChR2-mCherry
TTX
DA
NE
mPFC
VTA
LC
TH::Cre rat
b
DAPI
TH
ChR2
VTA
100 mm
c
ChR2
TH
d
m
d
Current (nA)
6
-4
-0.6
Applied voltage
+1.3
-0.6
pH CV
CAT CV
e
pH Training Set
DA Training Set
f
0.04 pH
10 nM
pinch
10 s
g
DAPI TH
mPFC
d
l
h
VTA^DA-mPFC::ChR2
mPFC
mPFC
PL
IL
AP: +3.72 mm
AP: +3.24 mm
i
60 p
30 p
10 p
20 nM [DA]
3 s
j
DA uM (AUC)
0.3
0
*
pre post
k
DAPI TH
LC
d
l
Before LC inactivation
Applied voltage
3
-2 Current (nA)
-0.4
+1.3
-0.4
5 s
pinch
m
20 nM [CAT]
5 s
pinch
n
CAT µM (AUC)
0.5
0
*
base pinch
o
injection
(center)
AP: -9.84 mm
After LC inactivation
p
Applied voltage
3
-2 Current (nA)
-0.4
+1.3
-0.4
5 s
pinch
q
20 nM [CAT]
5 s
pinch
r
CAT µM (AUC)
0.5
0
**
base pinch

Figure 3. LC inactivation does not alter catecholamine release in the mPFC in response to tail pinch.

(a) Schematic of strategy for differentiating dopamine and NE neurotransmission in the mPFC using fast-scan cyclic voltammetry (FSCV). VTA^{DA} neurons were selectively transduced with ChR2 in TH::Cre rats (n = 5). After incubation, rats were prepared for anesthetized FSCV recordings where an optical fiber was implanted over the VTA and a guide cannula was positioned over the LC for tetrodotoxin (TTX)-mediated pharmacological inhibition. A glass-encased carbon-fiber recording electrode was lowered into the mPFC for FSCV neurochemical measurements.

(b) 20x representative confocal image of ChR2-mCherry expression (red) in VTA^{DA} cell bodies (yellow = TH immunostaining). The optical fiber track is indicated by the white rectangle.

(c) 40x representative confocal image of ChR2-mCherry expression (left, red) in VTA^{DA} cell bodies (right, yellow = TH immunostaining).

(d) Overview of chemometric and principal component analyses of FSCV recordings to isolate catecholamine signals from pH shifts. Representative false color plot showing the presence of both basic pH shifts (left inset, pH cyclic voltammogram) and catecholamine release (right inset, catecholamine cyclic voltammogram).

(e) pH training set composed of acidic and basic pH voltammograms derived from *in vivo* and *in vitro* (flow cell) preparations. Dopamine training set composed of *in vivo* (optically- and electrically- evoked) and *in vitro* (flow cell) preparations.

(f) pH and dopamine traces derived from the representative recording using principal component regression

(g) Representative image of FSCV electrode track.

(h) Schematic representation of all recording electrode locations for ChR2 FSCV experiments.

(i) Evoked dopamine release in the mPFC following 20 Hz (60, 30, and 10 pulses) optical activation of VTA^{DA}::ChR2-mCherry cell bodies in the VTA.

(j) Optical activation (473 nm, 20 Hz, 60 pulses, 5 ms pulse-duration, 20 mW) of VTA^{DA}::ChR2 neurons evoked dopamine release in the mPFC (paired t-test, $t(3) = 3.72$, $p = 0.034$), ensuring FSCV recording electrodes were positioned in dopamine-rich locations.

(k) Representative image of guide cannula track positioned over LC^{NE} cell bodies (yellow = TH).

(l-n) When VTA^{DA} and LC^{NE} neurons were intact, tail pinch (10 s in duration) rapidly increased extracellular catecholamine concentration ([CAT]) release, as shown in **(l)** a representative false color plot, **(m)** average CAT trace, and **(n)** concentration quantification (paired t-test, $t(4) = 3.402$, $p = 0.027$). Color plot insets: representative cyclic voltammograms.

(o) Tetrodotoxin (TTX) + fast-green injection locations were viewed and recorded while tissue sectioning on a freezing microtome, prior to staining and mounting. The center of each injection was recorded. Rats that had injections but did not have spread covering the majority of the LC were excluded. Cannula implant locations were subsequently verified on a confocal microscope.

(p-q) After LC inactivation via intra-LC infusion of TTX, tail pinch evoked responses were maintained as shown in **(p)** a representative false color plot, **(q)** average CAT trace, and **(r)** concentration quantification (paired t-test, $t(4) = 5.249$, $p = 0.006$). Color plot insets: representative cyclic voltammograms.

Error bars indicate ±SEM. Scale bars (histology) = 50 um. "pre" = 5 s time period prior to stimulation onset; "post" = 5 s time period after stimulation onset.

Since both dopamine and norepinephrine can be released from multiple sources (Bjorklund & Dunnet et al., 2007), and it is possible that local modulation of LC^{NE}-mPFC terminals could occur, we sought to determine the primary source for the pinch-induced dopaminergic signal in the mPFC. To do this, we performed halorhodopsin (NpHR)-mediated photoinhibition of VTA^{DA} neurons during tail pinch (**Figure 4a-b**). We found that photoinhibition of VTA^{DA} neurons significantly attenuated the pinch-induced dopaminergic signal in the mPFC (**Figure 4d-f**). These data suggest that the majority of the pinch-evoked time-locked signal in the mPFC was mediated by dopamine release from VTA terminals.

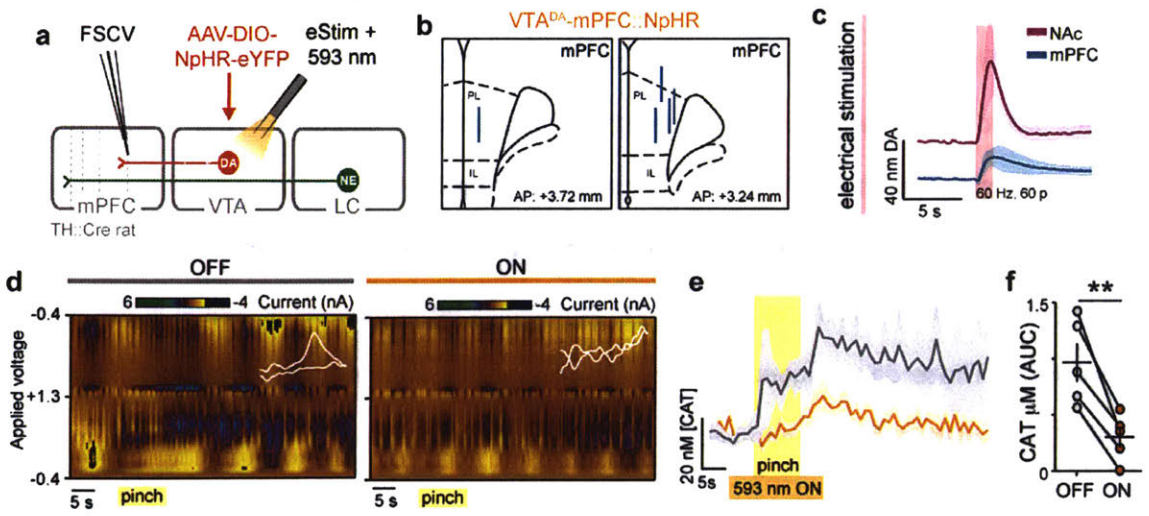

Figure 4. VTA DA inhibition attenuates catecholamine release in response to tail pinch.

(a) Schematic of strategy to verify dependence of pinch-evoked increases in CAT neurotransmission on VTA^{DA} neurons.

(b) Histologically verified FSCV recording electrode locations for NpHR experiments.

(c) Electrical stimulation (60 Hz, 60 pulses, 200 uA) of the dorsal VTA evoked distinct patterns of dopamine release in the NAc and mPFC.

(d) Representative false color plots showing tail pinch evoked CAT responses before (left) VTA^{DA} inhibition and during (right) transient VTA^{DA} inhibition surrounding the tail pinch (593 nm laser light, 20 s in duration) (n = 5) Color plot insets: representative cyclic voltammograms.

(e) Average CAT traces with (orange) and without (gray) optical inhibition of VTA^{DA} neurons.

(f) Optical inhibition of NpHR-expressing VTA^{DA} neurons attenuated tail pinch evoked CAT release in the mPFC (concentration quantification (paired t-test, $t(4) = 5.884$, $p = 0.004$)).

Error bars indicate ±SEM. Scale bars (histology) = 50 um. "pre" = 5 s time period prior to stimulation onset; "post" = 5 s time period after stimulation onset.

Next, given that dopamine is released in the mPFC following aversive stimuli, we wanted to explore the causal relationship between VTA^{DA}-mPFC and valence processing. To address this, we tested whether photostimulation of dopaminergic VTA terminals in the mPFC was sufficient to drive aversion. In TH::Cre rats, we injected a viral vector enabling Cre-dependent expression of ChR2 in the VTA and implanted optical fibers over the mPFC (**Figure 5a-b**). We did not find any detectable differences between ChR2- and eYFP-expressing rats in closed-loop real-time place avoidance (RTPA) (**Figure 5c-d**) or conditioned place aversion (CPA) assays (**Figure 5e-f**).

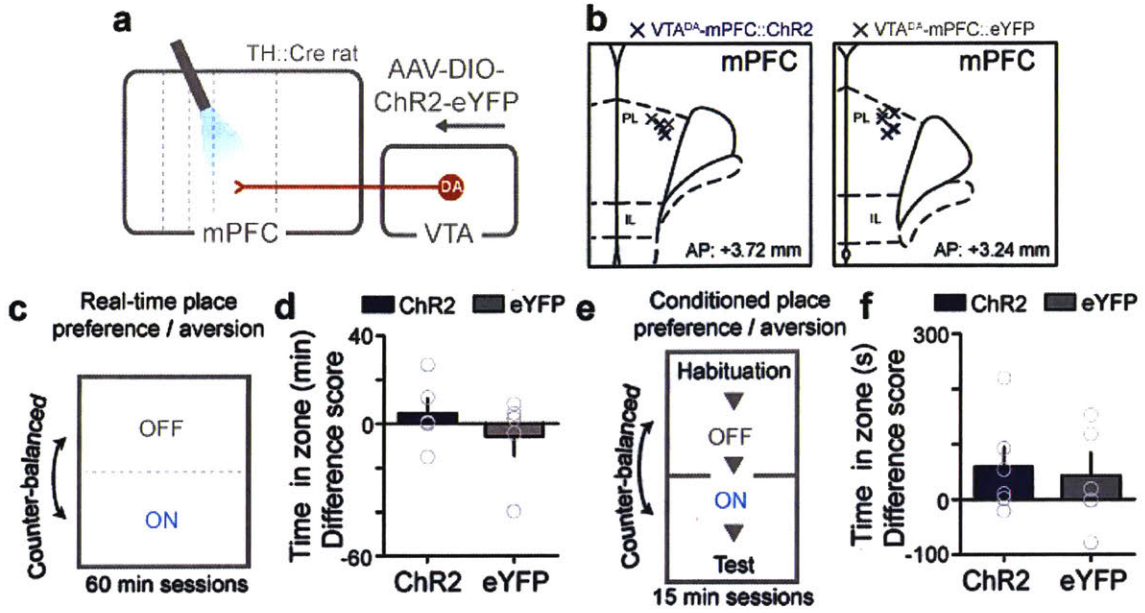

Figure 5. Activation of dopamine terminals in the mPFC does not support real-time or conditioned place preference / aversion.

(a) Schematic strategy for manipulating dopamine release in the mPFC. VTA^{DA} neurons were selectively transduced with ChR2 in TH::Cre rats.

(b) Guide cannulae were implanted over the mPFC for the insertion of an optical fiber for light delivery.

(c) Schematic of experimental design for real-time place preference/avoidance assays (RTPP/A). When rats entered the ON zone, laser light stimulation was activated for the duration of the time spent in the ON zone (20 Hz, 60 p, every 30 s, 20 mW of 473 nm for VTA^{DA}-mPFC experiments). When rats entered the OFF zone, light stimulation was terminated for the duration of time spent in the OFF zone.

(d) Optogenetic stimulation of VTA^{DA} neurons did not evoke real-time place avoidance or preference in VTA^{DA}-mPFC::ChR2 animals, compared to VTA^{DA}-mPFC::eYFP controls,

measured by difference score [minutes spent in the ON zone – OFF zone] (unpaired t-test, t(8) = 0.9337, p = 0.3778).

(e) Schematic of experimental design for all conditioned place preference/aversion assays (CPP/A). Day 1 consisted of a habituation period where time spent on each compartment of the arena was recorded. On days 2 and 3, a divider was placed in the middle of the chamber to separate the two compartments and rats received either no stimulation (OFF) or stimulation (ON) (20 Hz, 60 p, every 30 s, 20 mW of 473 nm for VTA^{DA}-mPFC experiments), counter-balanced across days. On day 4, the divider was removed and time spent in each compartment was recorded in the absence of stimulation (i.e., test day).

(f) Optogenetic stimulation of VTA^{DA} neurons did not support conditioned place aversion or preference in VTA^{DA}-mPFC::ChR2 animals, compared to VTA^{DA}-mPFC::eYFP controls, measured by difference score [minutes spent in the ON zone – OFF zone] (unpaired t-test, t(9) = 0.3192, p = 0.7569).

Error bars indicate ±SEM.

However, in RTPA and CPA there are no discrete stimuli presented, and in light of the model for dopaminergic involvement in enhancing signal-to-noise, we considered the potential importance of dopamine in enhancing neural activity in response to discrete, predictive cues. To test whether dopamine would bias behavioral responses to discrete cues predicting either punishment or reward, we used a recently described behavioral paradigm (Burgos-Robles et al., 2017). Here, rats expressing ChR2 in VTA^{DA} neurons (**Figure 6a-b**) and were trained on a stimulus competition behavioral paradigm (**Figure 6c-d**). First trained to associate auditory or visual cues (counter-balanced across subjects) with sucrose delivery to a nearby port (**Figure 6e**) and ChR2 and control eYFP subjects learned that the cue predicted reward delivery at the same rate – as measured by time spent in the sucrose port during the conditioned stimulus (**Figure 6f**). Next rats were trained to associate the alternative auditory or visual cues (counter-balanced across subjects) with footshock (**Figure 6g**). During discrimination sessions, and ChR2 and control eYFP subjects discriminated sucrose- and shock-predictive cues similarly, as measured by time spent in the sucrose port **(Figure 6h-i**) and time spent freezing (**Figure 6j-k**), a species-specific defensive reaction. Once rats learned to discriminate the cues predicting shock and sucrose by freezing or approaching the delivery port, respectively, we tested their behavioral responses to the competition of simultaneously-presented cues driving conflicting motivational outputs (**Figure 6d**). We found that photostimulation of VTA^{DA}-mPFC terminals (using empirically-determined optical parameters, **Figure 2i-j**) during the "competition" cues – wherein both shock-predictive and reward-predictive stimuli were co-presented – caused ChR2-expressing rats to spend significantly less time in the sucrose delivery port and more time freezing than eYFP controls (**Figure 6l-o**). There were no differences between groups during sucrose and shock only trials during competitions sessions (**Figure 6p-s**).

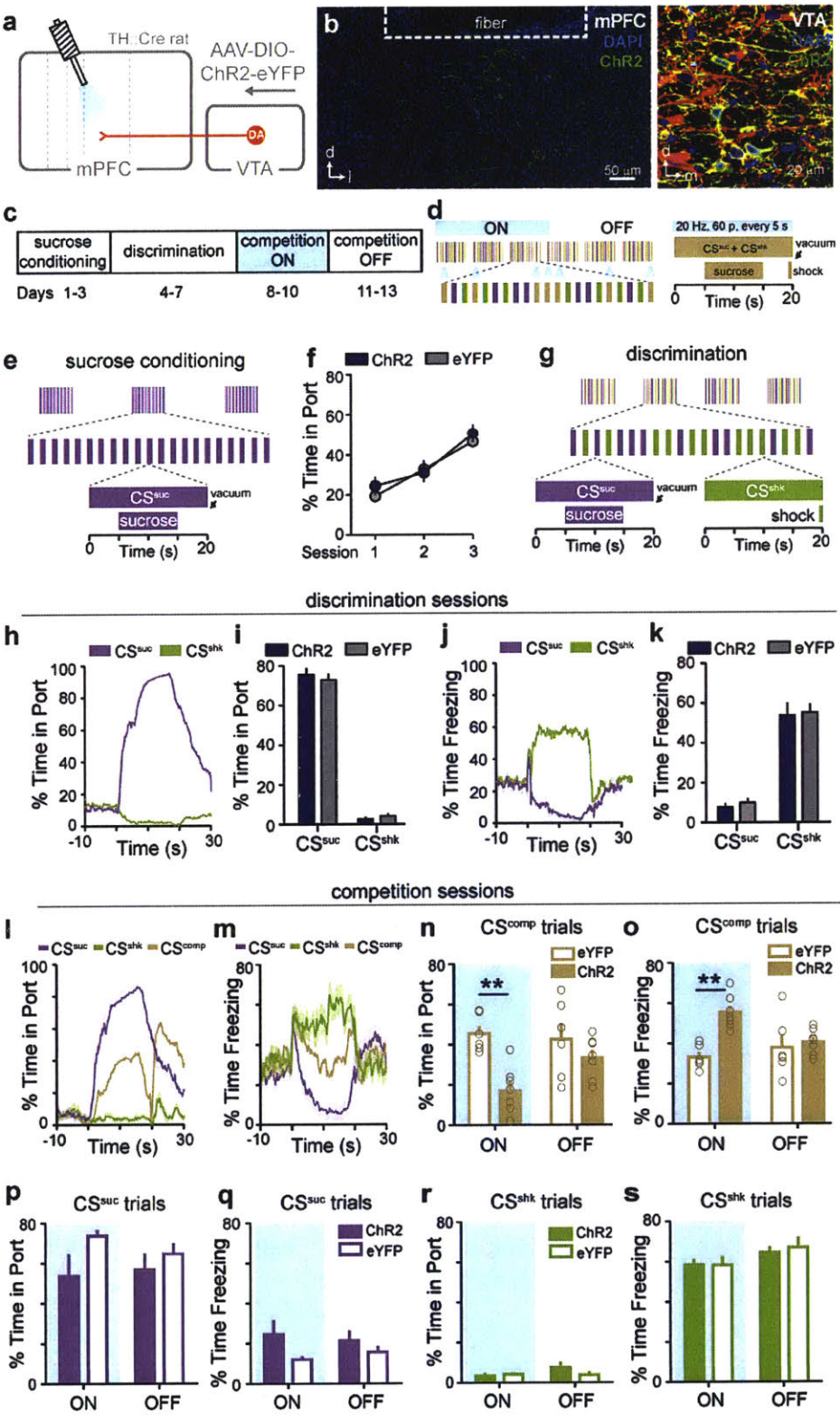
a
TH::Cre rat
AAV-DIO-ChR2-eYFP
DA
mPFC
VTA
b
fiber
mPFC
DAPI
ChR2
50 µm
VTA
29 µm
c
sucrose conditioning
discrimination
competition ON
competition OFF
Days 1-3
4-7
8-10
11-13
d
ON
OFF
20 Hz, 60 p. every 5 s
vacuum
sucrose
shock
Time (s)
e
sucrose conditioning
vacuum
sucrose
Time (s)
f
ChR2
eYFP
% Time in Port
Session
g
discrimination
vacuum
sucrose
shock
Time (s)
discrimination sessions
h
% Time in Port
Time (s)
i
ChR2
eYFP
% Time in Port
j
% Time Freezing
Time (s)
k
ChR2
eYFP
% Time Freezing
competition sessions
l
% Time in Port
Time (s)
m
% Time Freezing
Time (s)
n
trials
eYFP
ChR2
% Time in Port
ON
OFF
o
trials
eYFP
ChR2
% Time Freezing
ON
OFF
p
trials
% Time in Port
ON
OFF
q
trials
ChR2
eYFP
% Time Freezing
ON
OFF
r
trials
ChR2
eYFP
% Time in Port
ON
OFF
s
trials
% Time Freezing
ON
OFF

Figure 6. Activation of dopamine terminals in the mPFC biases behavior towards aversion during competitive stimulus presentations.

(a) Schematic of strategy for manipulating dopamine release in the mPFC.

(b) VTA^{DA} neurons were selectively transduced with ChR2 in TH::Cre rats and guide cannulae were implanted over the mPFC for insertion of an optical fiber for light delivery.

(c) Schematic of task used to examine dopamine modulation of reward and fear-motivated behaviors during competition.

(d) During competition trials (CS^{comp}), VTA^{DA} terminals were activated (473 nm, 20 Hz, 60 pulses, 5 ms pulse-duration, every 5 s, 18 mW) to assess the impact of dopamine signaling in the mPFC on behavior during competition. During "competition OFF", light was not delivered for the entire session to assess recovery.

(e) During sucrose training, a CS (light or tone, counterbalanced) predicted sucrose delivery (CS^{suc}). Sucrose was removed from the delivery port by vacuum if not collected.

(f) VTA^{DA}-mPFC::ChR2 rats and VTA^{DA}-mPFC::eYFP controls acquired sucrose conditioning similarly (two-way repeated measures ANOVA, $F_{2,22} = 0.7$, $p = 0.5090$).

(g) During discrimination, the alternative CS (light or tone, counterbalanced) was introduced and predicted foot shock (CS^{shk}).

(h) Average traces showing time spent in the sucrose port before, during, and after each CS presentation.

(i) Time spent in the sucrose port did not differ between VTA^{DA}-mPFC::ChR2 rats and VTA^{DA}-mPFC::eYFP controls during CS^{suc} or CS^{shk} (repeated measures two-way ANOVA, $F_{1,11} = 0.54$, $p = 0.4789$, Bonferroni multiple comparisons tests $p > 0.05$) presentation.

(j) Average traces showing time spent freezing before, during, and after each CS presentation.

(k) Time spent in the freezing did not differ between VTA^{DA}-mPFC::ChR2 rats and VTA^{DA}-

mPFC::eYFP controls during CS^{suc} or CS^{shk} (repeated measures two-way ANOVA, $F_{1,11} = 0.01$, $p = 0.9281$, Bonferroni multiple comparisons tests $p > 0.05$) presentation.

(l) Percent time spent in the reward port during the three trial types in the last competition ON session.

(m) Percent time spent freezing during the three trial types in the last competition ON session.

(n) During competition sessions, the average time spent in the reward port during CS^{comp} ON trials was lower in ChR2 rats (closed bars) compared with eYFP controls (open bars, repeated measures two-way ANOVA, $F_{1,11} = 8.13$, $p = 0.0157$, Bonferroni multiple comparisons tests $p < 0.05$).

(o) During competition sessions, the average time spent freezing during CS^{comp} ON trials was greater in ChR2 rats (closed bars) compared with eYFP controls (open bars, repeated measures two-way ANOVA, $F_{1,11} = 13.29$, $p = 0.0039$, Bonferroni multiple comparisons tests $p < 0.05$).

(p) During competition sessions, the average time spent in the reward port for CS^{suc} trials during ON sessions and CS^{suc} trials during OFF sessions did not differ between ChR2 rats (closed bars) and eYFP controls (open bars, repeated measures two-way ANOVA, $F_{1,11} = 0.82$, $p = 0.3845$). Note that during ON sessions, stimulation was only delivered during the CS^{comp} trials.

(q) Average time spent freezing for CS^{suc} trials during ON sessions and CS^{suc} trials during OFF sessions did not differ between ChR2 rats (closed bars) and eYFP controls (repeated measures two-way ANOVA, $F_{1,11} = 1.35$, $p = 1.35$).

(r) During competition sessions, the average time spent in the reward port for CS^{shk} trials during ON sessions and CS^{shk} trials during OFF sessions was not different between ChR2 (closed bars) and eYFP controls (open bars, repeated measures two-way ANOVA, $F_{1,11} = 0.94$, $p = 0.354$).

(s) During competition sessions, the average time spent freezing for CS^{shk} trials during ON sessions and CS^{shk} trials during OFF sessions was not different between ChR2 rats (closed bars) and eYFP controls (open bars, repeated measures two-way ANOVA, $F_{1,11} = 0.16$, $p = 0.6998$).

Error bars indicate ±SEM.

Experimental Procedures

General virus surgery

Specific subject/surgery details for each experiment are detailed below. For all subjects, surgeries were performed under aseptic conditions and body temperature was maintained with a heating pad. Rodents were anesthetized with isoflurane mixed with oxygen (5% for induction, 2.5-2% for maintenance, 1L/min oxygen flow rate) and placed in a digital small animal stereotax (David Kopf Instruments, Tujunga, CA, USA). Following initial induction, hair was removed from the dorsal surface of the head with hair clippers, ophthalmic ointment was applied to the eyes, the incision area was scrubbed with alcohol pads and betadine (x3 each), and 2% lidocaine was injected just under the skin surface above the skull for topical anesthesia. All measurements were made relative to bregma (unless noted otherwise) for virus/implant surgeries. Viral injections were performed using a beveled microinjection needle (26 gauge for rat; 33 gauge for mice) with a 10 µL microsyringe (Nanofil; WPI, Sarasota FL, USA) delivering virus at a rate of 0.05-0.01 µL/min using a microsyringe pump (UMP3; WPI, Sarasota, FL, USA) and controller (Micro4; WPI, Sarasota, FL, USA). For injections at multiple locations on the dorsal-ventral axis, the most ventral location was completed first and the injection needle was immediately relocated to the more dorsal location and initiated. After injection completion, 15 mins were allowed to pass before the needle was slowly withdrawn. After viral infusions were completed, craniotomies were filled with bone wax and the incision closed with nylon sutures. Subjects were maintained under a heat lamp and provided 0.05 mg/kg (rat) / 0.10 mg/kg (mouse) buprenophine (s.c., diluted in warm Ringers solution) until fully recovered from anesthesia.

All experiments involving the use of animals were in accordance with NIH guidelines and approved by the MIT Institutional Animal Care and Use Committee. For all experiments involving viral or tracer injections, animals containing mistargeted injection(s) were excluded after histological verification.

Viral constructs

Recombinant AAV_5 vectors carrying ChR2, NpHR, or fluorescent proteins (mCherry or eYFP) were packaged by the University of North Carolina Vector Core (Chapel Hill, NC, USA). We thank the UNC vector core for ChR2 and NpHR vectors.

Catecholamine terminal tracing

Male heterozygous tyrosine hydroxylase (TH)::Cre mice (8-9 weeks old) received unilateral injections of the anterogradely-traveling adeno-associated virus serotype 5 (AAV_5), encoding the fluorescent protein mCherry or eYFP under a double-floxed inverted open-reading frame (DIO) construct (AAV_5-DIO-EF1a- mCherry or AAV_5-DIO-EF1a-eYFP) in the ventral tegmental area (VTA; AP: -3.4, ML: +0.4, DV: -4.25 [1 µl]) and locus coeruleus (LC; AP: -5.45, ML: 1.25, DV: -4.0 & -7.8 [0.5 µl]), counter-balanced. Mice (n = 3) were given 10 weeks for viral expression and trafficking of the fluorescent protein to terminals in the medial prefrontal cortex (mPFC). After virus incubation, mice were transcardially perfused, tissue sectioned and immunohistochemically prepared to label TH+ neurons for histological analyses (described below). For quantification of fluorescently labeled TH+ neurons in the LC and VTA, single Z-stacks in the medial VTA and central LC were acquiring using a scanning confocal microscope (Olympus FV1000) with Fluoview software (Olympus, Center Valley, PA, USA) under a 60x/1.42 NA oil immersion objective. The number of co-labeled (TH+ and eYFP/mCherry+) neurons and eYFP/mCherry only labeled neurons were counted. Z-stack stitches encompassing both prelimbic (PL) and intralimbic (IL) regions of the mPFC were acquired under a 40x/1.30 NA oil immersion objective. Quantification of fluorescence intensity as a proxy for terminal density was accomplished by analyzing 100w x 200h µm sections across mPFC layers based on DAPI

density/morphology in FIJI ImageJ. Sections were normalized to the section with peak fluorescence within subjects. Sample size was based on reports in related literature and were not predetermined by calculation.

Fast-scan cyclic voltammetry (FSCV)

Subjects.

Male and female heterozygous BAC transgenic TH::Cre rats (~220 g) were dual housed with *ad libitum* access to water on a normal 12h:12h light/dark cycle (lights on at 09:00 AM).

Surgery.

TH::Cre rats which had received a unilateral injection of 2 µl adeno-associated virus serotype 5 (AAV_5), encoding channelrhodopsin-2 (ChR2)-mCherry or halorhodopsin 3.0 (NpHR)-eYFP, under a double-floxed inverted open-reading frame construct (DIO) (AAV_5-DIO-EF1a-ChR2-mCherry or AAV_5-DIO-EF1a-NpHR-eYFP) in the ventral tegmental area (VTA; AP: -5.3, ML: +0.7, DV: -8.2 & -7.8 [1 µl ea]) were given at least 8 weeks for viral expression before recording. Anesthetized *in vivo* FSCV experiments were conducted similar to those previously described (Matthews et al., 2016; Nieh et al., 2016). Rats were anesthetized with urethane (1.5 g/kg, i.p.) diluted in sterile saline and placed in a stereotaxic frame located in a faraday cage. For both experiments, a glass-encased carbon fiber electrode (~120 µm exposed carbon fiber, epoxied seal) was lowered into the mPFC (AP: +3.2, ML: +0.8 mm relative to bregma; DV: -2.0 mm from brain surface) through a small craniotomy performed above the deep layers of the mPFC for voltammetric recordings.

For ChR2 experiments (n = 5), additional craniotomies were performed above the VTA (AP: -5.5, ML: -0.6 mm), locus coeruleus (LC; AP: -9.6, ML: -1.2 mm), and contralateral cortex. A Ag/AgCl reference electrode, chlorinated just prior, was implanted in the contralateral cortex,

a manually-constructed optical fiber[11] (400 µm core, 0.48 NA; Thorlabs, Newton, NJ, USA) cut to 8 mm in length held in a 2.5 mm ferrule (Precision Fiber Products, Milpitas, CA, USA) was implanted above the VTA (DV: -7.0 mm), and a 26 gauge guide cannula (PlasticsOne, Roanoke, VA, USA) was positioned over the LC (DV: -6.6 mm). Implants were secured to the skull with adhesive cement (C&B Metabond; Parkell, Edgewood, NY, USA).

After cement dried, the optic fiber implant was connected to a patch cable (Doric, Quebec, CA) via a ceramic sleeve (PFP, Milpitas, CA, USA) and both reference and carbon-fiber recording electrode connected to the FSCV interface via custom-made headstage (Scott Ng-Evans, Paul E.M. Phillips Lab, University of Washington, USA). Dopamine (DA) release was evoked by optical activation of the VTA using 150 pulses of 473 nm light (25 mW, 5 ms pulse duration) at 50 or 30 Hz, delivered via a DPSS laser (OEM Laser Systems, Draper, UT) through the attached patch cable and controlled using a Master-8 pulse stimulator (A.M.P.I., Jerusalem, Israel). Electrodes were stereotaxically lowered in 0.2 mm increments until optimal DA release was detected by photoactivation of VTA DA neurons. Optically-evoked DA release was not detected from one subject for unknown reasons; however, tail-pinch evoked catecholamine release was observed with characteristic cyclic voltammograms (CVs) for catecholamines and was therefore included in analyses.

For NpHR experiments (n = 5), craniotomies (in addition to that above the mPFC) were performed above the VTA (AP: -5.5, ML: -0.6 mm), nucleus accumbens shell (NAc, AP: 1.5, ML: +0.9), and contralateral cortex. A Ag/AgCl reference electrode, chlorinated just prior, was implanted in the contralateral cortex and secured to the skull with adhesive cement (C&B Metabond; Parkell, Edgewood, NY). After cement dried, reference and carbon-fiber recording electrodes were connected to FSCV interface via headstage and the recording electrode was stereotaxically lowered into the NAc shell (DV: -6.6 mm relative to brain surface). Following equilibration (see below), a combination bipolar electrical stimulation electrode and 26 gauge

guide cannula (PlasticsOne, Roanoke, VA, USA) was stereotaxically lowered above the VTA (DV: -6.5 mm) and lowered in 0.2 mm increments until DA release was detected in the NAc by electrical activation of VTA DA neurons via 60 Hz, 60 pulses (biphasic, 200 uA), controlled by an ISO-Flex stimulus isolator (A.M.P.I., Jerusalem, Israel). Following DA detection, the combination electrical stimulation / guide cannula electrode was cemented in place (C&B Metabond; Parkell, Edgewood, NY, USA) slightly dorsal of the VTA and the carbon-fiber recording electrode transferred into the mPFC (DV: -2.0 mm) and allowed to equilibrate. Sample sizes were based on reports in related literature and were not predetermined by calculation.

Data acquisition.

For both experiments, electrodes were allowed to equilibrate for 20 min at 60 Hz and 10 min at 10 Hz. Voltammetric recordings were collected at 10 Hz by applying a triangular waveform (-0.4 V to +1.3 V to -0.4 V, 400 V/s) to the carbon-fiber electrode versus the Ag/AgCl reference implanted in the contralateral cortex. Data were collected in 60 s files with the tail pinch onset occurring 10 s into the file for a duration of 10 s (TarHeelCV, Chapel Hill, NC). Files were collected every 120 s and background subtracted at the lowest current value prior to pinch onset. Evoked signals maintained characteristic CVs for DA/NE (Heien et al., 2003), with oxidation and reduction peaks at ~+0.65 V and ~-0.2 V, respectively. For ChR2 experiments, 5 tail pinch recordings were obtained with a 120 s inter-recording interval, prior to LC inactivation. After recording were completed, 1 µl of tetrodotoxin (TTX, 10 ng/1.5 µl artificial cerebral spinal fluid) mixed with fast green (for spread visualization) was injected into the LC via a microinjection needle through the 26 gauge guide cannula controlled by a syringe pump. 10 min following infusion completion, 5 tail pinch recordings were obtained with a 120 s inter-recording interval, post-LC inactivation. For NpHR experiments, recordings were similarly obtained by 10 recordings at 120 s inter-recording interval were trials were interleaved with no optical manipulation trials ("OFF" trials) and trials where VTA DA neurons were inhibited with 20 s

constant 598 nm DPSS laser light (5 mW) delivered by a stripped 200 μm core patch cable (Doric, Quebec, CA) inserted into the combination electrical stimulation / guide cannula located dorsal of the NpHR-expressing VTA DA neurons ("ON" trials). Optical inhibition was initiated 5 s into each "ON" trial (i.e., 5 s prior to tail pinch onset) and remained for 20s (i.e., ending 5 s after tail pinch offset). Oscillatory signals were often observed in the mPFC (however, no such signals were detected in the NAc) and were attenuated by tail pinch and electrical stimulation. Trial averaging alleviated oscillatory interference. Following recording, rats were transcardially perfused and fixed (as described below) and processed using immunohistochemistry for TH immunolabeling to confirm viral expression and implant/recording electrode locations using confocal microscopy. Spread of TTX-fast green was recorded during tissue sectioning on a freezing, sliding microtome.

Data analysis.

Signals were converted to changes in catecholamine concentration using chemometric, principal component regression, and residual analyses using a custom LabView program (Umich CV, Courtesy of Richard Keithley), as previously described (Keithley and Wightman, 2011; Keithley et al., 2009; Vander Weele et al., 2014) using *in vivo* optically and electrically-evoked CVs and calibration data obtained from an average of 10 electrodes calibrated in known DA concentrations and pH units as previously described (Badrinarayan et al., 2012). For quantification of blue light evoked DA, area under the curve (AUC) was calculated during the 5 s pre-stimulation period, compared to the AUC 5 s following the initiation of 20 Hz, 60 pulses laser light. For quantification of tail pinch-evoked DA, AUC was calculated during the 10 s prior to pinch onset, compared to the AUC during the 10 s following pinch onset For comparison of pinch-evoked signals in "ON" and "OFF" trials in NpHR experiments, AUC was calculated during the 30 s period following pinch onset.

VTA^{DA}-mPFC behavioral optogenetic experiments

Subjects.

Male heterozygous BAC transgenic TH::Cre rats (Witten et al., 2011) (~220 g) were dual housed with *ad libitum* access to water on a normal 12h:12h light/dark cycle (lights on at 09:00 AM). ~1 weeks following viral injection surgeries, rats were individually housed with restricted food access (~16-20 g chow / day) for ~10 weeks, but retained *ad libitum* access to water. Sample size was based on reports in related literature and were not predetermined by calculation.

Surgery.

TH::Cre rats which had received a unilateral injection of 2 µl of AAV_5-DIO-EF1a-ChR2-eYFP [n = 6-8] or AAV_5-DIO-EF1a-eYFP [n = 5-7]) in the ventral tegmental area (VTA; AP: -5.3, ML: +0.7, DV: -8.2 & -7.8 [1 µl ea]) were given at least 12 weeks incubation period to ensure Cre-specific viral transduction of ChR2 in VTA^{DA} neurons and protein transport to distal terminals in the mPFC. Following incubation, 20G stainless steel cannulae (PlasticsOne, Roanoke, VA) were bilaterally implanted above the mPFC (AP: +3.2-3.6; ML: ±2.0, DV: -2.8; mm relative to bregma at a 15° angle, bilateral). Guide cannulae were secured to the skull with 2-4 skull screws, a layer of adhesive cement (C&B Metabond; Parkell, Edgewood, NY, USA), followed by black cranioplastic cement (Ortho-Jet; Lang, Wheeling, IL, USA) containing gentamicin antibiotic. The implant was allowed to completely dry before closure of the incision with nylon sutures. 24G dummies were inserted into toe cannulae to present clogging.

General testing procedures.

On each test day, a 400 µm core optical fiber was inserted and attached to the cannulae. Optical fibers extended ~250-500 um beyond the cannulae tips. Rats were then transferred to their behavioral apparatus and connected to patch cords connected to dual-rotating

commutators for testing. Real-time place preference / aversion and conditioned place preference / aversion assays were identical to those described above. 473 nm laser light was delivered through the patch cords at 20 Hz, 60 p (5 ms pulses) every 30 s at 20 mW from optic fiber tip. If an optic fiber broke into a guide cannula or if a guide cannula became clogged, the contralateral guide cannula was used for remaining experiments. Manipulated hemispheres were counterbalanced.

Real-time place preference / aversion.

Individual food-restricted rats were placed in a Plexiglas arena (24l x 24w in x 20h in) and were allowed to freely move between two compartments for 1 hr in a dimly lit room containing constant white noise (Marpac Dohm-DS dual speed sound conditioner, Wilmington, NC, USA). Entry into one half of the chamber resulted in photostimulation (VTA^{DA}-mPFC::ChR2/eYFP = unilateral 20 Hz, 60 p, 5 ms pulses every 30 s, 20 mW; mPFC-dPAG/NAc::ChR2/eYFP = bilateral 20 Hz 5 ms pulses, 12-15 mW, *see below*). Stimulation and no stimulation sides were counterbalanced between animals. Rats were tested on 2 consecutive days and on the second day; the stimulation side and no stimulation side were reversed. A video camera positioned directly above the arena tracked and recorded movement using EthoVision XT (Noldus, Wageningen, Netherlands). All data presented are tracked from the "center" of the subject and time spent in each zone was averaged across the 2 testing sessions. In between subjects, the behavioral chamber was thoroughly cleaned with 10% glass cleanser diluted in ddH20.

Conditioned place preference / aversion.

Individual food-restricted rats were placed in a Plexiglas arena (30l x 15w in x 25h in) divided into two compartments: one with vertical stripes and the other with horizontal stripes. On day 1 (habituation), rats were allowed to freely move between two compartments for 15 min in a brightly lit room containing constant white noise (Marpac Dohm-DS dual speed sound

conditioner, Wilmington, NC, USA). Movement was tracked by an overhead video camera positioned above the arena and time spent in each compartment was calculated using EthoVision XT (Noldus, Wageningen, Netherlands). On day 2 and 3, rats were exposed to conditioning sessions (20 min ea, 1 per day) during which they were confined to one side of the chamber and received optical stimulation (VTA^{DA}-mPFC::ChR2/eYFP = unilateral 20 Hz, 60 p, 5 ms pulses every 30 s, 20 mW; mPFC-dPAG/NAc::ChR2/eYFP = bilateral 20 Hz 5 ms pulses, 12-15 mW, *see below*) or no stimulation (counterbalanced for order and side across animals). On day 4 (test), rats were placed in the chamber and allowed to freely explore both compartments in the absence of optical stimulation. Again, movement was tracked by an overhead video camera positioned above the arena using EthoVision XT (Noldus, Wageningen, Netherlands) and a time difference score was calculated by subtracting the time spent in the stimulation-paired compartment on the habituation day from the time spent in the stimulation-pared compartment on the test day (test[time spent in paired side] – habituation[time spent in paired side]).

Stimulus competition task.

Training and testing procedures were similar to those previously described (Burgos-Robles et al., 2017). Training was performed in standard rat operant chambers (23 x 30 x 40 cm; Med Associates) located within sound-attenuating cubicles. Each chamber was equipped with a red house light, speakers for the delivery of tone cues, a sucrose port that was equipped with an infrared beam for the detection of port entries and exits, a syringe pump to deliver sucrose (30% in cage water), 2 light cues on either side of the sucrose port, and a grid floor for the delivery of electrical shocks. Chambers were wiped down with 70% isopropyl alcohol after each session. Prior to training, rats were pre-exposed to sucrose in their homecage and were magazine trained in the operant boxes (60 min, 20 sucrose deliveries). The first phase of training consisted of Pavlovian reward conditioning where rats learned to associate a 20 s

conditioned stimulus (CS^{suc}, either a light cue or tone cue [5 kHz, 80 dB], counter-balanced between subjects) with sucrose delivery into the reward port (30% sucrose, 120 uL/ trial). Sucrose was delivered over 10 s during the cue presentation (5-15 s, relative to CS^{suc} onset). Inter-trial intervals were set to an average of 60 s. If sucrose was not consumed (as detected by the lack of a port entry during the 20 s CS^{suc} presentation), sucrose was immediately removed after cue offset via activation of a vacuum tube located in the sucrose port. Rats were trained on sucrose conditioning for 3 days with each session comprised of 25 trials delivered over ~35 min. The second phase of training consisted of four Pavlovian discrimination sessions where conditioned stimuli predicted sucrose (CS^{suc}) or footshock (CS^{shk}) delivery. During these sessions, the opposite conditioned stimulus (either a light cue or tone cue [5 kHz, 80 dB]) co-terminated with 0.5 s footshock (0.60 mA, 19.5 – 20 s relative to CS^{shk} onset). CS^{suc} and CS^{shk} cues were counterbalanced and presented in a pseudorandom manner. Each sessions consisted of 40 total trials (20 of each trial type) with a variable ~60 s ITI. During sucrose conditioning and discrimination sessions, animals were unilaterally connected to a rotating commutator via a dummy patch cord, but no laser light was delivered.

The third phase was the stimulus competition test sessions. Prior to these sessions, an optical fiber was loaded into a guide cannula, connected to a patch cord, and attached to a rotating commutator, identical to the prior phases. During competition sessions, in addition to CS^{suc} and CS^{shk} trials, competition trials were introduced – in which CS^{suc} and CS^{shk} cues and their respective outcomes were co-presented to evoke conflicting motivation between reward- and fear-associated behaviors. 1 s prior to competition trials (CS^{comp}), 473 nm laser was triggered (20 Hz, 60 p, 5 ms pulses every 5 s) for the duration of the 20 s compound cue (4 stimulation trains per CS). Each competition session consisted of 60 total trials (20 of each trial type) with a variable ~60 s ITI.

Data analysis.

Sucrose port entries and exits provided a read-out for reward-related behavior (based on % of time in the port during each trial type) and were sampled from infrared beam breaks (Med-PC IV, Med Associates. Freezing, defined as the lack of all movement other than respiration, provided a read-out for aversively-motivated behavior. Videos were sampled using side-profiled infrared cameras at 30 fps and freezing was quantified using an automated custom MATLAB script that calculated frame-by-frame changes in total pixel intensity as an approximation for animal movement. Frame-by-frame motion values were converted into freezing scores using a binary method relative to a motion threshold. This method produced values which are highly correlated with hand-scored measured of freezing (Burgos-Robles et al., 2017)The time spent in the port was subtracted from the freezing quantification, as animals showed little movement while collecting sucrose.

Histology

Perfusion and storage.

Subjects were deeply anesthetized with sodium pentobarbital (200 mg/kg; i.p.) and transcardially perfused with 15 mL (mouse) / 60 mL (rat) of Ringers solution followed by 15 mL (mouse) / 60 mL (rat) of cold 4% paraformaldehyde (PFA) dissolved in 1x PBS. Animals were decapitated and the brain was extracted from the cranial cavity and placed in 4% PFA solution and stored at 4 °C for at least 48 hrs. 36 hrs before tissue sectioning, brains were transferred to 30% sucrose solution dissolved in 1x PBS at room temperature. Upon sinking, brains were sectioned at 60 um on a freezing sliding microtome (HM420; ThermoFischer Scientific). Sections were stored in 1x PBS at 4 °C until immunohistochemical processing.

Immunohistochemistry.

Sections were blocked in 1x PBS - 0.3% Triton containing 3% donkey serum (Jackson ImmunoResearch, West Grove, USA), for 1 h at room temperature followed by incubation in primary antibody solution: chicken anti-TH (1:1000; Millipore, USA) or rabbit anti c-Fos (1:500; Santa Cruz Biotechnology, Dallas, TX, USA) in 1x PBS - 0.1% Triton containing 3% donkey serum for 48 h at 4 °C. Sections were then washed 4 times (10 min each) with 1x PBS and immediately transferred to secondary antibody solution: AlexaFluor 647-conjugated donkey anti-chicken (1:1000; Jackson ImmunoResearch, West Grove PA, USA) or Cy3 donkey anti-rabbit (1:500, Jackson ImmunoResearch, West Grove, PA, USA) and containing a DNA-specific fluorescent probe (DAPI; 1:50,000) in 1x PBS containing 3% donkey serum for 2 h at room temperature. Sections not processed for immunohistochemistry were incubated in 1x PBS - 0.3% Triton containing 3% normal donkey serum (Jackson ImmunoResearch, West Grove, USA) and DAPI (1:50,000) for 1 hr. Sections were washed 4 times (10 min each) in 1x PBS and mounted onto glass slides. Slices were allowed to dry and were coverslipped using polyvinyl alcohol (PVA) mounting medium with DABCO (Sigma, MO, USA).

Confocal microscopy.

Fluorescent images were captured using a confocal laser scanning microscope (Olympus FV1000), with FluoView software (Olympus, Center Valley, PA), under a dry 10x / 0.40 NA objective, a 60x/1.42 NA oil immersion objective, or a 40x /1.30 NA oil immersion objective. The locations of opsin expression, injection site, lesion from the optic fiber placement, and the position of carbon-fiber recording electrodes were determined by taking serial z-stack images through the 10x objective across a depth of 20-40 µm, with an optical slice thickness of 5-8 µm. High magnification images fluorescence quantifications were obtained through the 40x or 60x objective using serial z-stack images with an optical slice thickness of 3-4 µm (5 slices) using matched parameters and imaging locations. Fluorescence (in arbitrary units) was

obtained from analysis in FIJI ImageJ. For quantitation of fluorescence across layers in the mPFC, measurements were normalized to the Z-stack containing the maximum value.

Statistics

Statistical analyses were performed using GraphPad Prism (GraphPad Software, Inc, La Jolla, CA). Paired and unpaired two-way Student's t-tests were used to make single-variable comparisons. Thresholds for significance were placed at $*p < 0.05$, $**p < 0.01$, $***p < 0.001$. All data are shown as mean ± standard error of the mean (SEM).

Summary

Taken together, these data suggest that dopamine is released in a time-locked manner upon an aversive stimulus and that VTA^{DA} in the mPFC plays an instructive role in biasing behavioral responses towards aversion in the face of conflicting cues.

Author Contributions

Conception. Caitlin M. Vander and Kay M. Tye

Surgical injections and implantations. Caitlin M. Vander Weele, Cody A. Siciliano. Ehsan M. Izadmehr, Isabella C. Espinel

Fast-scan cyclic voltammetry. Caitlin M. Vander Weele

Behavioral Experiments – Stimulus Competition. Caitlin M. Vander Weele and Tony Burgos-Robles

Histology. Caitlin M. Vander Weele, Ehsan M. Izadmehr, Isabella C. Espinel

Confocal Microscopy. Caitlin M. Vander Weele

Chapter 3

Prefrontal projections to the striatum and periaqueductal gray are distinct and differentially encode and promote reward and aversion

Introduction

The mPFC has copious projections throughout the brain (Sesack 1989; Vertes, 2004) and we next sought to identify a projection that might serve to translate aversive signals into action. As previously mentioned, subcortical projection predominately reside in output Layers 5 and 6 (Gabbott et al., 2005), which also express dopamine receptors (Gaspar et al., 1995). Prominent projections from the mPFC include the: basolateral amygdala (BLA), NAc / ventral striatum, lateral hypothalamus, periaqueductal gray (PAG), medial dorsal thalamic structures, and the dorsal raphe (Gabbott et al., 2005). mPFC projections to the NAc (mPFC-NAc; ~27% of Layer 5 neurons) and mPFC projections to the PAG (mPFC-PAG; ~3% of Layer 5 neurons) stood out as promising candidate regions which likely convey motivationally-relevant stimuli from the mPFC (Estimated proportion of projection neurons from retrograde labeling - Gabbott et al., 2005).

The PAG is a heterogenous midbrain structure considered an important relay center for defensive and threat responses (Bandler and Carrive, 1988; Bandler et al., 1985a, 1985b; Carrive et al., 1987; Fanselow, 1991; Tovote et al., 2016). In humans, the PAG is implicated in the general processing of aversive emotions (Buhle et al., 2013; Lindquist et al., 2012; Satpute et al., 2013), threat proximity (Mobbs et al., 2007, 2010), and threat anticipation (Meyer et al., BioRxiv, 2017). In non-primate models, local electric and glutamate stimulation of the PAG elicits a diverse range of aversive and defensive behavioral reactions, which vary within subcolumns along both medial-lateral and dorsal-ventral axes (Bandler & Carrive, 1988). Recently, optogenetic stimulation of neurons in the dorsal PAG (dPAG) has been shown to

evoke flight behaviors (Deng et al., 2016; Tovote et al., 2016). Further, dPAG neurons are activated at the initiation of escape responses measured by *in vivo* single cell calcium imaging in freely moving subjects (Evans et al., BioRxiv, 2018) and *in vivo* electrophysiology (Halladay and Blair, 2015). Together these data along with many others, strongly suggest that the dPAG is a crucial node mediating active avoidance strategies, rather than passive strategies (i.e., freezing), which have been attributed to the ventral portions of the PAG (Assareh et al., 2016; Bandler and Depaulis, 1988; Tovote et al., 2016). Considering several lines of evidence suggest that connections between the mPFC and dPAG (mPFC-dPAG) specifically are involved in coordinating behavioral strategies in response the threating stimuli (Mobbs et al., 2007; Halladay et al., 2015), we decided to investigate this pathway's involvement in aversive motivation and its responsivity to dopamine.

In contrast, the NAc is historically viewed as a reward center because of its involvement in reward-learning (Schultz et al., 1997), reward-seeking (Phillips et al., 2003; Roitman et al., 2004) and hedonic pleasure (Castro and Berridge, 2014). Optogenetic stimulation of mPFC terminals in the NAc has been shown to support place preference and operant reinforcement (Britt et al., 2012). However attempts to replicate this effect have been unsuccessful (Otis et al., 2017; Stuber et al., 2011), which may be attributed to the location (i.e., soma versus terminal) or stimulation parameters (i.e., frequency, light power). Recently, *in vivo* single-cell calcium imaging during reward-learning has revealed that mPFC-NAc neurons show enhanced responses to reward-predictive cues during conditioning and that optogenetic stimulation promotes the expression of conditioned-reward seeking (Otis et al., 2017). Considering VTA dopamine axon terminals synapse onto mPFC neurons projecting to the NAc (Carr et al., 1999) and that a subset of mPFC-NAc neurons express dopamine receptors (Gaspar et al., 1995), we decided to investigate this pathway as a point of contrast. Here we explore the anatomy, activity, and behavioral functions of mPFC-dPAG and mPFC-NAc subpopulations.

Results

To explore the putative density between the mPFC and downstream brain regions, we transduced mPFC neurons with AAV-CaMKIIα-eYFP in the rat and explored downstream fluorescence in a subset of candidate regions (**Figure 7a-c**). Fluorescence intensity, measured in arbitrary units (A.U.), revealed putative connections with several brain regions— including the nucleus accumbens (NAc) and dorsal periqueductal gray (dPAG) (**Figure 7d**).

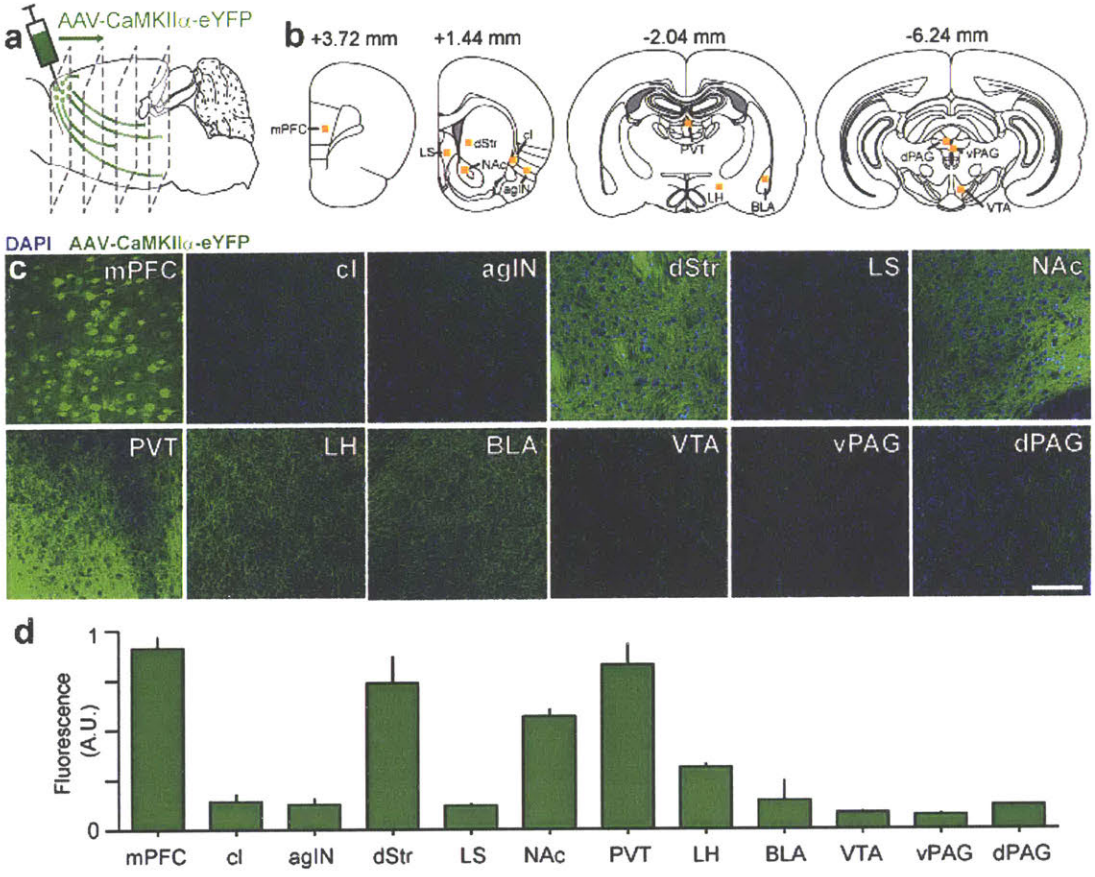

Figure 7. Putative connection strength of mPFC projections to downstream targets.

(a) Schematic of strategy where anterogradely traveling virus was injected into the prelimbic and infralimbic subregions of the mPFC and fluorescence was quantified in several downstream brain regions.

(b) Orange boxes represent approximate locations of fluorescence quantification, as a proxy for connection strength (n = 3).

(c) Representative images of fluorescence in the mPFC and downstream targets in the rat.

(d) Quantification of fluorescence in the mPFC and downstream targets in the rat.

Abbreviations: agIN = agranular insula; BLA = basolateral amygdala; cl = claustrum; dPAG = dorsal periaqueductal gray; dStr = dorsal striatum (medial); LH = lateral hypothalamus; LS = lateral septum; mPFC = medial prefrontal cortex; NAc = nucleus accumbens; PVT = paraventricular nucleus of the thalamus; vPAG = ventral periaqueductal gray; VTA = ventral tegmental area.

Error bars indicate ±SEM.

In animal studies, stimulation of the PAG evokes aversive responses, including defensive and attack behaviors (Bandler and Carrive, 1988; Deng et al., 2016; Silva et al., 2016; Tovote et al., 2016) and in humans, impending threat is associated with shifts in activity from the mPFC to the PAG (Mobbs et al., 2007). While projections to the dorsal periaqueductal gray (dPAG) have been explored in the context of social behavior (Franklin et al., 2016), contributions of the mPFC-dPAG circuit to aversive stimulus processing have not yet been evaluated. Due to its reported role in reward-related processes, we also investigated the mPFC-NAc projection for comparison (Britt et al., 2012; Murugan et al., 2017; Otis et al., 2017; Ye et al., 2016). To determine whether mPFC-dPAG and mPFC-NAc neurons form dissociable subpopulations, retrograde tracers were injected into the dPAG and NAc in both the rat (**Figure 8a-b**) and mouse (**Figure 8g-h**). Consistent with previous results (Franklin et al., 2017), mPFC-NAc and mPFC-dPAG neurons were localized to specific cortical layers and few neurons were dual-labeled in both the rat (11 of 1679) and mouse (17 of 458) (**Figure 8**). Interestingly, mPFC-NAc layer localization was slightly different between rodent species, with the highest density in Layer 5 in the rat (**Figure 8e**) and Layer 2/3 in mouse (**Figure 8k**). Additionally, anatomical investigations into collateralization of mPFC-NAc and mPFC-dPAG neurons using virally-expressed, projection-specific fluorescent synaptophysin did not provide detectable evidence for collateralization between the two subpopulations (**Figure 9a-d**), further suggesting that they are dissociable populations.

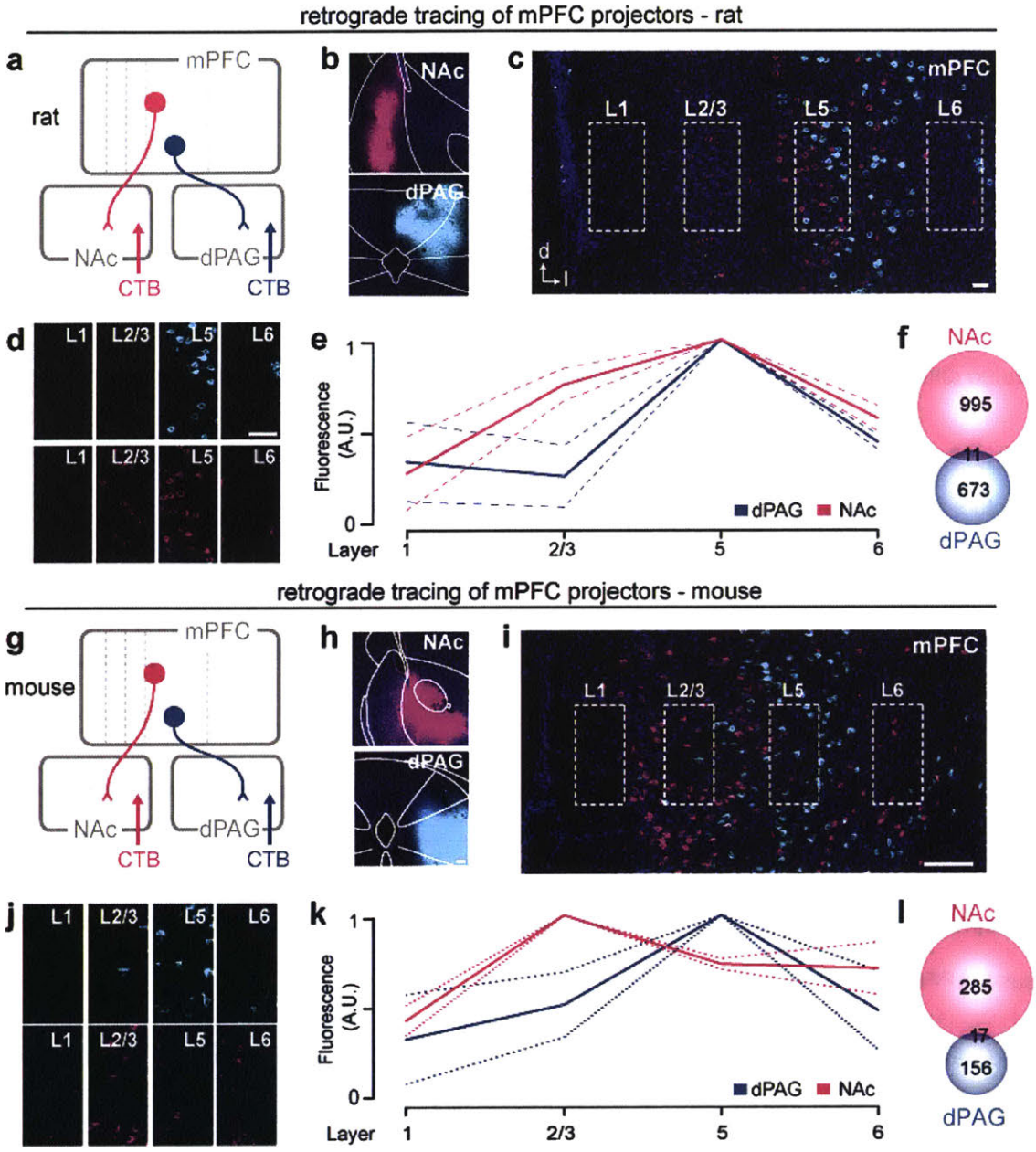

Figure 8. mPFC-dPAG and mPFC-NAc projector populations are distinct.

(a) Schematic of strategy for retrogradely labeling mPFC-NAc and mPFC-dPAG subpopulations in the rat.

(b) Representative images of microinjections of cholera toxin subunit B (CTB) conjugated to fluorescent proteins (AlexaFluor-488, -555, or -647, counter-balanced) placed in the rat dPAG and NAc.

(c) Representative images of retrogradely labeled cell bodies of dPAG- and NAc-projection neurons in the rat mPFC.

(d) Fluorescence quantification of retrogradely labeled mPFC-dPAG and mPFC-NAc neurons revealed differences in cell body location across cortical layers in the rat mPFC.

(e) In the rat, dPAG-projectors predominately originate from deep layer 5, whereas NAc-projectors are located in both superficial layers 2/3 and deep layer 5.

(f) As a population, only 11 out of 1,679 CTB+ neurons in the mPFC were dual-labeled.

(g) Schematic of strategy for retrogradely labeling mPFC-NAc and mPFC-dPAG subpopulations in the mouse.

(h) Representative images of microinjections of CTB conjugated to fluorescent proteins were placed in the mouse dPAG and NAc.

(i) Representative images of retrogradely labeled cell bodies of projection neurons in the mouse mPFC.

(j) Fluorescence quantification of retrogradely labeled mPFC-dPAG and mPFC-NAc neurons revealed differences in cell body location across cortical layers in the mouse mPFC.

(k) In the mouse, dPAG-projectors predominately originate from deep layer 5, whereas NAc-projectors are located in both superficial layers 2/3 and deep layer 5.

(l) As a population, only 17 out of 458 CTB+ neurons in the mPFC were dual-labeled.

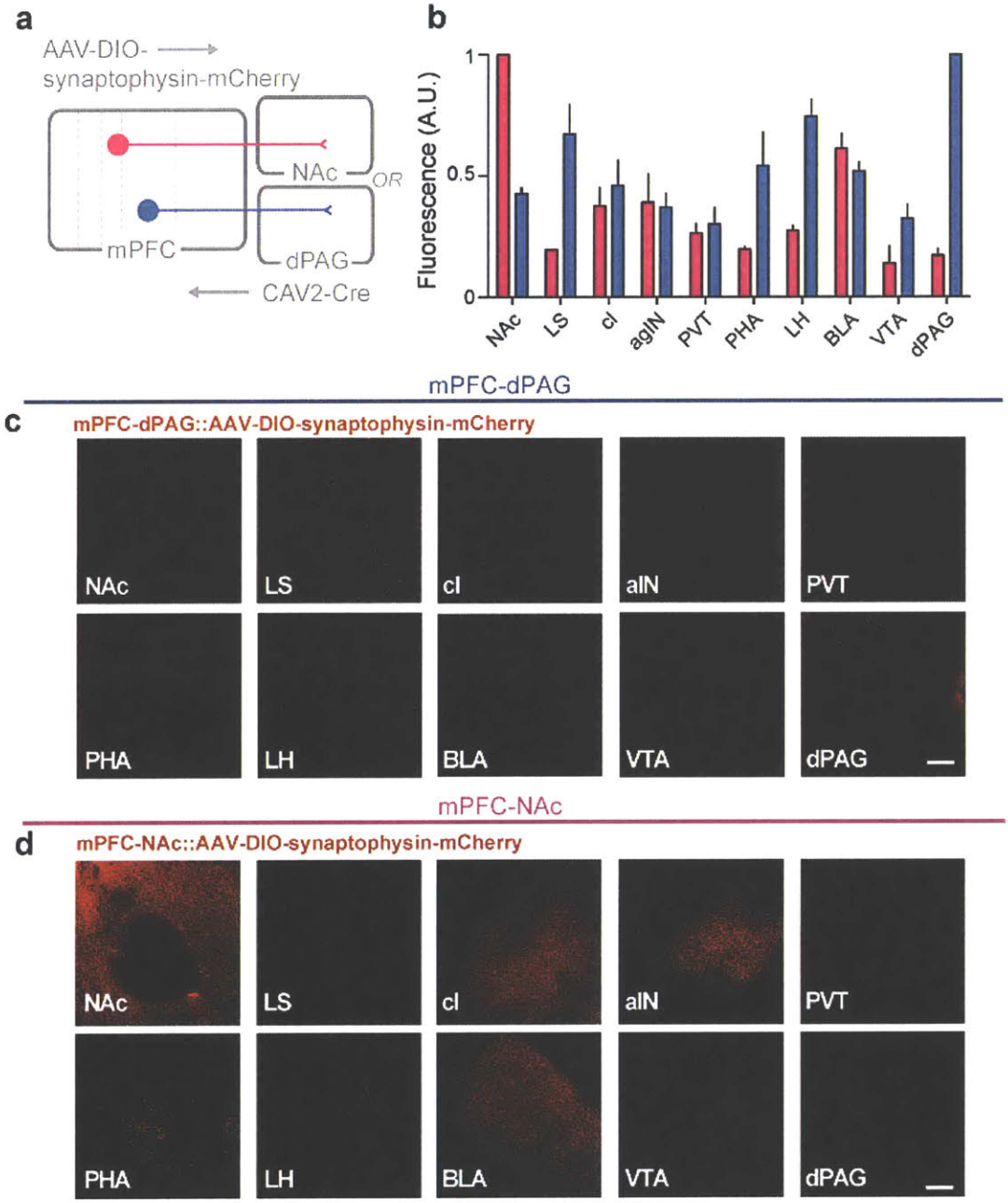

Figure 9. Collateralization of mPFC-NAc and mPFC-dPAG projector subpopulations.

(a) Schematic of viral strategy to explore downstream terminals from mPFC-NAc::synaptophysin and mPFC-dPAG::synaptophysin projectors (n = 3 per group).

(b) Quantification of fluorescence in the mPFC and downstream brain regions originating from mPFC-dPAG::synaptophysin and mPFC-NAc::synaptophysin neurons.

(c) Representative confocal images from a mPFC-dPAG::synaptophysin subject.

(d) Representative confocal images from a mPFC-NAc::synaptophysin subject.

Abbreviations: agIN = agranular insula; BLA = basolateral amygdala; cl = claustrum dPAG = dorsal periaqueductal gray; dStr = dorsal striatum (medial); LH = lateral hypothalamus; LS = lateral septum; mPFC = medial prefrontal cortex; NAc = nucleus accumbens; PHA = posterior hypothalamic area; PVT = paraventricular nucleus of the thalamus; VTA = ventral tegmental area.

Error bars indicate ±SEM. Scale bar = 100 um.

To target mPFC-NAc neurons, we used a dual virus approach (Senn et al., 2014). In rats, an anterogradely-traveling adeno-associated viral vector carrying ChR2- eYFP or eYFP alone (AAV-DIO-ChR2-eYFP or AAV-DIO-eYFP), expressed in a Cre-dependent manner, was injected into the mPFC and a retrogradely-traveling canine adenovirus vector carrying Cre-recombinase (CAV2-Cre) was injected into the NAc (**Figure 10a-b**). We found that photostimulation of mPFC-NAc neurons did not produce detectable differences between ChR2- and eYFP-expressing groups during RTPP/A (**Figure 10c-d**) or CPP/A (**Figure 10e-f**). These findings are consistent with some reports (Kim et al., 2016; Otis et al., 2017; Stuber et al., 2011), but not others (Britt et al., 2012). We speculate these discrepancies are related to the heterogeneity of the nucleus accumbens and differential targeting of core and/or shell subregions (Badrinarayan et al., 2012; Kim et al., 2017; Lammel et al., 2011) or the strength of activation due to illumination or opsin expression levels. Further, no effect was observed on anxiety-related behavior, as measured by time spent in the center in the open-field test (OFT) (**Figure 10g-h**) or on gross locomotion (**Figure 10i**).

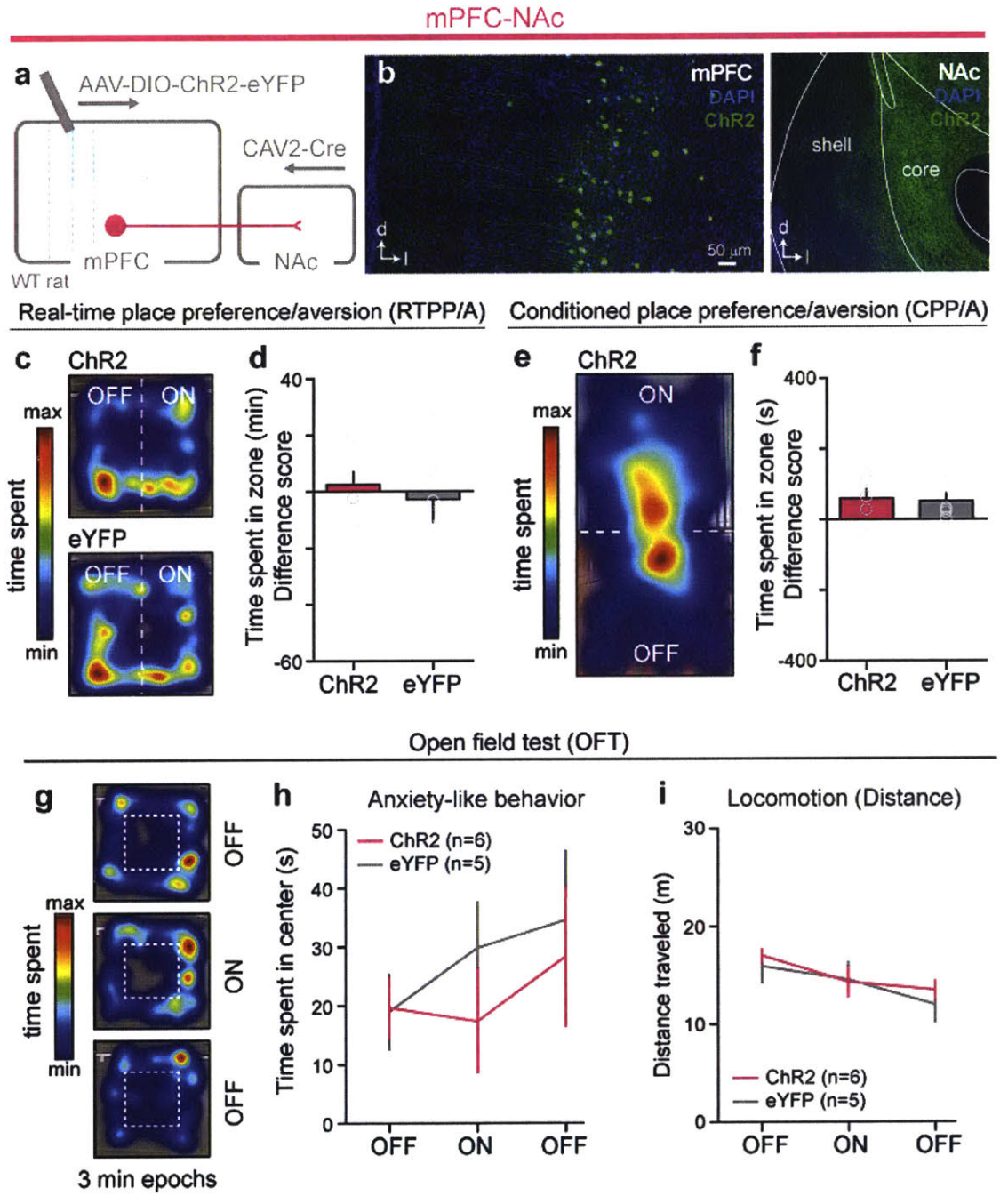

Figure 10. Activation of mPFC-NAc neurons does not support real-time or conditioned placed preference / aversion.

(a) Schematic of viral transduction strategy to achieve optogenetic control of rat mPFC neurons projecting to the NAc.

(b) Representative image of NAc-projecting mPFC neurons expressing ChR2 (left) and ChR2+ terminals in the NAc.

(c) Representative locomotor heatmaps of mPFC-NAc::ChR2 (top) and mPFC-NAc::eYFP (bottom) subjects during real-time place preference / aversion assay.

(d) Optogenetic stimulation of mPFC-NAc neurons did not evoke real-time place avoidance or preference in mPFC-NAc::ChR2 animals, compared to mPFC-NAc::eYFP controls, measured by difference score [minutes spent in the ON zone – OFF zone] (unpaired t-test, $t(11) = 0.555$, $p = 0.5901$).

(e) Representative locomotor heatmap of mPFC-NAc::ChR2 subject during condition place preference / aversion assay.

(f) Optogenetic stimulation of mPFC-NAc neurons did not evoke real-time place avoidance or preference in mPFC-NAc::ChR2 animals, compared to mPFC-NAc::eYFP controls, measured by difference score [minutes spent in the ON zone – OFF zone] (unpaired t-test, $t(10) = 0.2143$, $p = 0.8346$).

(g) Representative locomotor heatmaps of a mPFC-NAc::ChR2 subject during 3 min OFF-ON-OFF epochs during the open-field test (OFT).

(h) Optical activation of mPFC-NAc::ChR2 did not change time spent in the center region compared to eYFP controls, as measured by time spent in the center of the arena (two-way repeated measures ANOVA, $F_{2,18} = 0.4913$, $p > 0.05$).

(i) Optical activation of mPFC-NAc::ChR2 did not change general locomotor activity (two-way repeated measures ANOVA, $F_{2,18} = 0.5532$, $p > 0.05$).

To target mPFC-dPAG neurons, we again used a dual virus approach (Senn et al., 2014), where an anterogradely-traveling adeno-associated viral vector carrying ChR2- eYFP or eYFP alone (AAV-DIO-ChR2-eYFP or AAV-DIO-eYFP), expressed in a Cre-dependent manner, was injected into the mPFC and a retrogradely-traveling canine adenovirus vector carrying Cre-recombinase (CAV2-Cre) was injected into the dPAG (**Figure 11a-b**). Using *ex vivo* electrophysiology, we verified the functionality of ChR2 within this pathway and the 20 Hz stimulation parameters using 473 nm light (**Figure 11c-e**). Further, we validated ChR2 functionality *in vivo* by examining the immediate early gene, c-Fos in mPFC-dPAG::ChR2+ neurons (**Figure 11f-g**). In contrast to the lack of effect observed in mPFC-NAc subjects, activation of mPFC-dPAG neurons in ChR2-expressing rats reduced the time spent in the light-paired chamber in both RTPA (**Figure 11h-i**) and CPA (**Figure 11j-k**), relative to eYFP controls – thus demonstrating that these neighboring, projection-defined populations are functionally distinct.

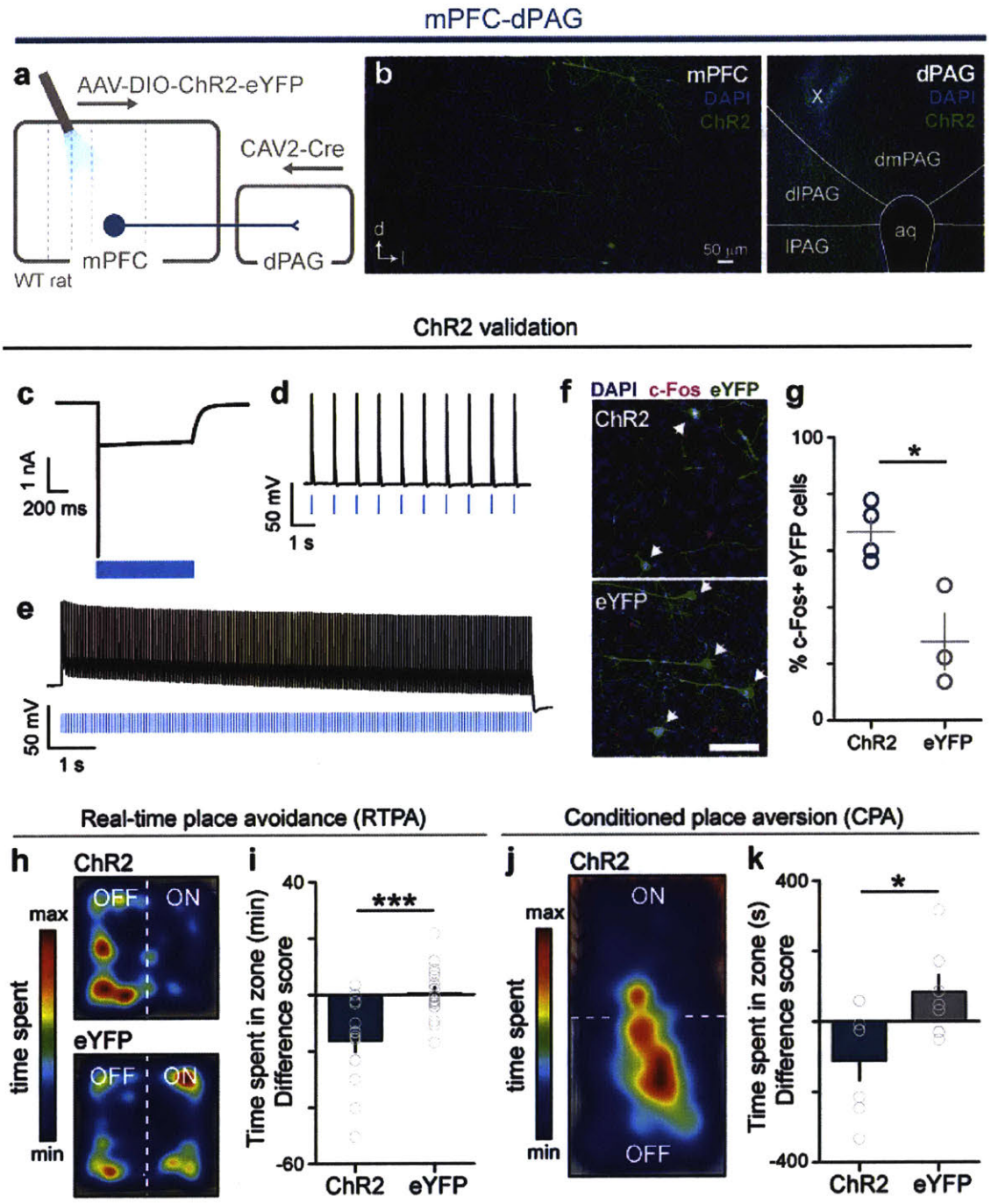
mPFC-dPAG
a
AAV-DIO-ChR2-eYFP
CAV2-Cre
mPFC
dPAG
WT rat
b
mPFC
DAPI
ChR2
50 µm
dPAG
DAPI
ChR2
dmPAG
dlPAG
lPAG
aq
ChR2 validation
c
1 nA
200 ms
d
50 mV
1 s
e
50 mV
1 s
f
DAPI c-Fos eYFP
ChR2
eYFP
g
% c-Fos+ eYFP cells
100
0
*
ChR2
eYFP
Real-time place avoidance (RTPA)
Conditioned place aversion (CPA)
h
ChR2
max
time spent
min
OFF
ON
eYFP
OFF
ON
i
Time spent in zone (min)
Difference score
40
-60
***
ChR2
eYFP
j
ChR2
max
time spent
min
ON
OFF
k
Time spent in zone (s)
Difference score
400
-400
*
ChR2
eYFP

Figure 11. Activation of mPFC-dPAG neurons supports real-time or conditioned placed aversion.

(a) Schematic of viral transduction strategy to achieve optogenetic control of rat mPFC neurons projecting to the dPAG.

(b) Representative image of dPAG-projecting mPFC neurons expressing ChR2 (left) and ChR2+ terminals in the dPAG surrounding the injection site (marked by an X).

(c) *Ex vivo* recording from a ChR2-expressing mPFC-dPAG neuron in voltage-clamp mode showing sustained inward current elicited by a 1 s pulse of 470 nm) light.

(d) In current-clamp mode, action potentials were elicited by 1 Hz laser pulses (470 nm, 5 ms pulse-duration).

(e) In current-clamp mode, action potentials were elicited by 20 Hz light trains (470 nm, 5 ms pulse-duration).

(f) Representative confocal images of mPFC-dPAG::ChR2 (top) and mPFC-dPAG::eYFP expressing neurons showing c-Fos expression following 5 min of blue (473 nm) light exposure (20 Hz, 5 ms pulse-duration, 15 mW).

(g) 473 nm laser light stimulation enhanced the number of immediate early gene (c-Fos) positive ChR2-expressing mPFC-dPAG neurons compared to control mPFC-dPAG::eYFP neurons (mPFC-dPAG::ChR2 n = 4; mPFC-dPAG::eYFP n = 3; unpaired t-test, $t(5) = 3.707$, $p = 0.014$).

(h) Representative locomotor heatmaps of mPFC-dPAG::ChR2 (top) and mPFC-dPAG::eYFP (bottom) subjects during real-time place avoidance assay.

(i) Optogenetic stimulation of mPFC-dPAG neurons evoked real-time place avoidance in mPFC-dPAG::ChR2 animals, compared to mPFC-dPAG::eYFP controls, measured by difference score [minutes spent in the ON zone – OFF zone] (unpaired t-test, $t(30) = 3.902$, $p = 0.005$).

(j) Representative locomotor heatmap of mPFC-dPAG::ChR2 subject on test day during conditioned-place avoidance assay.

(k) Optogenetic stimulation of mPFC-dPAG neurons produced real-time place avoidance in mPFC-dPAG::ChR2 animals, compared to mPFC-dPAG::eYFP controls, measured by difference score [minutes spent in the ON zone – OFF zone] (unpaired t-test, $t(12) = 2.638$, $p = 0.022$).

We further investigated the effects of activating mPFC-dPAG neurons on assays for locomotor activity, general anxiety, and defensive behavior. In the OFT, which assays locomotor activity and anxiety-related behavior, we did not observe any differences for distance traveled nor time spent in the center of the chamber between ChR2- and eYFP-expressing rats during the illumination epoch (**Figure 12a-c**). Strikingly, mPFC-dPAG photostimulation during a marble burying assay produced a robust increase in the number of marbles buried (**Figure 12-d-f**) and time spent digging (**Figure 12g**). Importantly, expression was restricted to the dorsal / lateral portions of the PAG, verified in a subset of animals where CAV2-Cre (no fluorophore tag) was co-injected with AAV-synapsin-mCherry (**Figure 12h-i**). The effects in the RTPA and marble burying assays observed upon mPFC-dPAG activation were reproduced by activation of mPFC terminals directly in the dPAG (**Figure 13**).

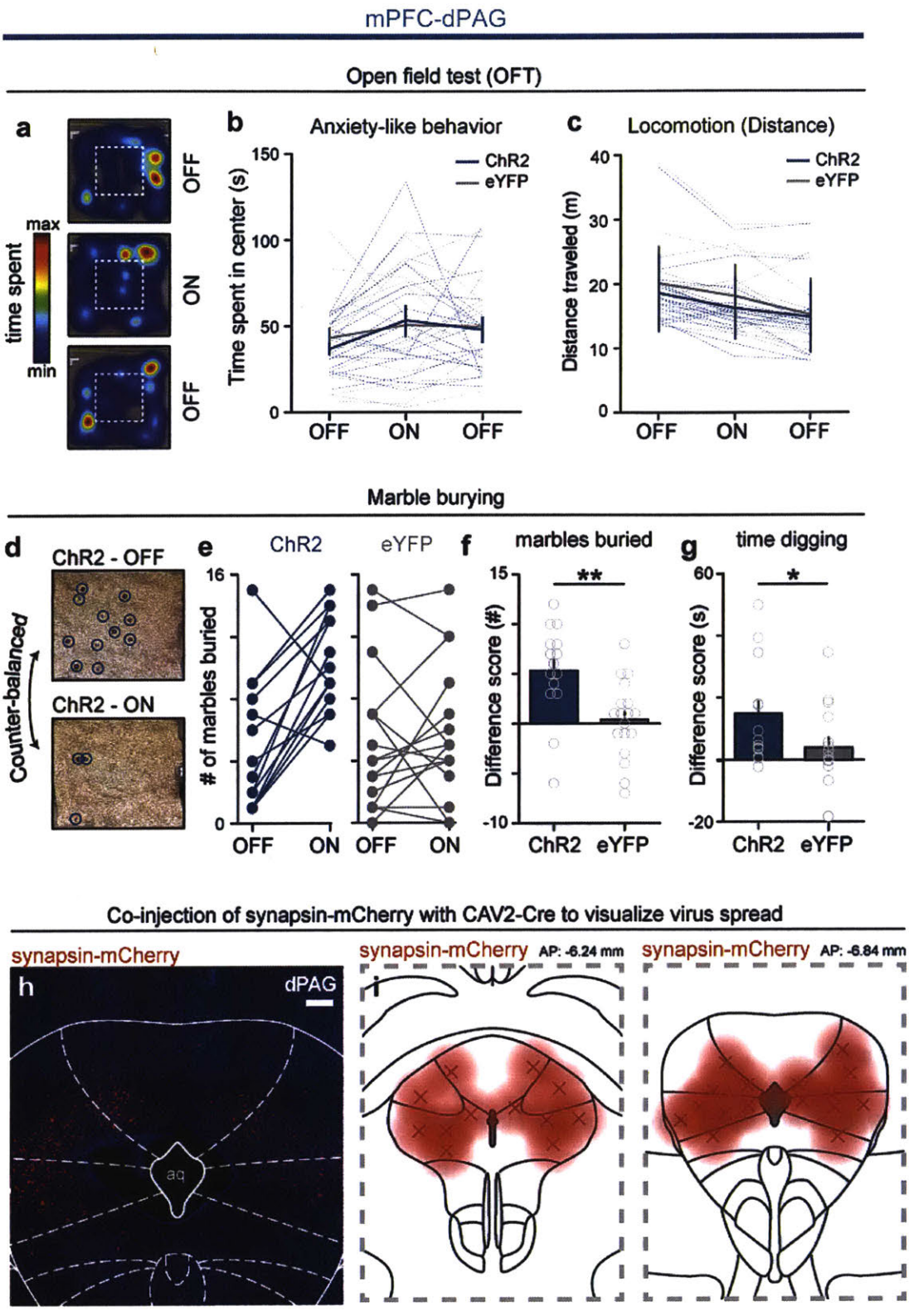
mPFC-dPAG
Open field test (OFT)
a
max
time spent
min
OFF
ON
OFF
b
Anxiety-like behavior
ChR2
eYFP
Time spent in center (s)
150
100
50
0
OFF
ON
OFF
c
Locomotion (Distance)
ChR2
eYFP
Distance traveled (m)
40
30
20
10
0
OFF
ON
OFF
Marble burying
d
ChR2 - OFF
Counter-balanced
ChR2 - ON
e
ChR2
eYFP
# of marbles buried
16
0
OFF
ON
OFF
ON
f
marbles buried
**
Difference score (#)
15
-10
ChR2
eYFP
g
time digging
*
Difference score (s)
60
-20
ChR2
eYFP
Co-injection of synapsin-mCherry with CAV2-Cre to visualize virus spread
synapsin-mCherry
h
dPAG
aq
synapsin-mCherry AP: -6.24 mm
i
synapsin-mCherry AP: -6.84 mm

Figure 12. Activation of mPFC-dPAG neurons increases marble burying.

(a) Representative locomotor heatmaps of a mPFC-dPAG::ChR2 subject during 3 min OFF-ON-OFF epochs in the open-field test (OFT).

(c) Optical activation of mPFC-dPAG::ChR2 did not change time spent in the center region compared to eYFP controls, as measured by time spent in the center of the arena (two-way repeated measures ANOVA, group x epoch, $F_{2,18} = 1.065$, $p > 0.05$)

(c) Optical activation of mPFC-dPAG::ChR2 did not change general locomotor activity (distance traveled, two-way repeated measures ANOVA, group x epoch interaction, $F_{2,18} = 1.156$, $p > 0.05$).

(d) Representative arena of mPFC-dPAG::ChR2 animal after marble burying assay when laser stimulation was OFF (top) and ON (bottom). Sessions were counter-balanced and separated by 24 h.

(e) The number of marbles buried in ON and OFF conditions for mPFC-dPAG::ChR2 (teal, left) and mPFC-dPAG::eYFP (grey, right) rats.

(f) Stimulation of mPFC-dPAG neurons resulted in a greater change in marbles buried by mPFC-dPAG::ChR2 animals compared with mPFC-dPAG::eYFP controls, as measured by difference score [# of marbles buried during ON session – OFF session] (unpaired t-test, $t(33) = 2.979$, $p = 0.005$).

(g) mPFC-dPAG::ChR2 subjects spent more time digging compared to mPFC-dPAG::eYFP controls, as measured by difference score [ON-OFF] (unpaired one-way t-test, $t(27) = 1.961$, $p = 0.0301$).

(h) Representative confocal image of viral spread in the PAG, visualized by co-injection of AAV_5-hSyn-mCherry (hSyn = synapsin, red) with CAV2-Cre in a subset of mPFC-dPAG::ChR2/eYFP expressing rats. Scale bars (histology) = 200 um.

(i) Illustration of reconstructed injection locations and spread in co-injected subjects (n = 14 total, 7 ChR2, 7 eYFP).

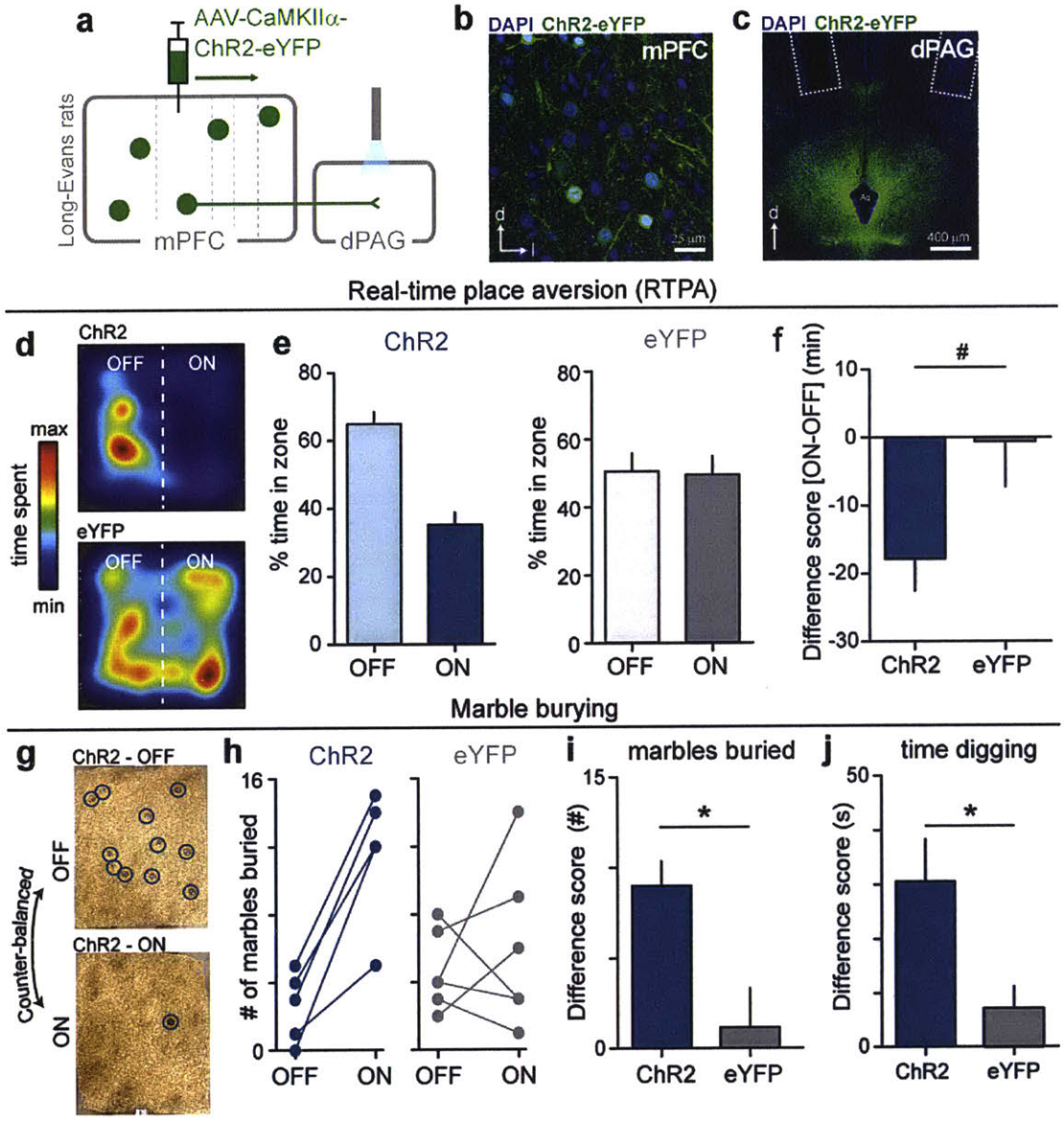

Figure 13. Activation of mPFC terminals in the dPAG evokes marble burying.

(a) Schematic of viral strategy to achieve optogenetic control of ChR2-expressing mPFC terminals in the dPAG.

(b) Representative image of ChR2+ neurons in the mPFC.

(c) Representative image of ChR2+ terminals in the dPAG.

(d) Representative locomotor heatmaps of mPFC-dPAG::ChR2 (top) compared to mPFC-dPAG::eYFP control subject (bottom) in the RTPP/A assay.

(e) Percent of time spent in the ON and OFF zones of the arena in mPFC-dPAG::ChR2 and mPFC-dPAG::eYFP subjects.

(f) Optogenetic stimulation of mPFC terminals in the dPAG resulted in a trend towards avoidance in the real-time place avoidance assay in mPFC-dPAG::ChR2 animals, compared to mPFC-dPAG::eYFP controls (unpaired t-test, $t(11) = 1.830$, $\#p = 0.094$.

(g) Representative arena of mPFC-dPAG::ChR2 animal after marble burying assay when optical stimulation was OFF (top) and ON (bottom).

(h) Number of marbles buried in mPFC-dPAG::ChR2 and mPFC-dPAG::eYFP during OFF and ON sessions.

(i) Optical stimulation of mPFC-dPAG neurons resulted in more marbles buried by mPFC-dPAG::ChR2 animals, compared with mPFC-dPAG::eYFP controls (unpaired t-test, $t(9) = 2.839$, $p = 0.019$).

(j) Optical stimulation of mPFC-dPAG neurons resulted in more time digging in mPFC-dPAG::ChR2 animals compared to mPFC-dPAG::eYFP animals (unpaired, one-tailed t-test, $t(9) = 2.775$, $p = 0.0108$).

Error bars indicate ±SEM.

We identified the ability of optogenetic activation of the mPFC-dPAG projection to mediate place avoidance and defensive behaviors, but acknowledge that such optogenetically-induced activity may not reflect the endogenous function of this circuit. To address this, we next investigated the natural neural dynamics of individual neurons in the mPFC-dPAG and mPFC-NAc populations during receipt of a punishment or a reward. To determine whether mPFC-dPAG neurons preferentially encode aversive stimuli, we performed *in vivo* microendoscopic imaging (Ghosh et al., 2011) of neurons expressing a genetically-encoded calcium indicator (Akerboom et al., 2013; Chen et al., 2013). To compare the responses of mPFC-dPAG and mPFC-NAc neurons in mice, we used the same dual virus approach wherein we injected an anterogradely-traveling viral vector carrying Cre-dependent GCaMP6m (AAV-DIO-GCaMP6m) into the mPFC and CAV2-Cre into the dPAG or NAc (**Figure 14a-b**), which allowed us to visualize changes in intracellular calcium concentration indicative of neural activity. We recorded neural activity during two 15-minute sessions counterbalanced for order, one in which we presented a reward (sucrose solution available from a spout), and another in which we presented an aversive stimulus (foot shock) (**Figure 14c**). Examination of the bulk fluorescence from the entire field of view (FOV) revealed that the mPFC-NAc neural population was not significantly modulated by either shock or sucrose (**Figure 14d-e**). In contrast, mPFC-dPAG neurons showed a robust, time-locked increase in activity in response to foot shock and a decrease in response to sucrose (**Figure 14d-e**).

To assess the activity of individual projection-defined neurons, we used a modified constrained non-negative matrix factorization algorithm (Pnevmatikakis et al., 2016) optimized for micro-endoscopic imaging (CNMF-E) (Zhou et al., 2018) where values were not constrained to non-negative numbers (i.e., C(N)MF-E) considering calcium fluctuations can exhibit negative transients, associated with a pause in firing (Otis et al., 2017). We recorded from 169 mPFC-NAc and 118 mPFC-dPAG neurons. When comparing the normalized responses of cells within

each population in response to foot shock and sucrose, we found heterogeneous mPFC-NAc responses – 19 (11.2%) were activated by foot shock, 17 (10%) to sucrose, and only 1 neuron (0.6%) was responsive to both (**Figure 14h-i**). In contrast, 42 mPFC-dPAG neurons (35.6%) showed phasic excitation to the shock, whereas only 9 (7.7%) were excited by sucrose and 5 neurons (4.2%) were responsive to both (**Figure 14j-k**). Thus, mPFC-dPAG and mPFC-NAc neurons show distinct response patterns to rewarding and aversive stimuli (chi square, X^2 = 10.95, p = 0.0042). When examining individual calcium transients (**Figure 14l**), mPFC-dPAG neurons had transients that were both more frequent (**Figure 14m**) and higher in amplitude (**Figure 14n**) during shock sessions, compared to mPFC-NAc neurons. Importantly, when the data set was analyzed by a different, ROI-based analysis approach, preferential shock responsivity was again observed in mPFC-dPAG projectors (**Figure 15**).

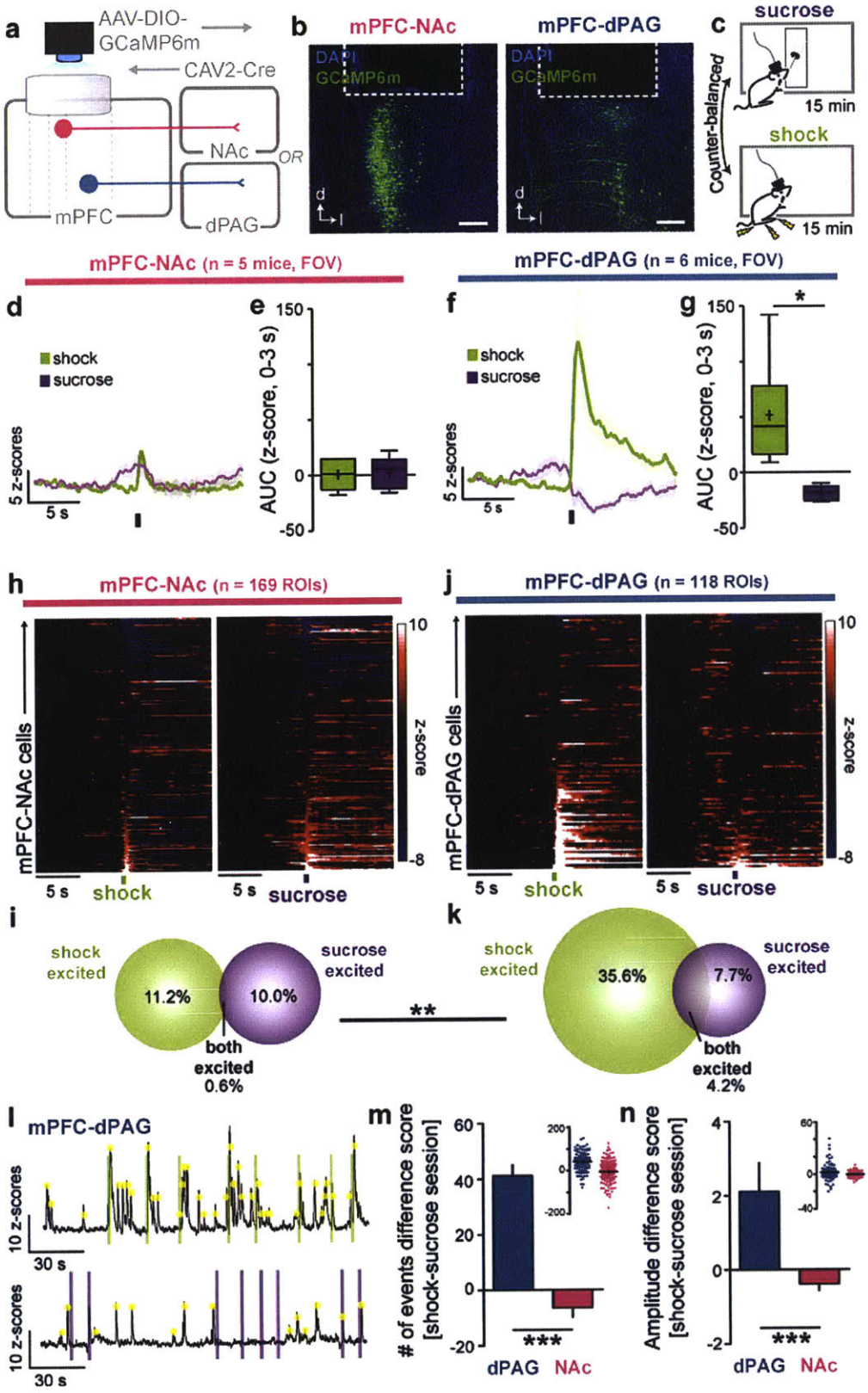
a
AAV-DIO-GCaMP6m
CAV2-Cre
NAc
OR
mPFC
dPAG
b
mPFC-NAc
mPFC-dPAG
DAPI
GCaMP6m
c
sucrose
15 min
Counter-balanced
shock
15 min
mPFC-NAc (n = 5 mice, FOV)
mPFC-dPAG (n = 6 mice, FOV)
d
shock
sucrose
5 z-scores
5 s
e
AUC (z-score, 0-3 s)
150
0
-50
f
shock
sucrose
5 z-scores
5 s
g
AUC (z-score, 0-3 s)
150
0
-50
*
h
mPFC-NAc (n = 169 ROIs)
mPFC-NAc cells
10
z-score
-8
5 s
shock
5 s
sucrose
j
mPFC-dPAG (n = 118 ROIs)
mPFC-dPAG cells
10
z-score
-8
5 s
shock
5 s
sucrose
i
shock excited
sucrose excited
11.2%
10.0%
both excited 0.6%
**
k
shock excited
sucrose excited
35.6%
7.7%
both excited 4.2%
l
mPFC-dPAG
10 z-scores
30 s
10 z-scores
30 s
m
# of events difference score [shock-sucrose session]
60
40
20
0
-20
200
0
-200
***
dPAG
NAc
n
Amplitude difference score [shock-sucrose session]
4
2
0
-2
60
0
-40
***
dPAG
NAc

Figure 14. mPFC-NAc neurons exhibit heterogeneous responses to rewarding and aversive stimuli, while mPFC-dPAG neurons preferentially respond to aversive stimuli.

(a) Schematic of strategy for monitoring neuronal activity in mPFC-dPAG and mPFC-NAc neurons using *in vivo* epifluorescent calcium imaging.

(b) dPAG- and NAc-projecting mPFC neurons were transduced with GCaMP6m using a dual viral strategy and imaged through an implanted relay lens using a detachable head mounted mini-microscope.

(c) Dynamic calcium fluctuations were monitored during a 15 min recording session where mice were allowed to self-administer sucrose via a sucrose lickometer or had random, unsignaled foot shocks delivered.

(d) Bulk fluorescence across the entire field of view (FOV) aligned to foot shock onset (green trace) and the initiation of a sucrose consumption bout (purple trace) in mPFC-NAc::GCaMP6m neurons (n = 5 mice).

(e) mPFC-NAc::GCaMP6m bulk calcium responses to sucrose did not differ from responses to foot shock (0-3 s AUC, paired t-test, $t(4)=0.1482$, $p = 0.8893$).

(f) Bulk fluorescence across the FOV aligned to foot shock onset (green trace) and the initiation of a sucrose consumption bout (purple trace) in mPFC-dPAG::GCaMP6m neurons (n = 6 mice).

(g) mPFC-NAc::GCaMP6m bulk calcium responses to foot shock were greater than those to sucrose bout initiation (0-3 s AUC, paired t-test, $t(5)=3.743$, $p = 0.0134$).

(h) Calcium signals were extracted from individual ROIs and the average calcium traces per ROI were aligned to shock and sucrose bout onset (heatmaps of z-scores) for both mPFC-NAc::GCaMP6m (n = 169 ROIs) and **(j)** mPFC-dPAG::GCaMP6m (n = 118 ROIs) recordings.

(i-k) The distribution of shock and sucrose excited cells for mPFC-dPAG::GCaMP6m neurons was different from mPFC-NAc::GCaMP6m neurons (chi square, $X^2 = 10.95$, $p = 0.0042$). Notably, more mPFC-dPAG::GCaMP6m neurons were excited to foot shock.

(l) Representative calcium traces from a mPFC-dPAG::GCaMP6m neuron during shock (top) and sucrose (bottom) recording sessions. Individual calcium transients (yellow dots) were identified and quantified.

(m) mPFC-dPAG::GCaMP6m neurons had more frequent calcium transients during the entire 15 min shock session compared the sucrose session (data not shown, one-sample Wilcoxon signed rank, $p < 0.0001$), and the number of transients was significantly greater than mPFC-NAc::GCaMP6m neurons (# of events difference score [shock-sucrose]), unpaired Wilcoxon signed rank, $p < 0.0001$), which did not exhibit differences in the number of events between sessions (data not shown, one-sample Wilcoxon signed rank, $p = 0.1251$).

(n) mPFC-dPAG::GCaMP6m neurons had higher amplitude calcium transients during the entire 15 min shock session compared to the sucrose session (data not shown, one-sample Wilcoxon signed rank, $p = 0.0022$), or compared to mPFC-NAc::GCaMP6m neurons (amplitude of events difference score [shock-sucrose]), unpaired Wilcoxon signed rank, $p < 0.0001$). In contrast, mPFC-NAc::GCaMP6m neurons showed greater amplitude events during the sucrose session compared with shock (data not shown, one-sample Wilcoxon signed rank, $p = 0.0345$).

Error bars indicate ±SEM. AUC = area under the curve. FOV = field of view.

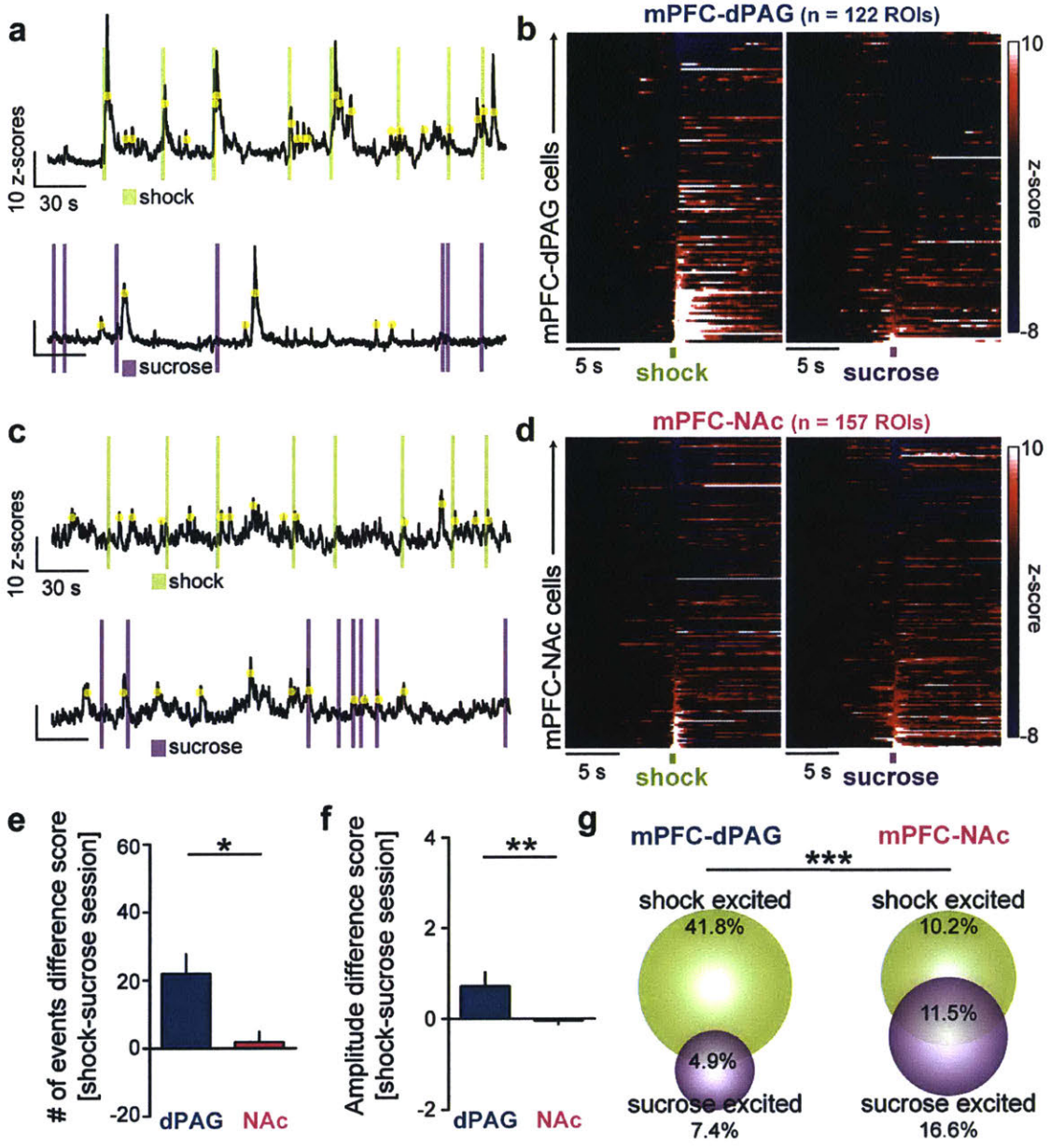

Figure 15. ***In vivo*** **calcium imaging re-analyzed with a background subtracted ROI approach.**

(a) Calcium transients (yellow dots) within individual mPFC-dPAG::GCaMP6m neurons (n = 108).

(b) mPFC-dPAG::GCaMP6m neurons aligned to footshock (left) and sucrose (right).

(c) Calcium transients (yellow dots) within individual mPFC-NAc::GCaMP6m neurons (n = 157).

(d) mPFC-NAc::GCaMP6m neurons aligned to footshock (left) and sucrose (right).

(e) mPFC-dPAG::GCaMP6m neurons had more frequent calcium transients during the entire 15 min shock session compared the sucrose session (data not shown: one-sample Wilcoxon signed rank, $p < 0.0001$), and was significantly greater than mPFC-NAc::GCaMP6m neurons (difference score [shock-sucrose], unpaired Wilcoxon rank sum text, $p = 0.0057$), which did not exhibit a difference in transient frequency between the two session (data not shown: one-sample Wilcoxon signed rank, $p = 0.3468$).

(f) mPFC-dPAG::GCaMP6m neurons had larger calcium transients during the entire 15 min shock session compared the sucrose session (data not shown: one-sample Wilcoxon signed rank, $p = 0.0081$), and this was significantly greater than mPFC-NAc::GCaMP6m neurons (difference score [shock-sucrose] unpaired Wilcoxon rank sum test, $p = 0.0057$), which had similar transient amplitude during both sessions (one-sample Wilcoxon signed rank, $p = 0.5021$).

(g) The distribution of shock and sucrose excited cells for mPFC-dPAG::GCaMP6m neurons were different from mPFC-NAc::GCaMP6m neurons (chi square, $X^2 = 32.33$, $p < 0.0001$).

Error bars indicate ±SEM.

Experimental Procedures

General virus surgery.

Specific subject/surgery details for each experiment are detailed below. For all subjects, surgeries were performed under aseptic conditions and body temperature was maintained with a heating pad. Rodents were anesthetized with isoflurane mixed with oxygen (5% for induction, 2.5-2% for maintenance, 1L/min oxygen flow rate) and placed in a digital small animal stereotax (David Kopf Instruments, Tujunga, CA, USA). Following initial induction, hair was removed from the dorsal surface of the head with hair clippers, ophthalmic ointment was applied to the eyes, the incision area was scrubbed with alcohol pads and betadine (x3 each), and 2% lidocaine was injected just under the skin surface above the skull for topical anesthesia. All measurements were made relative to bregma (unless noted otherwise) for virus/implant surgeries. Viral injections were performed using a beveled microinjection needle (26 gauge for rat; 33 gauge for mice) with a 10 µL microsyringe (Nanofil; WPI, Sarasota FL, USA) delivering virus at a rate of 0.05-0.01 µL/min using a microsyringe pump (UMP3; WPI, Sarasota, FL, USA) and controller (Micro4; WPI, Sarasota, FL, USA). For injections at multiple locations on the dorsal-ventral axis, the most ventral location was completed first and the injection needle was immediately relocated to the more dorsal location and initiated. After injection completion, 15 mins were allowed to pass before the needle was slowly withdrawn. After viral infusions were completed, craniotomies were filled with bone wax and the incision closed with nylon sutures. Subjects were maintained under a heat lamp and provided 0.05 mg/kg (rat) / 0.10 mg/kg (mouse) buprenophine (s.c., diluted in warm Ringers solution) until fully recovered from anesthesia.

All experiments involving the use of animals were in accordance with NIH guidelines and approved by the MIT Institutional Animal Care and Use Committee. For all experiments involving viral or tracer injections, animals containing mistargeted injection(s) were excluded

after histological verification. Sample size was based on reports in related literature and were not predetermined by calculation.

Viral constructs

Recombinant AAV_5 vectors carrying ChR2 or fluorescent proteins (mCherry or eYFP) were packaged by the University of North Carolina Vector Core (Chapel Hill, NC, USA). AAV_8-hSyn-FLEX-ChrimsonR-tdTomato and AAV_5-hSyn-mCherry was packaged by the University of North Carolina Vector Core (Chapel Hill, NC, USA). Viruses carrying GCaMP6m were packaged by the University of Pennsylvania Vector Core (Philadelphia, PA, USA). We recognize the generosity of the Genetically-Encoded Neuronal Indicator and Effector (GENIE) program, the Janelia Farm Research Campus, Drs. Vivek Jayaraman, Rex A. Kerr, Douglas S. Kim, Loren L. Looger, Karel Svoboda for providing GCaMP6m. Canine adeno-associated virus carrying Cre recombinase (CAV2-Cre 4.2x10 infectious units/mL) was packaged and obtained from the Istitut de Génétique Moléculaire de Montpellier, France from Dr. Eric Kremer. AAV_9-hEF1a-DIO-synaptophysin-mCherry was packaged from Dr. Rachael Neve at the Viral Gene Transfer Core Facility at MIT (now located at Massachusetts General Hospital). We thank Dr. Eric J. Kremer for providing CAV2-Cre vector, UNC vector core for ChR2, NpHR, and ChrimsonR vectors, and University of Pennsylvania vector core for GCaMP6m packaging. We recognize Dr. Rachel Neve (formerly at the Gene Transfer Core Facility at MIT, now located at Massachusetts General Hospital) for packaging the AAV-DIO-synaptophysin-mCherry construct.

Retrograde cholera toxin-B tracing

Rats.

Male wild-type Long-Evans rats (~220g; Charles Rivers Laboratories, NC, USA) were dual housed on a normal 12h:12h light/dark cycle (lights on at 09:00 AM). Rats were prepared

for stereotaxic surgery as described above using the viral infusion parameters also described above (under *general virus surgery*). Briefly, 500 nl of cholera toxin subunit B (CTB) conjugated to Alexa Fluor-488, 555, or 647[17] (0.1%, Molecular Probes, Eugene, OR, USA) was injected into the dorsal periaqueductal gray (dPAG; AP: -6.6, ML: -0.6; DV: -5.4 mm) and NAc shell (AP: +1.5, ML: +0.95, DV: -7.5 mm) (color counterbalanced between animals). After 7 days, rats were transcardially perfused and histologically prepared. Z-stack stitches encompassing both prelimbic (PL) and intralimbic (IL) regions of the mPFC were acquired using a scanning confocal microscope (Olympus FV1000) with Fluoview software (Olympus, Center Valley, PA, USA) under a 40x/1.30 NA oil immersion objective. Quantification of fluorescence intensity across layers was accomplished by analyzing 200w x 400h µm sections encompassing ventral PL / dorsal IL across mPFC layers based on DAPI density/morphology in FIJI ImageJ. Sections were normalized to the section with peak fluorescence within subjects. For cell quantification, the number of CTB positive and double-positive neurons was counted in both the IL and PL subregions of the mPFC using FluoView software (Olympus, Center Valley, PA). To examine potential projections from the VTA to the dPAG 14 VTA sections were immunstained for tyrosine hydroxylase (TH) (see below) and Z-stacks were captured under a 40x/1.30 NA oil immersion objective. In each stack, 100 DAPI+ cells were identified and the proportion of TH+ and CTB+ cells were counted. Sample size was based on reports in related literature and were not predetermined by calculation.

Mice.

Adult male wild-type C56BL/6 mice (~10 wks; Jackson Laboratory, Bar Harbor, ME) were prepared similarly to methods described above. Briefly, 350 nl of Cholera Toxin subunit B (CTB) conjugated to Alexa Fluor-488, 555, or 647 (Molecular Probes, Eugene, OR, USA) was injected into the dorsal periaqueductal gray (dPAG; AP: -4.2, ML: -0.5; DV: -2.4 mm) and NAc

shell (AP: +1.0, ML: +0.75, DV: -4.5 mm) (color counterbalanced between animals). Histological, imaging, and data analyses are the same as previously described.

Projection-specific behavioral optogenetic experiments

mPFC-dPAG and mPFC-NAc Subjects.

Male wild-type Long-Evans rats (~220g; Charles Rivers Laboratories) were dual housed on a normal 12h:12h light/dark cycle (lights on at 09:00 AM). ~1 weeks following viral injection surgeries, rats were individually housed with restricted food access (~16-20 g chow / day) for ~10 weeks, but retained *ad libitum* access to water. Rats were maintained on food restriction unless noted otherwise.

Surgery.

For projection-specific targeting for behavioral optogenetic, male wild-type Long-Evans rats were bilaterally injected with 1.2 µL of AAV_5-Ef1a-DIO-ChR2(H134R)-eYFP in the mPFC at 2 locations along the dorsal-ventral axis (0.6 µL each) (AP: +3.2; ML: ±0.75; DV: -3.5 and -2.5; mm relative to bregma). To achieve projection-specific recombination, retrogradely traveling canine adeno-associated (CAV) virus carrying Cre-recombinase (CAV2-Cre; $4.2x10^{12}$ infectious units/mL; Istitut de Genetique Moleculaire de Montpellier, France) was bilaterally injected (0.6 µL each) in the dorsal periaqueductal gray (dPAG) (AP: -6.0; ML: ±0.6; DV: -5.2; mm relative to bregma [0.4 ul]), or nucleus accumbens (NAc) (AP: +1.4; ML: ±1.0; DV: -7.4; mm relative to bregma [0.5 µL]). A subset of mPFC-dPAG rats were co-injected with 0.1 ul of AAV^5-hSyn-mCherry to visualize virus spread. ~7 days following virus surgery, rats were individually housed and placed on food restriction. ~10 weeks later, manually constructed optic fibers (400 µm core, 0.48 NA) (Thorlabs, Newton, NJ, USA) held in a 2.5 mm ferrule (Precision Fiber Products, Milpitas, CA, USA) were implanted directly above ChR2/eYFP-expressing mPFC

neurons projecting to either the dPAG or NAc for projection-specific manipulations (AP: +3.2-3.6; ML: ±1.5, DV: -2.8; mm relative to bregma at a 10° angle, bilateral).

For terminal manipulations, AAV_5-CaMKIIa-ChR2-eYFP was bilaterally injected into the mPFC at 2 locations along the dorsal-ventral axis (0.6 µL each) (AP: +3.2; ML: ±0.75; DV: -3.5 and -2.5; mm relative to bregma). ~7 days following surgery, rats were individually housed and placed on food restriction. ~10 weeks later, manually constructed optic fibers (400 µm core, 0.48 NA) (Thorlabs, Newton, NJ, USA) held in a 2.5 mm ferrule (Precision Fiber Products, Milpitas, CA, USA) were bilaterally implanted directly above the dPAG for mPFC terminal manipulations (AP: -6.6, ML: ±1.5, DV: -4.3 mm relative to bregma at a 10° angle, bilateral). For both experiments, optical fibers were secured to the skull with 2-4 skull screws, a layer of adhesive cement (C&B Metabond; Parkell, Edgewood, NY, USA), followed by black cranioplastic cement (Ortho-Jet; Lang, Wheeling, IL, USA) containing gentamicin antibiotic. The implant was allowed to completely dry before closure of the incision with nylon sutures.

Behavioral testing.

Testing was performed at ~13 wks following viral injection and ~10 days after optical fiber implantation to allow sufficient time for transgene expression and tissue recovery. Throughout this period, rats were maintained on food-restriction (~16-20 g chow / day). Rats were tested during their light phase (09:30 AM – 07:00 pm) under food-deprived conditions. Optic fiber implants were connected to a 200 um patch cable (Doric, Québec, Canada) using a ceramic sleeve (PFP, Milpitas, CA), which connected to a bilateral commutator (rotary joint; Doric, Québec, Canada) by means of an FC/PC adapter to allow unrestricted movement. A second patch cable, with an FC/PC connector at either end (Doric, Québec, Canada), connected the commutator to a 473 nm diode-pumped solid state (DPSS) laser (OEM Laser Systems, Draper, UT). A Master-8 pulse stimulator (A.M.P.I., Jerusalem, Israel) was used to control the output of the 473 nm laser, with a light power of ~10-15 mW (adjusted to account for

optic fiber efficiency). Following each day's experimentation, rats were provided their ~16-20 grams of standard chow.

Real-time place preference / aversion.

Individual food-restricted rats were placed in a Plexiglas arena (24l x 24w in x 20h in) and were allowed to freely move between two compartments for 1 hr in a dimly lit room containing constant white noise (Marpac Dohm-DS dual speed sound conditioner, Wilmington, NC, USA). Entry into one half of the chamber resulted in photostimulation (VTA^{DA}-mPFC::ChR2/eYFP = unilateral 20 Hz, 60 p, 5 ms pulses every 30 s, 20 mW; mPFC-dPAG/NAc::ChR2/eYFP = bilateral 20 Hz 5 ms pulses, 12-15 mW, *see below*). Stimulation and no stimulation sides were counterbalanced between animals. Rats were tested on 2 consecutive days and on the second day; the stimulation side and no stimulation side were reversed. A video camera positioned directly above the arena tracked and recorded movement using EthoVision XT (Noldus, Wageningen, Netherlands). All data presented are tracked from the "center" of the subject and time spent in each zone was averaged across the 2 testing sessions. In between subjects, the behavioral chamber was thoroughly cleaned with 10% glass cleanser diluted in ddH20.

Conditioned place preference / aversion.

Individual food-restricted rats were placed in a Plexiglas arena (30l x 15w in x 25h in) divided into two compartments: one with vertical stripes and the other with horizontal stripes. On day 1 (habituation), rats were allowed to freely move between two compartments for 15 min in a brightly lit room containing constant white noise (Marpac Dohm-DS dual speed sound conditioner, Wilmington, NC, USA). Movement was tracked by an overhead video camera positioned above the arena and time spent in each compartment was calculated using EthoVision XT (Noldus, Wageningen, Netherlands). On day 2 and 3, rats were exposed to conditioning sessions (20 min ea, 1 per day) during which they were confined to one side of the

chamber and received optical stimulation (VTA^{DA}-mPFC::ChR2/eYFP = unilateral 20 Hz, 60 p, 5 ms pulses every 30 s, 20 mW; mPFC-dPAG/NAc::ChR2/eYFP = bilateral 20 Hz 5 ms pulses, 12-15 mW, *see below*) or no stimulation (counterbalanced for order and side across animals). On day 4 (test), rats were placed in the chamber and allowed to freely explore both compartments in the absence of optical stimulation. Again, movement was tracked by an overhead video camera positioned above the arena using EthoVision XT (Noldus, Wageningen, Netherlands) and a time difference score was calculated by subtracting the time spent in the stimulation-paired compartment on the habituation day from the time spent in the stimulation-pared compartment on the test day (test[time spent in paired side] – habituation[time spent in paired side]).

Open field test.

Individual food-restricted rats were placed in a Plexiglas arena (24l x 24w x 20h in) and were allowed to move freely within the arena for 9 min with light stimulation occurring during the middle 3 min (3 min OFF, 3 min ON, 3 min OFF design) (mPFC-dPAG/NAc::ChR2/eYFP = bilateral 20 Hz 5 ms pulses, 12-15 mW). The room was brightly lit and contained constant white noise (Marpac Dohm-DS dual speed sound conditioner, Wilmington, NC, USA). A video camera positioned directly above the arena tracked and recorded movement using EthoVision XT (Noldus, Wageningen, Netherlands). In order to assess anxiety-related behavior, the chamber was divided into a center (40 x 40 cm) and periphery region. In between subjects, the behavioral chamber was thoroughly cleaned with 3% acetic acid diluted in ddH20. All data presented are tracked from the "center" of the subject.

Marble burying.

Individual food-restricted rats were placed in a standard, rectangular rodent cage (33w x 40l x 20h cm) containing ~7.5 cm of clean standard bedding and 16 black marbles, which was slightly elevated from the floor (1 m). 16, 1.3 cm diameter black marbles were placed on top of

the even bedding in a 4 x 4 array separated from the cage sides by ~5 cm. Rats were tested across 2 days for 12 min each, counter-balanced for laser stimulation (mPFC-dPAG::ChR2/eYFP = bilateral 20 Hz 5 ms pulses, 12-15 mW) in a brightly lit room containing constant white noise (Marpac Dohm-DS dual speed sound conditioner, Wilmington, NC, USA). Behavior was recorded via a video camera positioned directly above the arena using Ethovision XT (Noldus, Wageningen, Netherlands). Photographs of the behavioral arena before (undisturbed) and after each 12 min session were obtained and marbles that were 100% buried were counted. Time spent digging was scored by two experimenters blind to condition using ODLog (Macropod). Cage exploration time was obtained by subtracting the time spent of scored behaviors from the total session length. The time spent engaging in each behavior was quantified by taking the average between the two experimenters. One mPFC-dPAG::ChR2 video was corrupted and was not included in analyses. In between subjects a new cage containing fresh bedding was used and marbles were cleaned with 15% isopropyl alcohol diluted in ddH20.

Following the conclusion of experiments, a subset of rats were stimulated for 5 min in a dark, sound-attenuating room (473 nm, 20 Hz, 20 mW, 5 ms pulses) for c-Fos quantification to verify light-evoked activity in ChR2+ mPFC-dPAG neurons. 80 mins later, rats were deeply anesthetized and transferred to the lab and transcardially perfused.

In vivo epifluorescent calcium imaging

Projection-specific subjects.

Male wild-type C57BL/6 mice (~8 wks old; mPFC-dPAG::GCaMP6m and mPFC-NAc::GCaMP6m) or male DAT::IRES-Cre mice (~ 8 wks old; mPFC-dPAG::GCaMP6m + VTA^{DA}::ChrimsonR/mCherry) were group housed (2-4 subjects per cage) on a 12h:12h reverse

light/dark cycle (lights off at 09.00 AM) prior to and 4 weeks following initial virus and microendoscope (i.e., GRIN lens) implant surgery. Following baseplate adhesion, subjects were individually housed and placed on food restriction (3-6 grams normal chow / day) with *ad libitum* access to water for 3-6 days encompassing testing. Sample sizes was based on reports in related literature and were not predetermined by calculation.

Surgeries.

Subjects were prepared for *in vivo* epifluorescent calcium imaging similarly to methods described elsewhere (Jennings et al., 2015; Resendez et al., 2016). Briefly, to achieve projection-specific imaging, a virus encoding Cre-dependent GCaMP6m (AAV_5-CAG-Flex-GCaMP6m) was injected into the mPFC (AP: +1.8, ML: +0.3, DV: -2.75 & -2.4 [300 nl ea, bevel facing lateral]) and retrogradely traveling canine adeno-associated (CAV) virus carrying Cre-recombinase (CAV2-Cre; Istitut de Génétique Moléculaire de Montpellier, France) was injected into the dPAG (n = 6; AP: -4.2, ML: +0.5, DV: -2.4 [350 nl]) or the nucleus accumbens shell (n = 5; AP: +1.0, ML: +0.75; DV: -4.5 [350 nl]). After virus infusions, the mPFC craniotomy was enlarged to >1 mm in diameter and dura removed with a bent 30 gauge beveled needle, but no tissue was aspirated. A 1 mm diameter, ~4 mm length gradient refractive index lens (GRIN lens; GLP-1040, Inscopix, Palo Alto, CA) was held via vacuum on the tip of a blunted needle surrounded by plastic tubing for stability and was lowered stereotaxically through the craniotomy under constant saline perfusion to minimize tissue/blood desiccation. Lenses were implanted slightly posterior and lateral of the needle track for virus infusions to avoid tissue damage in the imaging plane, and were lowered to locations in the ventral PL / dorsal IL subregion of the mPFC (AP: -1.77, ML: -0.4, DV: -2.32, mm from bregma). Lens implants were secured to the skull with a thin layer of adhesive cement (C&B Metabond; Parkell, Edgewood, NY, USA), followed by black cranioplastic cement (Ortho-Jet; Lang, Wheeling, IL, USA) containing gentamicin antibiotic. Lenses were covered with the top of an eppendorf tube and cemented in

place with cranioplastic cement for protection during the virus incubation period (3-4 wks). The implant was allowed to completely dry before closure of the incision with nylon sutures.

Following virus incubation, mice were again anesthetized with isofluorane, streotaxically secured, and baseplates (Inscopix, Palo Alto, CA) were cemented around the lens to support the connection of the miniaturized microscope for *in vivo*, freely moving imaging. During this procedure, the protective eppendorf cap and supporting cranioplastic cement were removed using a hand drill. The exposed top of the GRIN lens was scrubbed clean with a cotton-tipped applicator soaked with 15% isopropyl alcohol diluted in ddH_20. Next, a miniaturized microscope (single channel epifluorescence, 475 nm blue LED, Inscopix, Palo Alto, CA) with the baseplate attached was stereotaxically positioned over the implanted GRIN lens and adjusted in the DV axis in order to focus on visible landmarks (i.e., GCaMP6m expressing neurons and blood vessels). After the focal plane was identified, the microscope/baseplate was raised by ~50 um, to account for cement shrinkage, and was subsequently cemented in place with pink dental cement (Stoelting, Wood Dale, IL, USA). The microscope was then detached from the baseplates, a final layer of black cranioplastic cement (Ortho-Jet; Lang, Wheeling, IL, USA) was applied to prevent light leak, and the implant was covered with a protective plate (Inscopix, Palo Alto, CA) until imaging.

Behavioral sucrose/shock paradigm and data acquisition.

Following recovery (~7 days), mice were individually housed and food restricted for 2 days and exposed to 30% sucrose solution (diluted in standard tap/cage H20) in the homecage. Food-deprived mice were then trained in operant chambers equipped with sucrose lickometers (Med Associates, St Albans, VT), with a modified spout that extended into the chamber from the recessed opening, for ~60 min while connected to a plastic "dummy" microscope for training and habituation. All animals readily self-administered sucrose via the lickometer after 2 days of training. On the testing day, food-deprived mice were gently restrained and connected with the

miniaturized microscope (single channel epifluorescence, 475 nm blue LED, Inscopix, Palo Alto, CA) via the baseplate and secured with a small screw on the baseplate. Mice were allowed to recover from restraint for 10 min before the first session was initiated. Mice were exposed to two 15-minute imaging sessions ("sucrose" and "shock"), counter-balanced and separated by a 15 min intermediate epoch, during which the animal remained in the chamber, but no sucrose or footshocks were administered. During "sucrose" sessions, food deprived mice were allowed to self-administer sucrose for 15 min via the lickometer they had been exposed to previously. During "shock" sessions, mice were exposed to 27 mild electric food shocks (0.2 mA; 1 s duration; 10-60 inter-shock interval) for 15 min. Gray scale tiff images were collected at 20 frames per second using 20-60% of the miniaturized microscope's LED transmission range (nVista HD V2, Inscopix, CA).

Image processing.

Image processing was accomplished using Mosaic software (Version 1.1.2., Inscopix, Palo Alto, CA). Raw videos were pre-processed by applying x4 spatial downsampling to reduce file size and processing time, and isolated dropped frames were corrected. No temporal downsampling was applied. For sucrose/shock experiments, both recordings per animal (i.e., "Sucrose" recording and "Shock" recording) were concatenated to generate a single 30 min video. Lateral movement was corrected for by using a portion of a single reference frame (typically a window surrounding a prominent blood vessel or constellation of bright neurons). Images were cropped to remove post-registration borders and sections where cells were not observed. 2 method were used for ROI identification and single-cell fluorescence trace extraction in order to verify that these processes did not significantly change the pattern of results within our data sets. Both methods are described below in *CNMF-E analyses* and *non-ROI analyses*.

CNMF-E analyses.

After motion correction and cropping, recordings were exported as .tif z-stacks and were downsampled to 10 frames per second. We used a constrained non-negative matrix factorization algorithm optimized for micro-endoscopic imaging (CNMF-E) (Zhou et al., 2018) was used to extract fluorescence traces from ROIs. ROIs were defined by manually selecting seed pixels from peak-to-noise (PNR) graphs of the FOV (Murugan et al., 2017). Considering calcium fluctuations can exhibit negative transients, associated with a pause in firing (Otis et al., 2017), we did not constrain values to > 0 – as such we refer to this process as "C(N)MF-E".

Non-ROI analyses.

After motion correcting and cropping, recordings were converted to a changes in fluorescence compared to background fluorescence (F-F0)/F0 using the mean Z-projection image of the entire movie as reference (F0). Calcium signals arising from individual regions of interest (ROIs, i.e., cells) were identified using independent and principal component analyses (PCA/ICA). Identified PCA/ICA filters were thresholded at their half-max values to define possible ROIs. ROIs were then screened for neuronal morphology and only accepted if the threshold filters included only on contiguous region with an eccentricity of <0.85 and an area between 30-350 pixels. Accepted ROI filters were merged if their areas overlapped by more than 60% after visual confirmation. The accepted ROI filters were then reapplied to the motion corrected videos to extract dF/F0 traces for each ROI. In order to correct for bleaching and possible neuropil contamination of the extracted ROI trace, we correct each ROI tracing using signals from the whole field, using a multiple step procedure: The full ROI trace and the signals from the whole field were filtered using a 30 s median filter to eliminate the influence of sharp transients or outliers. The influenced of the surrounding signals on the ROI trace were quantified using regression (*glmfit* in MATLAB). The resulting regression coefficient was then applied to the original, unfiltered trace to regress out the influence of the non-ROI thresholded field on the ROI trace itself. Multiple background subtraction were examined and a non-ROI thresholded

approach was implemented because 1) this approach excludes subtraction of prominent processes (i.e., dendrites and axons) observed in our data set, 2) the reasonable correlation coefficients between individual ROIs (i.e., within the range that would expected based on electrical recordings). To acquire the non-ROI thresholded image for background subtraction, max Z-projections of individual recordings were created and thresholded to separate ROIs and their processes from the rest of the field of view. Average signal from the remaining pixels was used as a proxy for the whole field changes in fluorescence, and regressed of the signal from each ROI.

Data analysis.

Calcium event quantifications (number and amplitude) were performed in MiniAnalysis (Synaptosoft, Decatur, GA) using individual ROI traces from the entire session after conversion to z-score. Baseline from the z-transform was computed by thresholding the signal at 20% of the signal amplitude. Calcium events with z-scores <8 or did no did not have a > 0.5 AUC were not included in analyses because events of this magnitude were did not reliably retain transient, calcium-event characteristics across animals. ROIs which did not contain events that met event criterion were excluded.

We thank Drs. Ilana Witten, Courtney Cameron, Nathan Parker, Malavika Murugan, Pengcheng Zhou and Liam Paninski for advice and code for CNMF-E analysis. We thank Dr. Mark Schnitzer for advice regarding data analyses and endoscopic imaging. The authors wish to acknowledge Inscopix, Inc. for a scientific collaboration – particularly Lara Cardy and Dr. Alice Stamatakis of Inscopix, Inc. for technical assistance.

Histology

Perfusion and storage.

Subjects were deeply anesthetized with sodium pentobarbital (200 mg/kg; i.p.) and transcardially perfused with 15 mL (mouse) / 60 mL (rat) of Ringers solution followed by 15 mL (mouse) / 60 mL (rat) of cold 4% paraformaldehyde (PFA) dissolved in 1x PBS. Animals were decapitated and the brain was extracted from the cranial cavity and placed in 4% PFA solution and stored at 4 °C for at least 48 hrs. 36 hrs before tissue sectioning, brains were transferred to 30% sucrose solution dissolved in 1x PBS at room temperature. Upon sinking, brains were sectioned at 60 um on a freezing sliding microtome (HM420; Thermo Fischer Scientific). Sections were stored in 1x PBS at 4 °C until mounting and imaging.

Confocal microscopy.

Fluorescent images were captured using a confocal laser scanning microscope (Olympus FV1000), with FluoView software (Olympus, Center Valley, PA), under a dry 10x / 0.40 NA objective, a 60x/1.42 NA oil immersion objective, or a 40x /1.30 NA oil immersion objective. The locations of opsin expression, injection site, and lesion from the optic fiber placement were determined by taking serial z-stack images through the 10x objective across a depth of 20-40 µm, with an optical slice thickness of 5-8 µm. High magnification images fluorescence quantifications were obtained through the 40x or 60x objective using serial z-stack images with an optical slice thickness of 3-4 µm (5 slices) using matched parameters and imaging locations. Fluorescence (in arbitrary units) was obtained from analysis in FIJI ImageJ. For quantitation of fluorescence across layers in the mPFC, measurements were normalized to the Z-stack containing the maximum value.

Statistics

Statistical analyses were performed using GraphPad Prism (GraphPad Software, Inc, La Jolla, CA) and MATLAB (Mathworks, Natick, MA). Group comparisons were made using one-

way or two-way ANOVAs followed by Bonferroni post-hoc tests to control for multiple comparisons. Paired and unpaired two-way Student's t-tests were used to make single-variable comparisons. Unpaired one-way t-tests were used to make comparisons with a priori hypotheses (time spent digging in marble burying assay). Tests for binomial distribution were also used on single populations. Non-parametric Wilcoxon signed rank tests were used to make comparisons between non-parametric data (*in vivo* calcium-imaging). Chi square tests were used to compare distribution of shock and sucrose responsive cells between mPFC-dPAG and mPFC-NAc. All statistical tests are two-sided unless otherwise noted as an *a priori* hypothesis. Thresholds for significance were placed at $*p < 0.05$, $**p < 0.01$, $***p < 0.001$. All data are shown as mean ± standard error of the mean (SEM).

Summary

These data show that mPFC-dPAG and mPFC-NAc subpopulations are anatomically and functionally distinct. mPFC-dPAG encode aversive stimuli and promote avoidance, whereas mPFC-NAc responses to rewarding and aversive stimuli are diverse and neither support place preference nor avoidance.

Author Contributions

Conception. Caitlin M. Vander, Edward Nieh, Kay M. Tye

Surgical injections and implantations. Caitlin M. Vander Weele, Cody A. Siciliano. Ehsan M. Izadmehr, Isabella C. Espinel, Evelien H.S. Schut, Romy Wichmann

Cell Counting. Caitlin M. Vander Weele, Isabella C. Espinel, Cody A. Siciliano

Behavioral Experiments. Caitlin M. Vander Weele, Ehsan M. Izadmehr, Isabella C. Espinel, Evelien H.S. Schut

Behavioral Scoring – Marble Burying. Caitlin M. Vander Weele and Isabella C. Espinel

In Vivo Calcium-Imaging Recordings. Caitlin M. Vander Weele, Cody A. Siciliano, Edward H. Nieh

In Vivo Calcium-Imaging Analysis. Caitlin M. Vander Weele, Cody A. Siciliano, Edward H. Nieh, Praneeth Namburi. Eyal Y. Kimchi

Histology. Caitlin M. Vander Weele, Ehsan M. Izadmehr, Isabella C. Espinel, Nancy Padilla

Confocal Microscopy. Caitlin M. Vander Weele

Chapter 4

Dopamine enhances neuronal responses to aversive stimuli in periaqueductal gray-projecting prefrontal neurons and inhibits striatal-projecting neurons

Introduction

Thus far we have shown that mPFC-dPAG projectors are preferentially responsive to an aversive stimulus, and activation of this population drives defensive and avoidance behaviors. Given that mPFC-dPAG and mPFC-NAc neurons are non-overlapping and functionally distinct, we considered the possibility that increased dopaminergic tone might differentially impact these projection-defined populations of neurons. Controversy has long surrounded the topic of how dopamine alters the firing of mPFC neurons. Seemingly contradictory results from different groups performing whole-cell patch-clamp recordings from pyramidal neurons in Layer 5 of mPFC have reported dopamine-induced increases (Penit-Soria et al., 1987; Yang and Seamans, 1996) or decreases (Bunney and Aghajanian, 1976; Gulledge and Jaffe, 1998) in activity. One possible explanation is that these groups recorded from different populations of neurons, introduced by sampling bias, considering heterogeneous responses to dopamine for different cell types in mPFC have been demonstrated (Gee et al., 2012; Tritsch and Sabatini, 2012). Here we use *ex vivo* electrophysiological recordings of mPFC-dPAG and mPFC-NAc neurons combined with optogenetic activation of VTA dopamine terminals to explore how dopamine modulates the excitability of these two projector population.

Striatal-projecting mPFC neurons express D1 (~20%) and D2 (~60%) receptors, reported by *in situ* hybridization combined with retrograde labeling (Gaspar et al., 1995). Further, mPFC D1+ terminal axons are observed in the NAc in D1 transgenic reporter mouse lines (Han et al., 2017) and this pathway is modulated by dopamine release (Brady and

O'Donnell, 2004; Buchta et al., 2017). Dopamine receptor expression has not been explored in mPFC-dPAG neurons directly, although sparse downstream terminal fluorescence in D1 transgenic mice suggests that they do not express D1 (Han et al., 2017). As previously mentioned, considerable evidence supports indirect modulation of mPFC pyramidal neurons by dopamine — either via interactions with local GABAergic interneurons or modulation of other inputs (Paspalas and Goldman-Rakic, 2005; Seamans et al., 2001b; Tritsch and Sabatini, 2012). To explore this, we first characterize dopamine receptor localization on both projection-defined subpopulations and the impact of dopamine on mPFC-dPAG projectors *in vivo* using both calcium-imaging and electrophysiology combined with optogenetic phototagging.

Results

To test whether dopamine had different effects on the intrinsic excitability of these functionally-distinct populations, we performed whole-cell patch-clamp recordings in acute slice preparations of the mPFC containing ChR2-expressing VTA dopamine terminals and retrogradely-labeled mPFC-dPAG or mPFC-NAc neurons (**Figure 16a**). E*x vivo* recordings/reconstructions in labeled cells revealed several differences in the electrophysiological (**Figure 16b-i**) and morphological properties (**Figure 16j-l**).

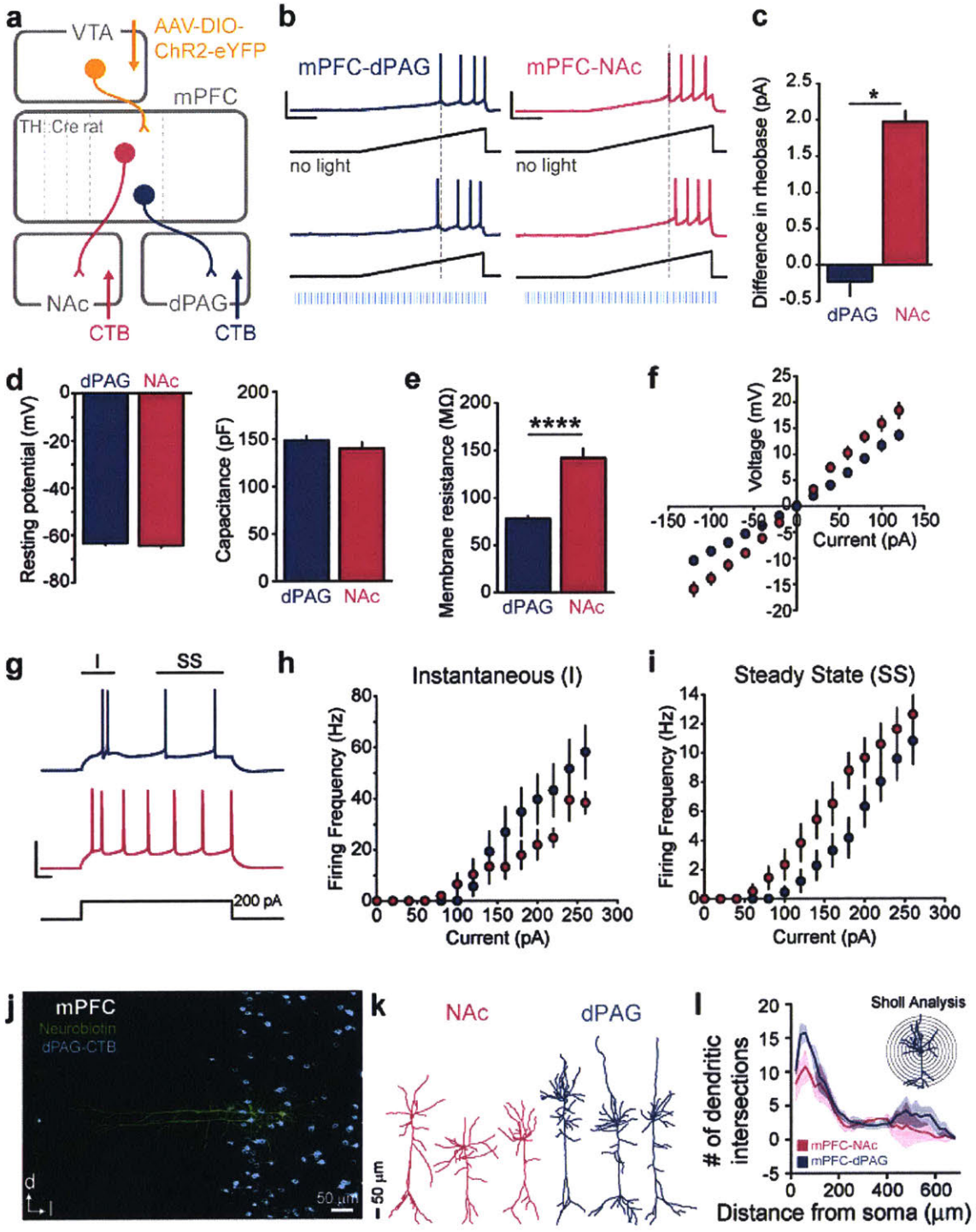
a
VTA
AAV-DIO-ChR2-eYFP
mPFC
TH::Cre rat
NAc
dPAG
CTB
CTB
b
mPFC-dPAG
mPFC-NAc
no light
no light
c
Difference in rheobase (pA)
dPAG
NAc
d
dPAG
NAc
Resting potential (mV)
Capacitance (pF)
dPAG
NAc
e
Membrane resistance (MΩ)
****
dPAG
NAc
f
Voltage (mV)
Current (pA)
g
I
SS
200 pA
h
Instantaneous (I)
Firing Frequency (Hz)
Current (pA)
i
Steady State (SS)
Firing Frequency (Hz)
Current (pA)
j
mPFC
Neurobiotin
dPAG-CTB
d
l
50 µm
k
NAc
dPAG
50 µm
l
Sholl Analysis
# of dendritic intersections
mPFC-NAc
mPFC-dPAG
Distance from soma (µm)

Figure 16. mPFC-dPAG and mPFC-NAc projectors have different electrophysiological properties.

(a) Schematic of viral strategy to optically manipulate ChR2-expressing VTA^{DA} terminals in the mPFC and record from dPAG- and NAc-projectors retrogradely labeled with cholera toxin (CTB) with *ex vivo* electrophysiology.

(b) Representative traces showing firing elicited in mPFC-dPAG and mPFC-NAc neurons in response to current ramp with and without VTA^{DA} terminal stimulation (grey dashed line indicates time of first action potential without optical stimulation).

(c) Optical stimulation of VTA^{DA} terminals increased the current required to elicit an action potential (rheobase) in NAc-projectors and the change in rheobase with optical stimulation (ON-OFF) was different between dPAG- and NAc-projectors (unpaired t-test, $t(12) = 2.669$, $p = 0.0205$).

(d) Electrophysiological properties of mPFC-dPAG and mPFC-NAc neurons. Neither resting membrane potential (unpaired t-test, $t(27) = 0.6265$, $p = 0.5363$), nor capacitance (unpaired t-test, $t(75) = 0.8643$, $p = 0.3902$) were different between dPAG- and NAc-projectors.

(e) The membrane resistance was significantly greater in NAc-projectors (unpaired t-test, $t(75) = 7.030$, $p < 0.0001$).

(f) The current-voltage (I-V) relationship of mPFC-dPAG and mPFC-NAc neurons obtained by applying a series of current steps in voltage-clamp mode (two-way ANOVA, $F_{12,324} = 10.16$, $p < 0.0001$).

(g) Representative traces showing action potential firing in mPFC-dPAG and mPFC-NAc neurons in response to a depolarizing current step.

(h-i) Instantaneous (I) and steady state (SS) firing frequency in dPAG- and NAc-projectors in response to increasing current steps.

(j) Representative confocal image of mPFC-dPAG labeled neurons filled with neurobiotin for reconstruction.

(k) Representative examples of reconstructed mPFC-NAc and mPFC-PAG neurons.

(l) Sholl analysis of mPFC subpopulations.

Error bars indicate ±SEM.

We presented current steps to evoke moderate levels of firing and paired these current steps with photostimulation of VTA^{DA}-mPFC terminals on interleaved sweeps (**Figure 17a-c**). Photostimulation of VTA^{DA}-mPFC terminals reduced the number of spikes per step for mPFC-NAc neurons, but did not alter the intrinsic excitability of mPFC-dPAG neurons (**Figure 17c-e**). Given that dopamine suppressed firing of mPFC-NAc neurons, we hypothesized that this could be mediated by D2 receptors. To test this, we repeated this experiment in the presence of the D2 receptor antagonist, raclopride, and found that VTA^{DA}-mPFC photostimulation-induced suppression was attenuated.

VTA dopamine neurons projecting to the striatum co-release fast amino acid neurotransmitters, such as GABA (Tritsch et al., 2016) and glutamate (Stuber et al., 2010). A proportion of mesocortical dopamine neurons co-stain for VGluT2 (Gorelova et al., 2012) suggesting glutamate co-release within this pathway. Indeed, a recent study has reported co-release of glutamate from mesocortical dopamine neurons during phasic (50 Hz for 500 ms) but not tonic (5 Hz) stimulation in Layer 6 mPFC neurons (Ellwood et al., 2017). Importantly, both stimulation parameters enhanced dopamine release measured by microdialysis combined with HPLC, although phasic stimulation evoked significantly great dopamine release (phasic = 34.1% increase versus tonic = 17.1% increase; Ellwood et al., 2017). In Layer 5 mPFC-NAc and mPFC-dPAG, we observed no evidence of co-release from dopamine axon terminals (**Figure 17f**).

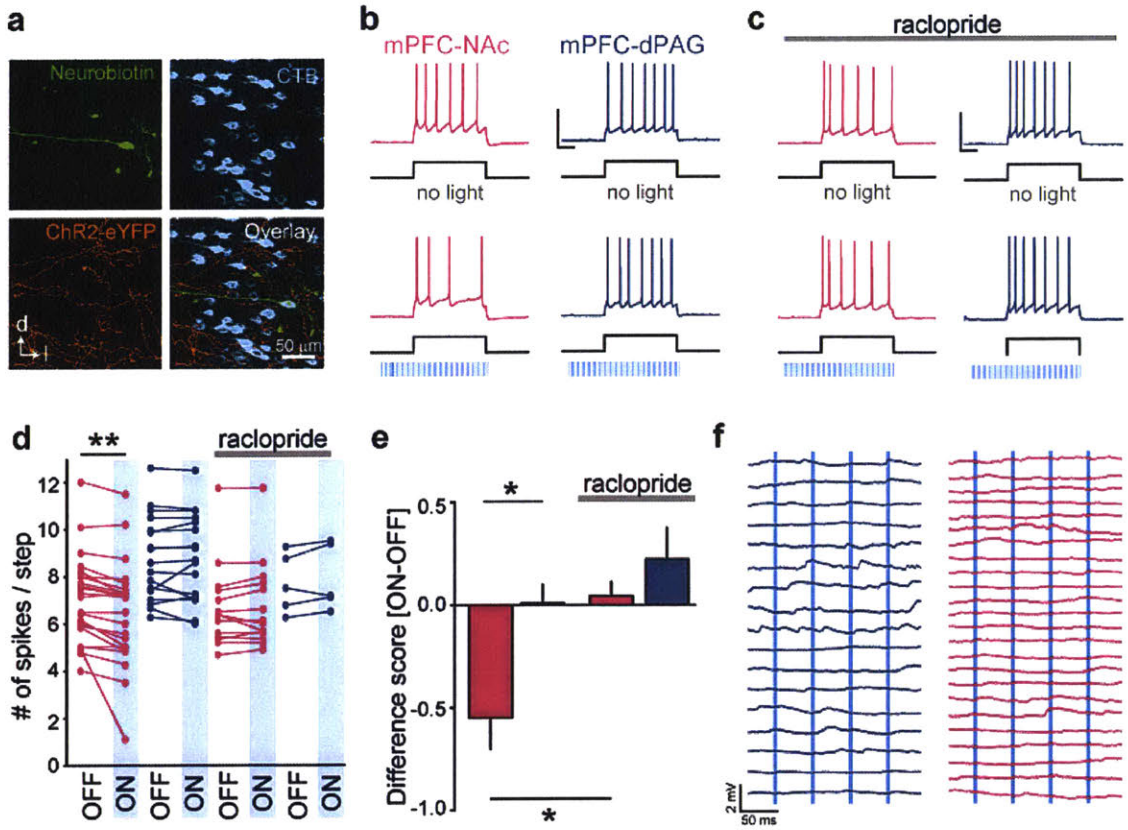

Figure 17. Dopamine inhibits NAc-projectors via D2-receptors.

(a) Representative images of a recorded mPFC-dPAG neuron (neurobiotin+ and CTB+) surrounded by ChR2-eYFP+ VTA^{DA} terminals.

(b) Representative traces of current-clamp recordings from a mPFC-NAc and mPFC-dPAG neuron during a current step without (top) and with (bottom) optogenetic activation of VTA^{DA} terminals (470 nm, 20 Hz, 60 pulses, 5 ms pulse-durations).

(c) Representative traces of a mPFC-dPAG and mPFC-NAc neuron during a current step without (top) and with (bottom) optogenetic activation of VTA^{DA} terminals in the presence of D2-type dopamine receptor blockade via bath applied raclopride.

(d) Optical activation of VTA^{DA} terminals did not influence the number of spikes per step in mPFC-dPAG neurons but decreased the number of spikes per step in mPFC-NAc neurons, an effect not observed with D2-receptor antagonism (two-way repeated measures ANOVA, $F_{3,56} = 5.531$, $p = 0.0027$, Bonferroni multiple comparisons tests, mPFC-NAc OFF vs. ON, $p < 0.001$).

(e) The change in spike number with optical stimulation (ON-OFF) was different between mPFC-dPAG and mPFC-NAc neurons and was blocked by D2-receptor antagonism (one-way ANOVA, $F_{3,56} = 5.343$, $p = 0.0026$, Bonferroni multiple comparisons tests $p < 0.05$.

(f) No evidence of co-release of fast-synaptic neurotransmitters (i.e., glutamate and GABA) from VTA^{DA} terminals onto either mPFC-dPAG (teal) or mPFC-NAc (pink) populations.

Error bars indicate ±SEM**.** Scale bars (histology) = 50 μm. Scale bars (electrophysiology) = 500 ms. 50 mV.

These data suggested that dopamine acts directly on mPFC-NAc neurons to inhibit them via a D2 receptor-dependent mechanism, and that mPFC-dPAG neurons do not express dopamine receptors. To explore dopamine receptor localization on mPFC-NAc and mPFC-dPAG neurons, we performed retrograde-labeling of projectors in Drd1a-Cre and Drd2-Cre mice injected with Cre-dependently expressed eYFP (**Figure 18a**). Consistent with previous studies, we found that mPFC-NAc projectors express both D1 (31.5%) and D2 (86.3%) receptors (Gaspar et al., 1995; Vincent et al., 1993, 1995), whereas mPFC-dPAG projectors largely lack both D1 (5%) and D2 (21.6%) receptors (D1 chi square, $X^2 = 93.29$, $p < 0.0001$; D2 chi square, $X^2 = 345.6$, $p < 0.0001$) (**Figure 18b-f**).

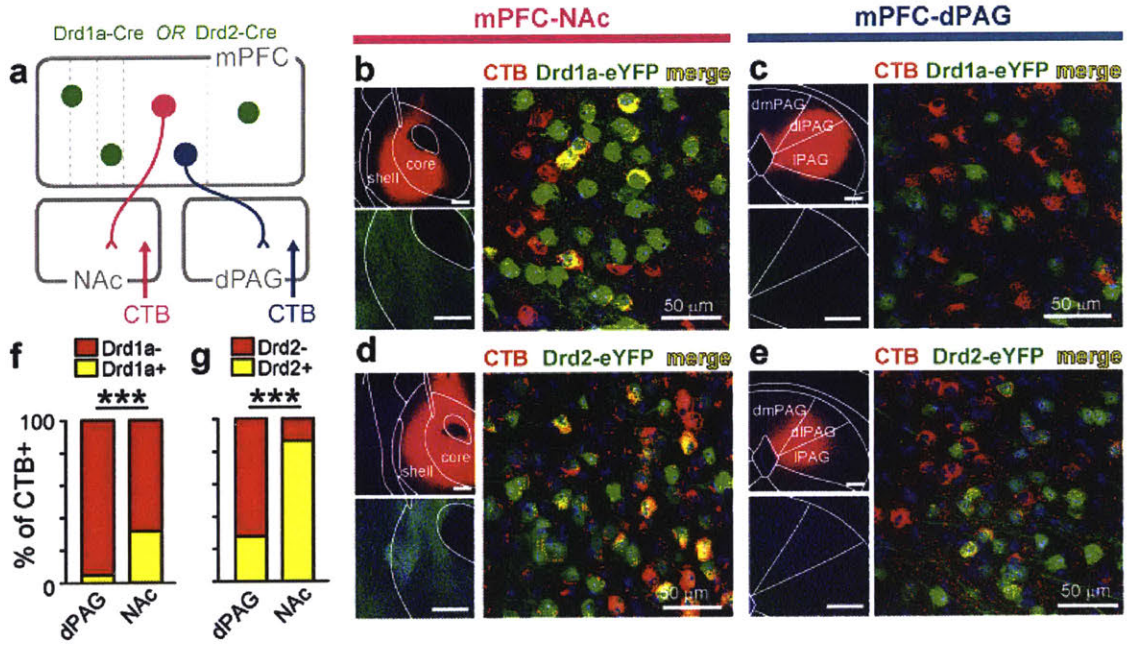

Figure 18. mPFC-dPAG projectors largely do not express dopamine receptors.

(a) Schematic of strategy for identifying dopamine receptor type 1 (D1) and dopamine receptor type 2 (D2) on mPFC-projector populations using transgenic mice (Drd1a-Cre [n = 3] and Drd2-Cre [n = 3]), retrograde labeling, and Cre-dependent eYFP recombination.

(b) Representative confocal images of CTB injections sites (upper left), mPFC terminal fluorescence (lower left), and mPFC cell bodies (right) in Drd1a-Cre::eYFP in NAc CTB injected subjects.

(c) Representative confocal images of CTB injections sites (upper left), mPFC terminal fluorescence (lower left), and mPFC cell bodies (right) in Drd1a-Cre::eYFP in dPAG CTB injected subjects.

(d) Representative confocal images of Drd2-Cre::eYFP subjects injected with CTB in the NAc.

(e) Representative confocal images of Drd2-Cre::eYFP subjects injected with CTB in the dPAG.

(f) 5% of mPFC-dPAG CTB+ were also Drd1a+ (19/378), whereas 31.5% of mPFC-NAC CTB+ neurons were co-labeled as Drd1a+ (151/479) (D1 chi square, $X^2 = 93.29$, $p < 0.0001$).

(g) 27.6% of mPFC-dPAG CTB+ neuron were also Drd2+ (74/342), whereas 86.3% of mPFC-NAc CTB+ neurons were co-labeled as Drd2+ (414/480) (D2 chi square, $X^2 = 345.6$, $p < 0.0001$).

Error bars indicate ±SEM. Scale bars (histology) = 50 μm.

The observation that dopamine attenuates mPFC-NAc neurons *ex vivo*, is consistent with previously reported *in vivo* recordings, which show attenuated responses via a D2-dependent mechanism within this circuit (Brady and O'Donnell, 2004). Since dopamine did not modulate mPFC-dPAG neurons in *ex vivo* recordings and this population does not robustly express dopamine receptors, this left multiple interpretations. One possibility was that dopamine does not alter the activity or function of mPFC-dPAG neurons. Another possibility is that dopamine modulates the signal-to-noise for incoming sensory information, a function that may only be revealed *in vivo* when connections carrying such information are intact. Indeed, this notion is supported by anatomical data showing that D1-receptors are located on axon terminals that form asymmetric (i.e., glutamatergic) synapses onto mPFC neurons (Paspalas and Goldman-Rakic, 2005).

To explore this idea, we first used a novel technology allowing for simultaneous recording of calcium events in mPFC-dPAG neurons while stimulating VTA dopamine terminals *in vivo* in freely-moving mice. GGaMP6m was targeted to mPFC-dPAG neurons in mice as previously described, and neurons expressing the DA transporter (DAT) were transduced with the excitatory red-shifted opsin, ChrimsonR (AAV-FLEX-ChrimsonR-tdTomato (Klapoetke et al., 2014) or mCherry as a control (**Figure 19a** and **Figure 20a-b)**. In order to use two Cre-dependent systems within the same animal, it is essential these pathways remain distinct. Indeed, neither dopaminergic nor non-dopaminergic neurons in the VTA project to the dPAG (**Figure 18b-c**), eliminating the possibility that retrogradely transported CAV2-Cre injected into the dPAG permits viral recombination in the non-dopaminergic neurons in the VTA.

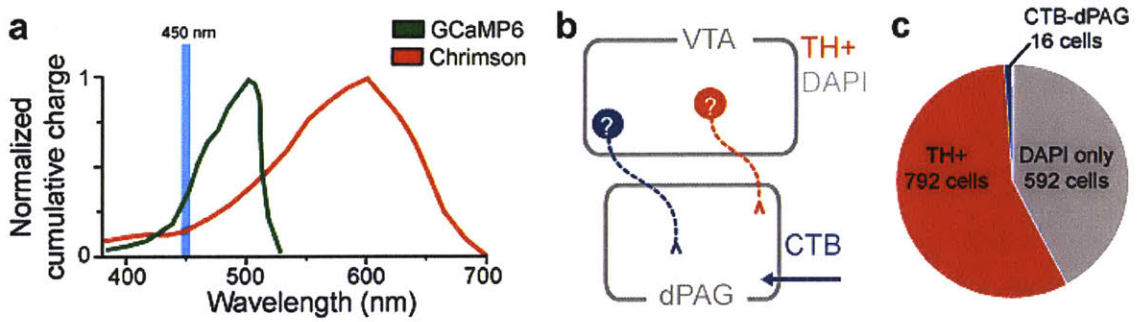

Figure 19. Investigation of VTA projections to the dPAG for simultaneous epifluorescent imaging in mPFC-dPAG neurons and excitation of VTA^{DA} terminals.

(a) Action spectra for Chrimson (adapted from Klapoetke et al., 2014) and GCaMP (adapted from Shigetomi et al., 2016 and Chen et al., 2013). GCaMP6m was excited with a 450 nm LED.

(b) To verify that VTA neurons do not project to the dPAG (to allow for CAV-Cre mediated GCaMP6m expression in dPAG neurons and simultaneous expression of the excitatory opsin ChrimsonR in VTA^{DA} neurons) VTA slices were immunostained for tyrosine hydroxylase (TH) in rats injected with the retrograde tracer CTB in the dPAG.

(c) Of 1,400 DAPI+ cells counted in the VTA, 792 (56%) were TH+, 16 (1.1%) were CTB+, and 0 were TH+ and CTB+. The lack of CTB+ cells suggests that VTA does not make a prominent projection to the dPAG. Of the retrogradely labeled cells observed in the VTA, none were TH+.

In a novel homecage, VTA dopaminergic terminals in the mPFC were activated (20 Hz, 60 pulses, every 30 s) during a 10 min ON epoch, flanked by two OFF epochs, where no stimulation occurred (**Figure 20c**). Examination of transient calcium events from individual mPFC-dPAG neuron traces (**Figure 20d**) revealed that while VTA DA stimulation decreased the average calcium event frequency, it simultaneously increased the average amplitude (**Figure 20e-f**), consistent with our model that dopamine increases the signal-to-noise ratio in mPFC-dPAG.

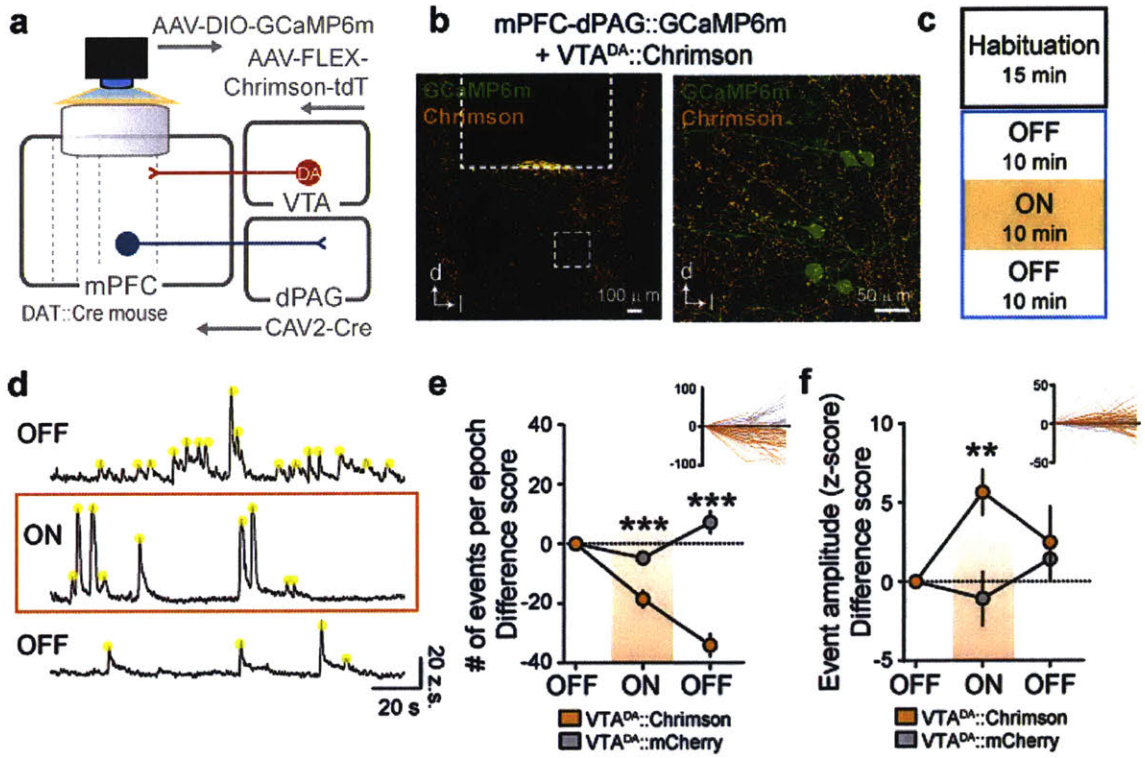

Figure 20. Stimulation of dopamine terminals in the mPFC increase calcium transient amplitude and decreases frequency in dPAG-projectors.

(a) Schematic of strategy to simultaneously image fluorescent calcium activity in mPFC-dPAG::GCaMP6m neurons and activate VTA^{DA} terminals in awake and freely moving mice.

(b) VTA^{DA} neurons expressed ChrimsonR (n = 4 mice, 44 ROIs) or mCherry (control, n = 5 mice, 50 ROIs), in a Cre-dependent manner in DAT::Cre mice. In the same animal, dPAG-projectors in the mPFC expressed GCaMP6m using a dual viral strategy.

(c) Schematic of experimental design. After a 15 min habituation period, each recording session (30 min total, 450 nm fluorescence emission, 10 Hz) was divided into 3 epochs: OFF-ON-OFF. During the ON epoch, fluorescence emission was recorded while a 620 nm LED stimulated ChrimsonR expressing VTA^{DA} terminals (20 Hz, 60 p, 5 ms pulses, every 30 s).

(d) Representative traces from a mPFC-dPAG::GCaMP6m neuron during each 10 min OFF-ON-OFF recording epoch. Calcium transients (yellow dots) for each neuron were identified and quantified.

(e) VTA^{DA} terminal stimulation decreased the average calcium event frequency per neuron, during both the ON and second OFF epochs (data normalized to first OFF epoch; two-way repeated measure ANOVA, $F_{2,184} = 43.62$, $p < 0.0001$, Bonferroni multiple comparisons tests, $p < 0.05$).

(f) VTA^{DA} terminal stimulation increased the average calcium event amplitude per cell during the ON epoch, an effect that recovered in the second OFF epoch (data normalized to first OFF epoch; two-way repeated measure ANOVA, $F_{2,184} = 3.50$, $p = 0.0322$, Bonferroni multiple comparisons tests, $p < 0.05$).

Error bars indicate ±SEM.

However, the interpretation of our calcium imaging results alone is limited by several caveats. First, while calcium transients are monotonically-related to action potentials, this relationship may be non-linear under some conditions (Chen et al., 2013). Second, dopamine could alter intracellular calcium handling (Gee et al., 2012; Surmeier et al., 1995). To demonstrate an alteration of the signal-to-noise ratio, we must first presume to know what the "signal" is and what constitutes "noise." Based on our single-cell mPFC-dPAG imaging data, we observed that mPFC-dPAG neurons were preferentially excited to shock, relative to sucrose, which led us to hypothesize that the signal represented aversive stimuli.

To test this hypothesis, we used ChR2-assisted identification of mPFC-dPAG projectors during electrophysiological recordings, paired with optical manipulations of local dopamine terminals from the VTA. In a DAT::Cre mouse, we expressed ChrimsonR in VTA dopamine neurons, expressed ChR2 in mPFC-dPAG neurons. Considering recurrent excitation is a well-established phenomenon in the mPFC (Gao et al., 2001) we used *ex vivo* electrophysiological recordings in ChR2-eYFP expressing cells and non-expressing neighbors to determine their photoresponse latencies to 5 ms pulses of blue light (**Figure 21a-c**) (Beyeler et al., 2016). All ChR2-eYFP expressing fired and action potential (AP) following photostimulation (i.e., suprathreshold response) with fast latencies, < 5 ms. In contrast, non-expressing neighbors had diverse responses to 5 ms blue light: 4 showed no response, 4 were characterized by a subthreshold response, while none had a suprathreshold response (**Figure 21d-f**). Based on these data, the *in vivo* photoresponse latency threshold was set at <10 ms for mPFC-dPAG::ChR2 projectors.

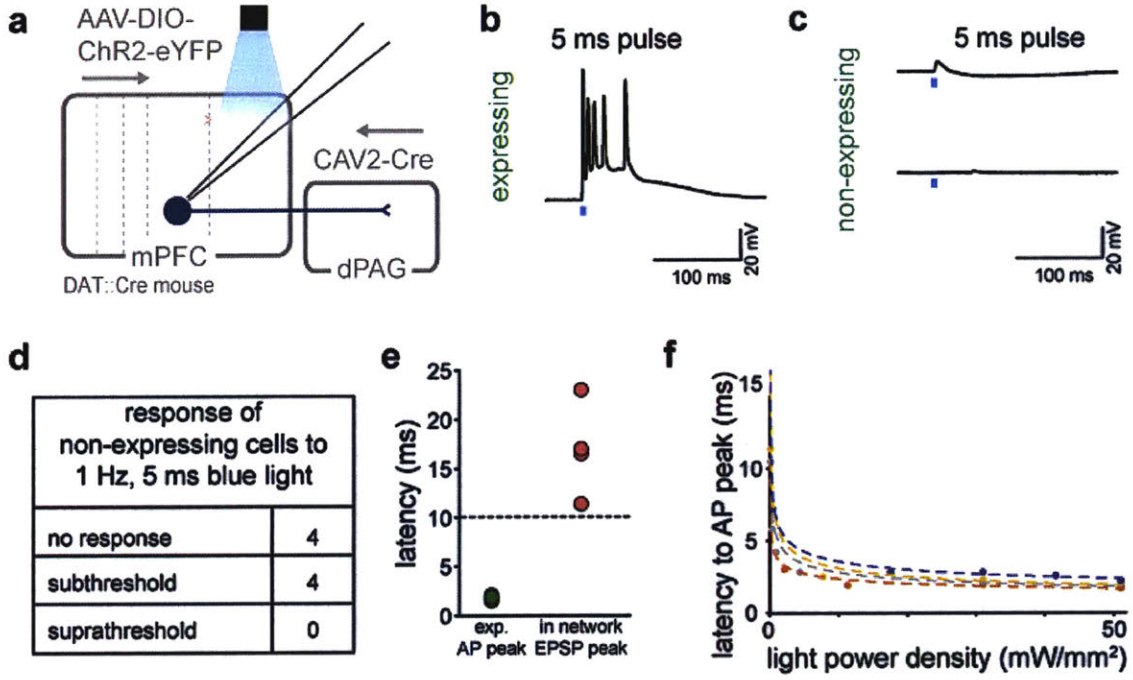

Figure 21. *Ex vivo* latency validation for head-fixed electrophysiological recordings with phototagging.

(a) Schematic of viral strategy to optically manipulate ChR2-expressing VTA^{DA} terminals in the mPFC and record from mPFC-dPAG::ChR2 and non-expressing neighboring neurons with *ex vivo* electrophysiology.

(b) Representative traces from ChR2-expressing cells showing action potential (AP) firing in response to a 5 ms blue light pulse.

(c) Representative traces from non-expressing 'in network' cells to delivery of 5 ms blue light.

(d) Number of non-expressing cells with different responses to 1 Hz, 5 ms blue light delivery.

(e) Latency to AP peak for ChR2-expressing cells (n = 5) and latency to EPSP peak for non-expressing neighbors (n = 4) measured from the onset of a 51.04 mW/mm^2 5 ms blue light

pulse delivered at 1 Hz. **(f)** Latency to AP peak for ChR2-expressing cells plotted against light power density.

Using the same viral strategy, mice for *in vivo* recordings were headfixed and implanted with a drivable, acute optrode in the mPFC (**Figure 22a-b**). Again, dopaminergic terminals from the VTA were stimulated in the mPFC during a 10 min ON epoch flanked by two OFF epochs where no stimulation occurred, in a head-fixed set-up (Beyeler et al., 2016). While recording, unpredicted sucrose and airpuff presentations were interleaved to assess the effect of dopamine on stimulus-evoked neural responses (**Figure 22c**). Sucrose and airpuff deliveries were terminated at the end of the 30 min recording period and mPFC-dPAG::ChR2 were optically tagged with blue light (**Figure 22d-g**). Importantly, photoidentified ChR2-expressing neurons were not activated by 593 nm red-shifted light used for VTA^{DA}::Chrimson terminal activation (**Figure 22h**). Of the 204 total mPFC units recorded, 32 were phototagged (**Figure 22i**) using *ex vivo* verified response latencies to blue light (**Figure 21**). Consistent with our *in vivo* calcium imaging results, we found that 43.8% of phototagged mPFC-dPAG neurons were excited to airpuff, while none of the units were selectively sucrose responsive (**Figure 22j-k**). In comparison to mPFC-dPAG neurons, our unidentified population was less responsive to airpuff and more responsive to sucrose (**Figure 22l**).

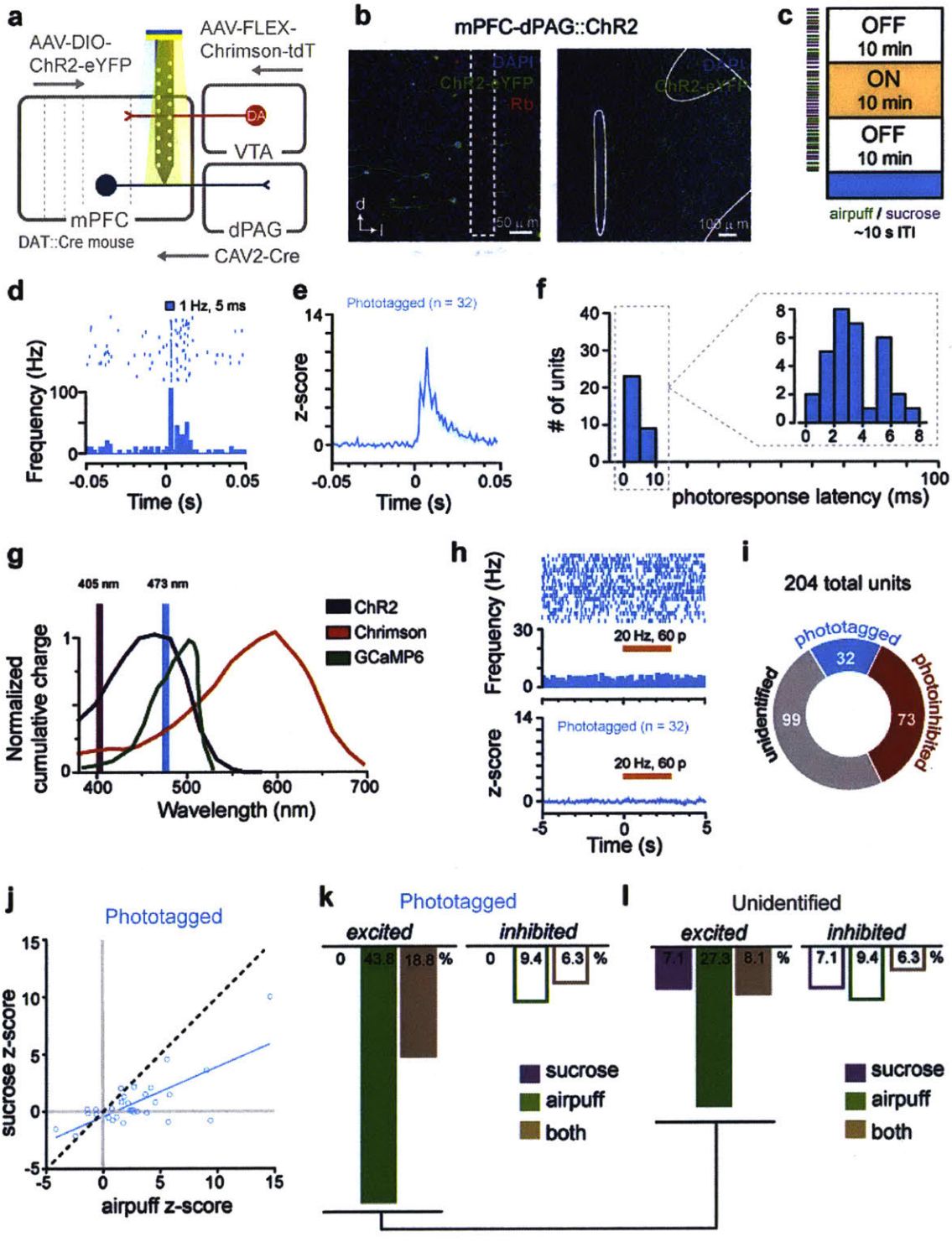
a
AAV-DIO-
ChR2-eYFP
AAV-FLEX-
Chrimson-tdT
VTA
mPFC
dPAG
DAT::Cre mouse
CAV2-Cre
b
mPFC-dPAG::ChR2
DAPI
ChR2-eYFP
Rb
c
OFF
10 min
ON
10 min
OFF
10 min
airpuff / sucrose
~10 s ITI
d
1 Hz, 5 ms
Frequency (Hz)
Time (s)
e
Phototagged (n = 32)
z-score
Time (s)
f
# of units
photoresponse latency (ms)
g
405 nm
473 nm
ChR2
Chrimson
GCaMP6
Normalized cumulative charge
Wavelength (nm)
h
Frequency (Hz)
20 Hz, 60 p
Phototagged (n = 32)
z-score
Time (s)
i
204 total units
phototagged
32
photoinhibited
73
unidentified
99
j
Phototagged
sucrose z-score
airpuff z-score
k
Phototagged
excited
inhibited
0
43.8
18.8
%
0
9.4
6.3
%
sucrose
airpuff
both
l
Unidentified
excited
inhibited
7.1
27.3
8.1
%
7.1
9.4
6.3
%
sucrose
airpuff
both

Figure 22. mPFC-dPAG neurons are excited to airpuff.

(a) Schematic of strategy to manipulate VTA^{DA} terminals in the mPFC and optically identify mPFC-dPAG::ChR2 neurons using *in vivo* head-fixed electrophysiology.

(b) Representative image of recording track in the mPFC (Rb, red retrobeads) and ChR2-eYFP-expressing mPFC-dPAG neurons. Representative image of ChR2-eYFP-expressing terminals surrounding the PAG.

(c) Schematic of recording blocks. After a 5 min rest period following optrode placement, each recording session (~35 min total, 30 min test session + ~5 min phototagging session) was divided into 3 epochs: OFF-ON-OFF. During the ON epoch, 593 nm laser light from the optrode stimulated ChrimsonR expressing VTA^{DA} terminals (20 Hz, 60 pulses, 5 ms pulse-duration, every 30 s, ≤ 4 mW). Neural activity was recorded while mice received random deliveries of sucrose (purple) or airpuff (green) throughout the 30 min recording block. Following completion of the final OFF epoch, stimuli delivery were terminated and 473 or 405 nm lasers were connected to the optrode for phototagging (1 Hz, 5ms pulses; 1 sec pulses; and 100 ms pulses, ≤ 20 mW).

(d) Peri-stimulus time histogram (PSTH) of the firing rate in response to the onset of 1 Hz, 5 ms pulse of 473 nm laser light used for phototagging from a representative unit.

(e) Population z-score of all phototagged units aligned to 1 Hz, 5 ms pulse of 473 nm.

(f) Photoresponse latencies showing < 8 ms response latency from all 32 mPFC-dPAG::ChR2 units.

(g) Action spectra for Chrimson, ChR2 (adapted from Klapoetke et al., 2014), and GCaMP (adapted from Shigetomi et al., 2016 and Chen et al., 2013) Phototagging was achieved with blue laser light.

(h) PSTH from representative phototagged unit (top) and population z-score (bottom) showing no response to 20 Hz, 60 pulses of 593 nm laser light used for VTA^{DA}::Chrimson terminal activation.

(i) 204 mPFC units were recorded (n = 3 mice, 5 recording sessions) and 32 phototagged units were identified as mPFC-dPAG projectors (blue), 78 were photoinhibited (red), and 99 remained unidentified (black).

(j) Neural response magnitudes to airpuff (x-axis) and sucrose (y-axis) in phototagged (blue) populations.

(k) Percent of units responding ($p > 0.01$) to sucrose (purple), airpuff (green), or both (brown) in the phototagged (n = 32) population. Excitatory response are shown in closed bars and inhibitory responses in open bars.

(l) Percent of units responding ($p > 0.01$) to sucrose (purple), airpuff (green), or both (brown) in the unidentified (n = 99) population. Excitatory responses are shown in closed bars and inhibitory responses in open bars. Excitatory response patterns were different between phototagged and unidentified populations (chi square, $X^2 = 9.52$, $p = 0.0016$).

Error bars indicate ±SEM.

The robust effect of dopamine on airpuff, but not sucrose, responses in mPFC-dPAG neurons was striking, as exemplified by time-locked responses to these stimuli (**Figure 23a**). Although the dopamine-induced stimulus-evoked and basal firing rate changes were quite heterogeneous, the increase in signal-to-noise was not (**Figure 23a**). As a population, dopamine terminal stimulation did not change basal firing rates in phototagged or unidentified populations (**Figure 24a-b**). Remarkably, dopamine selectively enhanced neural responses to airpuff, but did not influence responses to sucrose in mPFC-dPAG neurons. Further, the signal-to-noise increase was not observed in the unidentified population (**Figure 24c-h**) or photoinhibited populations (**Figure 25**).

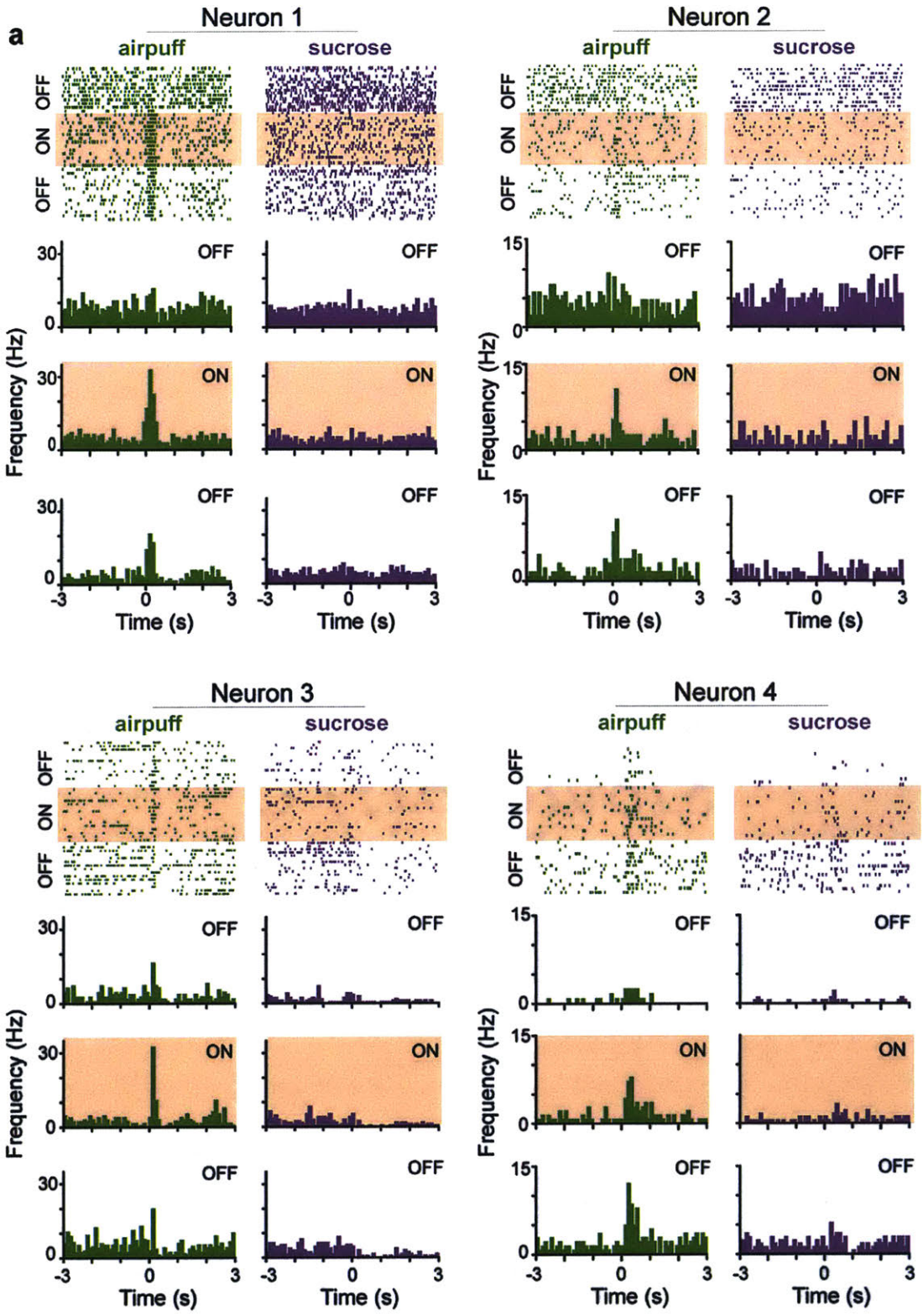
a
Neuron 1
airpuff
sucrose
OFF
ON
OFF
Frequency (Hz)
30
0
OFF
ON
OFF
-3
0
3
Time (s)
Neuron 2
15
Neuron 3
Neuron 4

Figure 23. Representative mPFC-dPAG units.

(a) Representative PSTHs of 4 photoidentified mPFC-dPAG units aligned to airpuff (green) and sucrose (purple). Histograms show neural responses in the OFF-ON-OFF epochs.

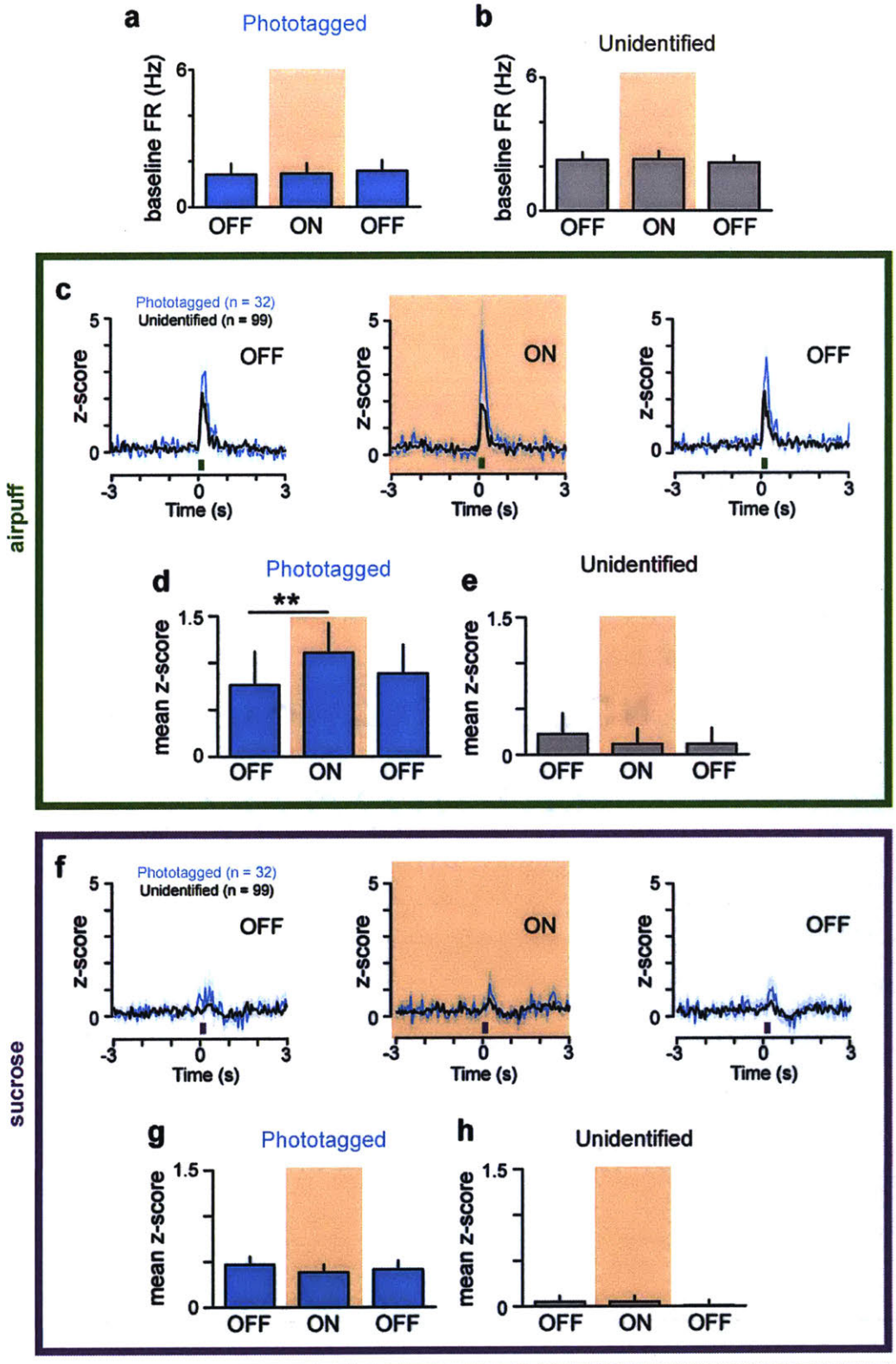
a
Phototagged
baseline FR (Hz)
6
0
OFF
ON
OFF
b
Unidentified
baseline FR (Hz)
6
0
OFF
ON
OFF
airpuff
c
Phototagged (n = 32)
Unidentified (n = 99)
z-score
5
0
OFF
ON
OFF
-3
0
3
Time (s)
d
Phototagged
**
mean z-score
1.5
0
OFF
ON
OFF
e
Unidentified
mean z-score
1.5
0
OFF
ON
OFF
sucrose
f
Phototagged (n = 32)
Unidentified (n = 99)
z-score
5
0
OFF
ON
OFF
-3
0
3
Time (s)
g
Phototagged
mean z-score
1.5
0
OFF
ON
OFF
h
Unidentified
mean z-score
1.5
0
OFF
ON
OFF

Figure 24. Dopamine selectively enhances mPFC-dPAG responses to airpuff.

(a) VTA dopamine terminal stimulation in the mPFC did not change the baseline firing rate (FR, Hz) in the 3 s pre-stimulus windows in the phototagged population(Friedman Test, $X^2(2) = 2.472$ $p = 0.2905$).

(b) VTA dopamine terminal stimulation in the mPFC did not change the baseline firing rate (FR, Hz) in the 3 s pre-stimulus windows in the unidentified (Friedman Test, $X^2(2) = 0.4242$ $p = 0.8089$) population.

(c) Population z-score for phototagged (blue) and unidentified (black) units aligned to airpuff across the OFF-ON-OFF epochs.

(d) VTA^{DA} terminal stimulation enhanced airpuff responses in phototagged units during the ON epoch, (Friedman Test, $X^2(2) = 9.813$, $p = 0.0075$, Dunn's multiple comparisons tests, $p < 0.01$).

(e) VTA^{DA} terminal stimulation did not change responses to airpuff in unidentified neurons (Friedman Test, $X^2(2) = 0.0625$ $p = 0.9692$).

(f) Population z-score for phototagged (blue) and unidentified (black) units aligned to sucrose delivery across the OFF-ON-OFF epochs.

(g) VTA^{DA} terminal stimulation did not change responses to sucrose in phototagged neurons (Friedman Test, $X^2(2) = 3.960$, $p = 0.1381$).

(h) VTA^{DA} terminal stimulation did not change responses to sucrose in unidentified neurons (Friedman Test, $X^2(2) = 0.1818$, $p = 0.9131$).

Error bars indicate ±SEM.

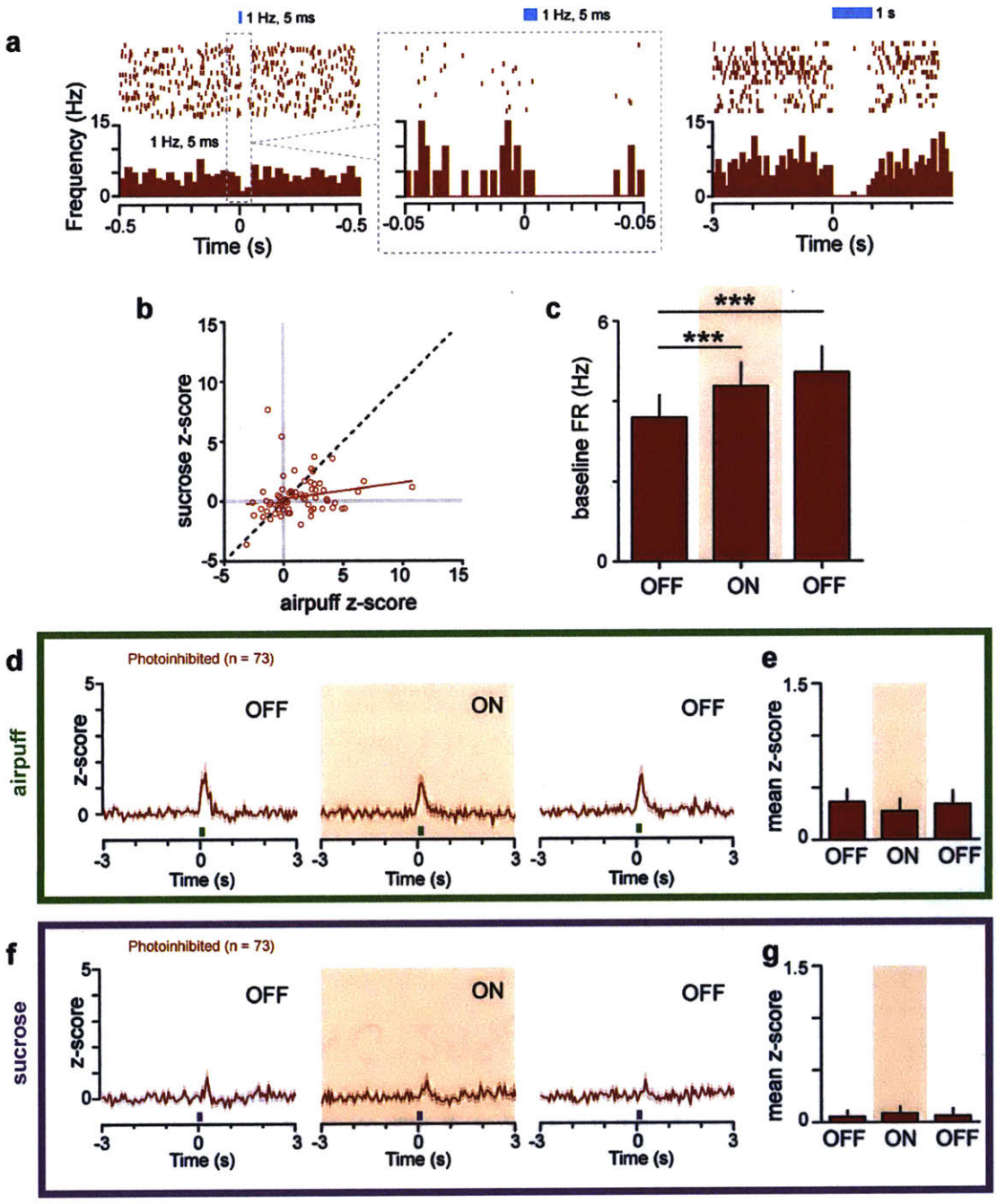

Figure 25. Dopamine increase baseline firing rate, but not stimulus-evoked responses in photoinhibited mPFC neurons.

(a) 35.8% of recorded units (73/204) were photoinhibited. Representative PSTHs of a photoinhibited unit in response to 1 Hz, 5 ms (left) and 1 s (right) of 473 nm light.

(b) Neural response magnitudes to airpuff (x-axis) and sucrose (y-axis) in photoinhibited (red) population.

(c) VTA dopamine terminal stimulation in the mPFC increased the baseline firing rate (FR, Hz) in the 3 s pre-stimulus windows in the photoinhibited population during the ON and second OFF epochs (Friedman Test, $X^2(2) = 16.22$; $p = 0.0003$; Dunn's multiple comparisons tests, $p > 0.05$).

(d) Population z-score of photoinhibited units aligned to airpuff in each of the recording epochs.

(e) In photoinhibited neurons, VTA^{DA} terminal stimulation did not change neural responses to airpuff (Friedman Test, $X^2(2) = 2.493$, $p = 0.2875$, Dunn's multiple comparisons tests, $p > 0.05$).

(f) Population z-score of photoinhibited units aligned to sucrose in each of the recording epochs.

(g) In photoinhibited neurons, VTA^{DA} terminal stimulation did not affect neural responses to sucrose (Friedman Test, $X^2(2) = 0.4492$, $p = 0.7988$, Dunn's multiple comparisons tests, $p > 0.05$).

Error bars indicate ±SEM.

Experimental Procedures

General virus surgery.

Specific subject/surgery details for each experiment are detailed below. For all subjects, surgeries were performed under aseptic conditions and body temperature was maintained with a heating pad. Rodents were anesthetized with isoflurane mixed with oxygen (5% for induction, 2.5-2% for maintenance, 1L/min oxygen flow rate) and placed in a digital small animal stereotax (David Kopf Instruments, Tujunga, CA, USA). Following initial induction, hair was removed from the dorsal surface of the head with hair clippers, ophthalmic ointment was applied to the eyes, the incision area was scrubbed with alcohol pads and betadine (x3 each), and 2% lidocaine was injected just under the skin surface above the skull for topical anesthesia. All measurements were made relative to bregma (unless noted otherwise) for virus/implant surgeries. Viral injections were performed using a beveled microinjection needle (26 gauge for rat; 33 gauge for mice) with a 10 µL microsyringe (Nanofil; WPI, Sarasota FL, USA) delivering virus at a rate of 0.05-0.01 µL/min using a microsyringe pump (UMP3; WPI, Sarasota, FL, USA) and controller (Micro4; WPI, Sarasota, FL, USA). For injections at multiple locations on the dorsal-ventral axis, the most ventral location was completed first and the injection needle was immediately relocated to the more dorsal location and initiated. After injection completion, 15 mins were allowed to pass before the needle was slowly withdrawn. After viral infusions were completed, craniotomies were filled with bone wax and the incision closed with nylon sutures. Subjects were maintained under a heat lamp and provided 0.05 mg/kg (rat) / 0.10 mg/kg (mouse) buprenophine (s.c., diluted in warm Ringers solution) until fully recovered from anesthesia.

All experiments involving the use of animals were in accordance with NIH guidelines and approved by the MIT Institutional Animal Care and Use Committee. For all experiments involving viral or tracer injections, animals containing mistargeted injection(s) were excluded

after histological verification. Sample size was based on reports in related literature and were not predetermined by calculation.

Viral constructs

Recombinant AAV_5 vectors carrying ChR2 or fluorescent proteins (mCherry or eYFP) were packaged by the University of North Carolina Vector Core (Chapel Hill, NC, USA). AAV_8-hSyn-FLEX-ChrimsonR-tdTomato and AAV_5-hSyn-mCherry was packaged by the University of North Carolina Vector Core (Chapel Hill, NC, USA). Viruses carrying GCaMP6m were packaged by the University of Pennsylvania Vector Core (Philadelphia, PA, USA). Canine adeno-associated virus carrying Cre recombinase (CAV2-Cre 4.2x10 infectious units/mL) was packaged and obtained from the Istitut de Génétique Moléculaire de Montpellier, France from Dr. Eric Kremer.

***Ex vivo* electrophysiology to examine dopamine effects on projector populations.**

Subjects.

Male and female heterozygous BAC transgenic TH::Cre rats (~220 g; Charles Rivers Laboratories) were dual housed on a normal 12h:12h light/dark cycle (lights on at 09:00 AM) throughout the duration of experiments. Sample sizes was based on reports in related literature and were not predetermined by calculation.

Surgery.

Rats first received bilateral infusions of AAV_5-EF1a-DIO-ChR2-eYFP, as previously described (*Chapter 2 – Experimental Procedures – Fast-Scan Cyclic Voltammetry - Surgeries*). Rats were allowed to recover for virus surgery for an 8-10 weeks incubation period to ensure Cre-specific viral transduction of ChR2 in VTA^{DA} neurons and protein transport to distal terminals in the mPFC. After incubation, rats received a second surgery to retrogradely label

dPAG and NAc shell projectors in the mPFC. CTB injections were performed similarly as previously described (*Chapter 3 – Experimental Procedures - Retrograde cholera toxin-B tracing - Rats*). Briefly, rats received bilateral injections of CTB conjugated to Alexa Fluor-488 or -555 (Molecular Probes, Eugene, OR, USA) into the dPAG (AP: -6.6, ML: -0.6; DV: -5.4 mm), the NAc (AP: +1.5, ML: +0.95, DV: -7.5 mm), or one in each hemisphere (fluorophores were counterbalanced between rats).

Brain slice preparation.

7 days following CTB injections, TH::Cre rats were deeply anesthetized with sodium pentobarbital (250 mg/kg; IP) and transcardially perfused with 60 mL ice cold modified artificial cerebrospinal fluid (aCSF) (NaCl 87, KCl 2.5, NaH2PO4*H20 1.3, MgCl2*6H2O 7, NaHCO3 25, sucrose 75, ascorbate 5, CaCl2*2H2O 0.5 [composition in mM] in ddH20; osmolarity 322-326 mOsm, pH 7.20-7.30) saturated with carbogen gas (95 % oxygen, 5 % carbon dioxide). Following decapitation, the brain was rapidly removed from the cranial cavity and coronally dissected (AP: ~ -1.5 mm from bregma). Coronal 300 µm brain sections were prepared from the anterior portion of the brain containing the mPFC and striatum, using a vibrating microtome (Leica VT1000S, Leica Microsystems, Germany). The posterior portion of the brain was transferred to 4% paraformaldehyde (PFA) dissolved in 1x PBS for fixation and subsequent histological processing (see below in *Histology*). Brain slices were given at least 1 hr to recover in a holding chamber containing aCSF (NaCl 126, KCl 2.5, NaH2PO4*H20 1.25, MgCl2*6H2O 1, NaHCO3 26, glucose 10, CaCl2*H2O 2.4 [composition in mM]; in ddH20; osmolarity 298-301 mOsm; pH 7.28-7.32) saturated with carbogen gas at 32 °C before being transferred to the recording chamber for electrophysiological recordings.

Whole-cell patch-clamp recordings.

Once in the recording chamber, brain slices were continually perfused with fully oxygenated aCSF at a rate of 2 mL/min at 30-32 °C. Neurons were visualized using an upright

microscope (Scientifica, Uckfield, UK) equipped with IR-DIC optics and a QImaging Retiga EXi camera (QImaging, Surrey, BC, Canada) through a 40X water-immersion objective. Brief illumination through a 470 nm or 595 nm LED light source (pE-100; CoolLED, Andover, UK) was used to identify CTB-488 and CTB-555 expressing mPFC neurons, respectively, prior to recording. Whole-cell patch-clamp recordings were performed using glass electrodes (resistance 4-6 MΩ) pulled from thin-walled borosilicate glass capillary tubing (World Precision Instruments, Hertfordshire, UK) on a P-97 horizontal puller (Sutter Instrument, Novato, CA, USA) and filled with internal solution containing (in mM) potassium gluconate 125, NaCl 10, HEPES 20, Mg-ATP 3, neurobiotin 0.1 % in ddH20 (osmolarity 287, PH 7.33). For electrophysiological recordings signals were amplified using a Multiclamp 700B amplifier (Molecular Devices, CA, USA), digitized at 10 kHz using a Digidata 1550 (Molecular Devices, CA, USA), and recorded using Clampex 10.4 software (Molecular Devices, CA, USA). Capacitance, series resistance (R_s), and input resistance (R_{in}) were frequently measured during recordings to monitor cell health, using a 5 mV hyperpolarizing step in voltage-clamp. The resting membrane potential and the current-voltage (I-V) relationship of the neuron were determined in current-clamp mode using incremental 20 pA, 500 ms square current pulses from -120 pA to +260 pA. The instantaneous and steady-state action potential firing frequencies were calculated using the first 100 ms and last 300 ms of the current pulse, respectively.

In order to assess the effect of activating ChR2-expressing VTA (DA) terminals on mPFC neuron firing, a square current pulse (2 s duration) was applied in current-clamp mode to elicit stable firing (~2-6 Hz). After 20 s a 20 Hz train of 470 nm light (5 ms pulse duration) was delivered through the 40X objective for 3 s. During the last 2 s of this blue light train, the same square current pulse was applied to the cell. This protocol was repeated every 50 s and the firing during the current pulses (with and without blue light stimulation) was used for analysis. To determine the effect of VTA (DA) terminal stimulation on the rheobase of the neuron, the same

protocol was performed, but instead of a square current pulse, a 2 s current ramp was applied to the cell.

The D_2 antagonist raclopride was used in a subset of recordings during which a square current pulse was applied with and without optical stimulation of ChR2-expressing VTA (DA) terminals. Raclopride (Sigma-Aldrich, MO, USA) was prepared fresh at the start of each recording session and was dissolved in aCSF to give a final concentration of 10 μM. Raclopride was perfused onto the slice for at least 10 min before electrophysiological recordings were commenced.

Analysis of action potential firing was performed offline using Clampfit 10.4 software (Molecular Devices, Sunnyvale, CA) and passive membrane properties were computed using custom MATLAB software written by Praneeth Namburi based on MATLAB implementation of the Q-method[26].

Immunohistochemistry.

Following recording, slices were transferred to 4% PFA solution overnight at 4 °C, and were then washed 4 times (for 10 min each) in 1x PBS. Slices were then blocked in 1x PBS solution containing 0.3% Triton X-100 and 5% normal donkey serum (NDS; Jackson ImmunoResearch, PA, USA) for 1 h at room temperature. They were then incubated in primary antibody solution containing chicken anti-TH (1:1000; Millipore, MA, USA) in 1x PBS with 0.3% Triton X-100 (Thermo Fisher Scientific, MA. USA) and 3% NDS overnight at 4 °C. Slices were subsequently washed 4 times (for 10 min each) in 1x PBS and then incubated in secondary antibody solution containing Alexa Fluor 647-conjugated donkey anti-chicken (1:1000; Jackson ImmunoResearch, PA, USA) and 405-conjugated streptavidin (1:1000; Biotium, CA, USA) in 1x PBS with 0.1% Triton X-100 and 3% NDS for 2 h at room temperature. Slices were finally washed 5 times (for 10 min each) in 1x PBS, then mounted onto glass slides and cover-slipped using polyvinyl alcohol (PVA) mounting medium with DABCO (Sigma-Aldrich, MO, USA).

Ex vivo electrophysiology to determine latency for phototagging experiments.

Subjects & surgery.

To verify the latency of blue light-evoked action-potentials (AP) in ChR2-expressing mPFC-dPAG projectors, DAT::Cre mice were used which had received the same viral surgery as those for *in vivo* electrophysiology experiments. Viral incubation for *ex vivo* recordings was matched for those for *in vivo* experiments. For subject and surgery details, see below (*in vivo electrophysiology – Surgery*).

Brain slice preparation.

Brian slice preparation was similar to previously described. Briefly, mice were deeply anesthetized with sodium pentobarbital (90 mg/kg; IP) and transcardially perfused with 20 mL ice cold modified artificial cerebrospinal fluid (aCSF) (NaCl 87, KCl 2.5, NaH2PO4*H20 1.3, MgCl2*6H2O 7, NaHCO3 25, sucrose 75, ascorbate 5, CaCl2*2H2O 0.5 [composition in mM] in ddH20; osmolarity 322-326 mOsm, pH 7.20-7.30) saturated with carbogen gas (95 % oxygen, 5 % carbon dioxide). Following decapitation, the brain was rapidly removed from the cranial cavity and coronally dissected (AP: ~ 0 mm from bregma). Coronal 300 µm brain sections were prepared from the anterior portion of the brain containing the mPFC and striatum, using a vibrating microtome (Leica VT1000S, Leica Microsystems, Germany). The posterior portion of the brain was transferred to 4% paraformaldehyde (PFA) dissolved in 1x PBS for fixation and subsequent histological processing (see below in *Histology*). Brain slices were given at least 1 hr to recover in a holding chamber containing aCSF (NaCl 126, KCl 2.5, NaH2PO4*H20 1.25, MgCl2*6H2O 1, NaHCO3 26, glucose 10, CaCl2*H2O 2.4 [composition in mM]; in ddH20; osmolarity 298-301 mOsm; pH 7.28-7.32) saturated with carbogen gas at 32 °C before being transferred to the recording chamber for electrophysiological recordings.

Whole-cell patch clamp recordings.

Recordings were similar to those previously described above. Briefly, recordings were made from visually identified neurons expressing ChR2-eYFP and non-expressing neighbors. Blue light was provided by a 470 nm LED light source (pE-100; CoolLED, NY, USA) delivered through a 40X immersion objective. ChR2 expression in recorded neurons was confirmed by the presence of sustained inward current in response to 1 s constant pulse of blue light delivered in voltage-clamp mode.

Offline analysis was performed in Clampfit 1.4 software (Molecular Devices, Sunnyvale, CA). Latency to AP or excitatory postsynaptic potentials (EPSP) were peak averaged from 30 responses to a 5 ms pulse of blue light (delivered in a 10 pulse, 1 Hz train every 60 s). Latency was measured as the durations from the onset of the light pulse to the peak of the AP or EPSP.

Dopamine receptor localization on projector populations

Subjects.

Transgenic male and female Drd1a-Cre [n = 3, B6.FVB(Cg)-Tg(Drd1a-cre)FK150Gsat/Mmucd ; ID# 036916-UCD from MMRRC originally from GENSAT BAC Tg Project] and Drd2-Cre mice [n = 3, B6.FVB(Cg)-Tg(Drd2-cre)ER44Gsat/Mmucd ; ID# 032108-UCD from MMRRC originally from GENSAT BAC Tg Project] (~12 wks old) were group housed (2-4 subjects per cage) on a 12h:12h reverse light/dark cycle (lights off at 09.00 AM) throughout the duration of experiments with *ad libitum* access to food and water. Sample sizes was based on reports in related literature and were not predetermined by calculation. We thank Dr. Jill Crittenden (Graybiel Lab) for donating D1-TdTomato/D2-GFP mice and Dr. Teruhiro Okuyama (Tonegawa Lab) for donating Drd1a-Cre and Drd2-Cre mice.

Surgeries.

To label Drd1a- and Drd2-expressing mPFC neurons, AAV_5-EF1a-DIO-eYFP was injected bilaterally into the mPFC (AP: +1.8, ML: +0.3, DV: -2.75 & -2.4 [300 nl ea, bevel facing lateral]). Mice were allowed to recover and incubate for 4 wks. In a second surgery, 350 nl of Cholera Toxin subunit B (CTB) conjugated to Alexa Fluor-555, or 647 (Molecular Probes, Eugene, OR, USA) was injected into the dorsal periaqueductal gray (dPAG; AP: -4.2, ML: -0.5; DV: -2.4 mm) and NAc shell (AP: +1.0, ML: +0.75, DV: -4.5 mm) (in contralateral hemispheres, color counterbalanced) to retrogradely label mPFC-dPAG and mPFC-NAc projectors. Mice were sacrificed 6 days later as previously described. Histological, imaging, and data analyses are the similar to those previously described.

In vivo epifluorescent calcium imaging with optical manipulations

Subjects.

Male DAT::IRES-Cre mice (~ 8 wks old; mPFC-dPAG::GCaMP6m + VTA^{DA}::ChrimsonR/mCherry) were group housed (2-4 subjects per cage) on a 12h:12h reverse light/dark cycle (lights off at 09.00 AM) prior to and 4 weeks following initial virus and microendoscope (i.e., GRIN lens) implant surgery. Following baseplate adhesion, subjects were individually housed and placed on food restriction (3-6 grams normal chow / day) with *ad libitum* access to water for 3-6 days encompassing testing. Sample sizes was based on reports in related literature and were not predetermined by calculation.

Surgeries.

Subjects were prepared for *in vivo* epifluorescent calcium imaging similarly to methods described elsewhere (Jennings et al., 2015; Resendez et al., 2016). Briefly, to achieve projection-specific imaging, a virus encoding Cre-dependent GCaMP6m (AAV_5-CAG-Flex-GCaMP6m) was injected into the mPFC (AP: +1.8, ML: +0.3, DV: -2.75 & -2.4 [300 nl ea, bevel

facing lateral]) and retrogradely traveling canine adeno-associated (CAV) virus carrying Cre-recombinase (CAV2-Cre; Istitut de Génétique Moléculaire de Montpellier, France) was injected into the dPAG (n = 6; AP: -4.2, ML: +0.5, DV: -2.4 [350 nl]) or the nucleus accumbens shell (n = 5; AP: +1.0, ML: +0.75; DV: -4.5 [350 nl]). For manipulation of DA terminals in mPFC-dPAG::GCaMP6m + VTA^{DA}::ChrimsonR subjects (n = 4), DAT::IRES-Cre mice received 1 ul of AAV_8-hSyn-FLEX-ChrimsonR-tdT in the VTA (AP: -3.4, ML: +0.4, DV: -4.25). Control mice (mPFC-dPAG::GCaMP6m + VTA^{DA}::mCherry; n = 5), received 1ul of AAV_5-DIO-EF1a-mCherry into the VTA using the same coordinated. After virus infusions, the mPFC craniotomy was enlarged to >1 mm in diameter and dura removed with a bent 30 gauge beveled needle, but no tissue was aspirated. A 1 mm diameter, ~4 mm length gradient refractive index lens (GRIN lens; =GLP-1040, Inscopix, Palo Alto, CA) was held via vacuum on the tip of a blunted needle surrounded by plastic tubing for stability and was lowered stereotaxically through the craniotomy under constant saline perfusion to minimize tissue/blood desiccation. Lenses were implanted slightly posterior and lateral of the needle track for virus infusions to avoid tissue damage in the imaging plane, and were lowered to locations in the ventral PL / dorsal IL subregion of the mPFC (AP: -1.77, ML: -0.4, DV: -2.32, mm from bregma). Lens implants were secured to the skull with a thin layer of adhesive cement (C&B Metabond; Parkell, Edgewood, NY, USA), followed by black cranioplastic cement (Ortho-Jet; Lang, Wheeling, IL, USA) containing gentamicin antibiotic. Lenses were covered with the top of an eppendorf tube and cemented in place with cranioplastic cement for protection during the virus incubation period (3-4 wks). The implant was allowed to completely dry before closure of the incision with nylon sutures.

Following virus incubation, mice were again anesthetized with isofluorane, streotaxically secured, and baseplates (Inscopix, Palo Alto, CA) were cemented around the lens to support the connection of the miniaturized microscope for *in vivo*, freely moving imaging. During this procedure, the protective eppendorf cap and supporting cranioplastic cement were removed

using a hand drill. The exposed top of the GRIN lens was scrubbed clean with a cotton-tipped applicator soaked with 15% isopropyl alcohol diluted in ddH_20. Next, a miniaturized microscope (single channel epifluorescence, 475 nm blue LED, Inscopix, Palo Alto, CA) with the baseplate attached was stereotaxically positioned over the implanted GRIN lens and adjusted in the DV axis in order to focus on visible landmarks (i.e., GCaMP6m expressing neurons and blood vessels). After the focal plane was identified, the microscope/baseplate was raised by ~50 um, to account for cement shrinkage, and was subsequently cemented in place with pink dental cement (Stoelting, Wood Dale, IL, USA). The microscope was then detached from the baseplates, a final layer of black cranioplastic cement (Ortho-Jet; Lang, Wheeling, IL, USA) was applied to prevent light leak, and the implant was covered with a protective plate (Inscopix, Palo Alto, CA) until imaging.

Recording from mPFC-dPAG neurons while manipulating VTA^{DA} terminal activity.

Following recovery, DAT::Cre mice were individually housed and food restricted for 2 days prior to recording. Prior to the recording day, food-deprived mice were habituated to handling and the nVoke miniaturized microscope (an integrated imaging and optogenetics system, 450 nm blue GCaMP excitation LED, 620 nm amber optogenetic LED, Inscopix, Palo Alto, CA). 24 hrs prior to recordings, mice were habituated in their homecage to a dimly lit recording room containing constant white noise (Marpac Dohm-DS dual speed sound conditioner, Wilmington, NC, USA). On the recording day, mice were attached to the nVoke miniaturized microscope and habituated in their homecage for 15 min. After the 15 min habituation, a 30 min recording session, composed of 10 min OFF-ON-OFF epochs, was initiated. Gray scale images were collected at 10 frames per second using 0.094-0.266 mW x mm^2 (estimated light power based on GRIN lens efficiency) of the miniaturized microscope's 450 nm LED transmission range (nVoke 2.1.5., Inscopix, Palo Alto, CA). During the ON epoch,

20 Hz, 60p (5 ms pulses) trains of 620 nm LED light were initiated every 30 s for the duration of the 10 min epoch.

Image processing.

Image processing was accomplished using Mosaic software (Version 1.1.2., Inscopix, Palo Alto, CA). Raw videos were pre-processed by applying x4 spatial downsampling to reduce file size and processing time, and isolated dropped frames were corrected. No temporal downsampling was applied. For sucrose/shock experiments, both recordings per animal (i.e., "Sucrose" recording and "Shock" recording) were concatenated to generate a single 30 min video. Lateral movement was corrected for by using a portion of a single reference frame (typically a window surrounding a prominent blood vessel or constellation of bright neurons). Images were cropped to remove post-registration borders and sections where cells were not observed. 2 method were used for ROI identification and single-cell fluorescence trace extraction in order to verify that these processes did not significantly change the pattern of results within our data sets. Both methods are described below in *CNMF-E analyses* and *non-ROI analyses*. The results from the CNMF-E analyses are reported in **Figure 13 and Figure 19**. The results from the non-ROI analyses are reported in **Figure 14**.

CNMF-E analyses.

After motion correction and cropping, recordings were exported as .tif z-stacks and were downsampled to 10 frames per second. We used a constrained non-negative matrix factorization algorithm optimized for micro-endoscopic imaging (CNMF-E) (Zhou et al., 2018)was used to extract fluorescence traces from ROIs. ROIs were defined by manually selecting seed pixels from peak-to-noise (PNR) graphs of the FOV (Murugan et al., 2017). Considering calcium fluctuations can exhibit negative transients, associated with a pause in firing (Otis et al., 2017), we did not constrain values to > 0 – as such we refer to this process as "C(N)MF-E".

Non-ROI analyses.

After motion correcting and cropping, recordings were converted to a changes in fluorescence compared to background fluorescence (F-F0)/F0 using the mean Z-projection image of the entire movie as reference (F0). Calcium signals arising from individual regions of interest (ROIs, i.e., cells) were identified using independent and principal component analyses (PCA/ICA). Identified PCA/ICA filters were thresholded at their half-max values to define possible ROIs. ROIs were then screened for neuronal morphology and only accepted if the threshold filters included only on contiguous region with an eccentricity of <0.85 and an area between 30-350 pixels. Accepted ROI filters were merged if their areas overlapped by more than 60% after visual confirmation. The accepted ROI filters were then reapplied to the motion corrected videos to extract dF/F0 traces for each ROI. In order to correct for bleaching and possible neuropil contamination of the extracted ROI trace, we correct each ROI tracing using signals from the whole field, using a multiple step procedure: The full ROI trace and the signals from the whole field were filtered using a 30 s median filter to eliminate the influence of sharp transients or outliers. The influenced of the surrounding signals on the ROI trace were quantified using regression (*glmfit* in MATLAB). The resulting regression coefficient was then applied to the original, unfiltered trace to regress out the influence of the non-ROI thresholded field on the ROI trace itself. Multiple background subtraction were examined and a non-ROI thresholded approach was implemented because 1) this approach excludes subtraction of prominent processes (i.e., dendrites and axons) observed in our data set, 2) the reasonable correlation coefficients between individual ROIs (i.e., within the range that would expected based on electrical recordings). To acquire the non-ROI thresholded image for background subtraction, max Z-projections of individual recordings were created and thresholded to separate ROIs and their processes from the rest of the field of view. Average signal from the remaining pixels was

used as a proxy for the whole field changes in fluorescence, and regressed of the signal from each ROI.

Data analysis.

Individual lick bouts were characterized by lick events detected at the sucrose lickometer and events that were separated by >1 s were identified as an individual lick bout. Calcium signals for the bulk FOV fluorescence and for each ROI were aligned to behavioral events (i.e., lick bout initiation and shock). Population z-scores were calculated using the period -10 to -5 s prior to stimuli onset as baseline. ROIs were classified as being stimulus excited if the average z-score 0-1 s after stimulus onset was greater than 3. Calcium event quantifications (number and amplitude) were performed in MiniAnalysis (Synaptosoft, Decatur, GA) using individual ROI traces from the entire session after conversion to z-score. Baseline from the z-transform was computed by thresholding the signal at 20% of the signal amplitude. Calcium events with z-scores <8 or did no did not have a > 0.5 AUC were not included in analyses because events of this magnitude were did not reliably retain transient, calcium-event characteristics across animals. ROIs which did not contain events that met event criterion were excluded.

We thank Drs. Ilana Witten, Courtney Cameron, Nathan Parker, Malavika Murugan, Pengcheng Zhou and Liam Paninski for advice and code for CNMF-E analysis. We thank Dr. Mark Schnitzer for advice regarding data analyses and endoscopic imaging. The authors wish to acknowledge Inscopix, Inc. for a scientific collaboration – particularly Lara Cardy and Dr. Alice Stamatakis of Inscopix, Inc. for technical assistance.

***In vivo* electrophysiology.**

Subjects.

Male DAT::IRES-Cre mice (~6-8 wks old) were group housed (2-4 subjects per cage) on a 12h:12h reverse light/dark cycle (lights off at 09.00 AM) throughout the duration of experiments. Two days after head-bar adhesion (~2 wks before recordings), cages were placed on food restriction (4 hrs access to standard chow / day) with *ad libitum* access to water throughout training and recording. Sample sizes was based on reports in related literature and were not predetermined by calculation.

Surgery.

To achieve projection-specific ChR2 expression for *in vivo* photoidentification of mPFC-dPAG projecots, a virus encoding Cre-dependent ChR2 (AAV_5-Ef1a-DIO-ChR2-eYFP) was injected into the mPFC (AP: +1.8, ML: +0.3, DV: -2.75 & -2.4 [300 nl ea, bevel facing lateral]) and retrogradely traveling canine adeno-associated (CAV) virus carrying Cre-recombinase (CAV2-Cre; Institut de Génétique Moléculaire de Montpellier, France) was injected into the dPAG (AP: -4.2, ML: +0.5, DV: -2.4 [350 nl]). For manipulation of DA terminals, DAT::IRES-Cre mice received 1 ul of AAV_8-hSyn-FLEX-ChrimsonR-tdT in the VTA (AP: -3.4, ML: +0.4, DV: -4.25).

Head-bar adhesion.

After 11+ weeks of virus incubation, and ~2 weeks prior to behavioral training, mice were briefly anesthetized small aluminum head-bar (2 cm*2 mm*2 mm) was placed on the skull 5 mm posterior to the bregma along with one reference and one ground pin contacting the dura mater just anterior to the head-bar, in the contralateral cortex. A small pilot hole was made with a cranial drill above the mPFC and was marked with a pen. The area surrounding the pilot hole/mark was covered with petroleum jelly to prevent covering with dental cement. The three elements (head-bar, ground pin and reference pin) were cemented using one layer of adhesive cement (C&B metabond; Parkell, Edgewood, NY) followed by a layer of cranioplastic cement (Dental cement; Stoelting, Wood Dale, IL). After the cement dried, the pilot hole/mark was

covered with a silicone gel (Kwik-Sil Adhesive, WPI, Sarasota, FL) to keep the bone clear during behavioral training.

Behavior.

2 days after head-bar adhesion, mice were food restricted and pre-exposed to a 30% sucrose solution. Mice were head-fixed[27] in front of two small tubes one located just under the nose and the other above it pointed at the nose. The bottom tube delivered sucrose (training and recording days) and the top tube delivered airpuff (recording days only). Mice we trained to retrieve small drops (3 μL) of sucrose delivered through the bottom tube via a solenoid valve (Parker, Cleveland, OH), measured by breaks of an infrared beam recorded by an Arduino board (SmartProjects, Italy). Training sessions gradually increased in total duration (0.5 – 1.5 hr) and sucrose ITIs increased (15 – 80±8 s) over 5-8 days. The solenoid valves were triggered with a custom software written in LABVIEW (National instruments, Austin, TX) powered by NIDAQ-6251 and Arduino hardware.

Pre-recording craniotomy.

After 5-8 days of habituation and training, mice were briefly anesthetized with isoflurane (5% for induction, 1.5% after) and placed in a stereotaxic frame while their body temperature was controlled with a heating pad. A craniotomy was performed over the mPFC using the pilot hole/mark previously implemented using a hand-held drill. When the craniotomy was open, the dura was removed, blood cleaned with perfusion of saline, and then covered with petroleum jelly. Mice were removed from the stereotaxic and placed in a clean cage while their body temperature was maintained using a heat lamp until fully they recovered from anesthesia.

In vivo electrophysiological recordings and phototagging.

Once the mice recovered from the craniotomy surgery (at least 1 hr), they were head-fixed and a silicon optrode (A1x16-Poly2-5mm-50s- 177, NeuroNexus, Ann Arbor, MI) coated

with red fluorescent latex microspheres (Lumafluor Inc.) was inserted into the anterior mPFC and lowered from the surface of the cortex for 1 mm at 10 µm/s using a motorized actuator (Z825B - 25 mm Motorized Actuator, Thorlabs, Newton, NJ, USA) mounted on a shuttle (460A linear stage, Newport, Irvine CA, USA) fixed to the stereotaxic arm. Next, the optrode was lowered for 1 mm at 1-2 µm/s. During the insertion of the electrode, sucrose was delivered every 60±8 s. After the probe was lowered to -2 mm below brain surface, sucrose deliveries were halted and a 10 min wait period commenced to let the tissue stabilize around the recording probe. Recording sessions were initiated using a RZ5D TDT system (Tucker-Davis Technologies, Alachua, FL, USA) while presenting ~ 40 sucrose and 40 airpuff trials (10-12±4 s ITI) randomly intermixed throughout the entire 30 min recording period. The recording period was broken into three 10 min epochs: 10 min into the recording period (first OFF epoch), 593 nm laser light pulse trains (20 Hz, 60 p, 5 ms pulses) were delivered through the optrode every 30 s for 10 min (20 pulse trains total, ON epoch). 10 more minutes were recorded in the absence of laser manipulation (second OFF epoch) – resulting in an OFF-ON-OFF epoch structure, with laser delivery only occurring during the ON epoch. Following completion of 30 min recording session, a photoidentification session using a 473 and/or 405 nm laser was conducted, during which pseudorandomly dispersed stimulations were delivered: 1 s constant light, 10x 1 Hz, 5 ms pulse trains, and 100 ms of 100 Hz (5 ms pulses). Recordings were then terminated and the optorde was lowered 300 um to a new recording site at 1-2 µm/s. The recording protocol was then repeated after a 30 min inter-session interval. Recordings sessions continued until we reached the bottom of the mPFC (-3 mm from brain surface) or when mice became sated and stopped retrieving sucrose. The electrode was then retracted at 5 µm/s, the craniotomy cleaned with saline, and covered with silicone gel (Kwik-Sil Adhesive, WPI, Sarasota, FL) to protect the brain until the next day of recording. During the second day of recording, the same procedure was repeated in a more posterior recording location. Following completion of the second day of recordings, mice were anesthetized with sodium pentobarbital

and transcardially perfused. The brain was extracted, sectioned, and examined under a confocal microscope to verify the viral expression and the locations of the recording electrode.

Analysis of in vivo electrophysiological recordings.

Recording sessions were exported from the TDT format to Plexon offline sorter using OpenBridge (Tucker-Davis Technologies, Alachua, FL, USA). Offline sorter (Plexon, Dallas, TX, USA) was used to sort single units. Neural responses to sucrose / airpuff delivery and light stimulation were visualized through peristimulus time histograms (PSTH) and rasters for every unit using NeuroExplorer.

Data from Plexon and Neuroexplorer data files was then imported into MATLAB and analyzed using software written by P.N. Sucrose and airpuff PSTHs for each epoch (OFF-ON-OFF) were z-transformed using the histogram values in a 2 s baseline period starting 3 s prior to the onset of the stimulus. Similarly, PSTHs around a light pulse (used for photo identification of dPAG projectors) were z-transformed using a baseline window of 40 ms prior to the onset of the light pulse. To test significance of neural responses, Wilcoxon signed-rank test was performed on the neural activity of each unit by comparing the number of spikes in a baseline window and an experimental window starting at the onset of stimulus or light pulse. The experimental window for mean stimulus response was set to 0.5 s. The experimental window for light response was 10 ms based on the results of the *ex vivo* recordings. Significance threshold for the Wilcoxon signed rank test was set at $p < 0.01$. Latency to the light pulse was defined as the first bin in the PSTH to cross 4 standard deviations relative to the 40 ms baseline window. Only units which met both criterion were considered phototagged and thus mPFC-dPAG projectors.

Histology

Perfusion and storage.

Subjects were deeply anesthetized with sodium pentobarbital (200 mg/kg; i.p.) and transcardially perfused with 15 mL (mouse) / 60 mL (rat) of Ringers solution followed by 15 mL (mouse) / 60 mL (rat) of cold 4% paraformaldehyde (PFA) dissolved in 1x PBS. Animals were decapitated and the brain was extracted from the cranial cavity and placed in 4% PFA solution and stored at 4 °C for at least 48 hrs. 36 hrs before tissue sectioning, brains were transferred to 30% sucrose solution dissolved in 1x PBS at room temperature. Upon sinking, brains were sectioned at 60 um on a freezing sliding microtome (HM420; Thermo Fischer Scientific). Sections were stored in 1x PBS at 4 °C until mounting and imaging.

Confocal microscopy.

Fluorescent images were captured using a confocal laser scanning microscope (Olympus FV1000), with FluoView software (Olympus, Center Valley, PA), under a dry 10x / 0.40 NA objective, a 60x/1.42 NA oil immersion objective, or a 40x /1.30 NA oil immersion objective. The locations of opsin expression, injection site, lesion from the optic fiber placement, and the position of recording electrodes were determined by taking serial z-stack images through the 10x objective across a depth of 20-40 µm, with an optical slice thickness of 5-8 µm. High magnification images fluorescence quantifications were obtained through the 40x or 60x objective using serial z-stack images with an optical slice thickness of 3-4 µm (5 slices) using matched parameters and imaging locations.

Sholl analysis.

Neurobiotin-filled/streptavidin stained mPFC-dPAG and mPFC-NAc projectors from *ex vivo* electorphysiology experiments were imaged at 40 x (1.30 NA oil immersion objective) using a confocal laser scanning microscope (Olympus FV100) covering the whole dendritic and axonal arborization in the slice. Neurons were reconstructed and Sholl analysis (# of intersections, 20 um rings from soma) performed using the "Simple Neurite Tracer" plugin contained in FIJI ImageJ.

Statistics

Statistical analyses were performed using GraphPad Prism (GraphPad Software, Inc, La Jolla, CA) and MATLAB (Mathworks, Natick, MA). Group comparisons were made using one-way or two-way ANOVAs followed by Bonferroni post-hoc tests to control for multiple comparisons. Paired and unpaired two-way Student's t-tests were used to make single-variable comparisons. Unpaired one-way t-tests were used to make comparisons with a priori hypotheses. Tests for binomial distribution were also used on single populations. Non-parametric Wilcoxon signed rank tests were used to make comparisons between non-parametric data (*in vivo* calcium-imaging and electrophysiology data). Chi square tests were used to compare distribution of shock and sucrose responsive cells between mPFC-dPAG and mPFC-NAc. All statistical tests are two-sided unless otherwise noted as an *a priori* hypothesis. Thresholds for significance were placed at $*p < 0.05$, $**p < 0.01$, $***p < 0.001$. All data are shown as mean ± standard error of the mean (SEM).

Summary

Our data show that activation of dopamine terminals in the mPFC inhibits NAc-projectors via a D2-dependent mechanism in *ex vivo* brain slices. Consistent with this, a considerable proportion of mPFC-NAc neurons (~86%) express D2-receptors. In contrast, mPFC-dPAG neurons do not robustly express D1- or D2-receptors and their intrinsic excitability is not modulated by dopamine terminal activation *ex vivo*. However *in vivo,* where excitatory inputs are intact, dopamine sharpens mPFC-dPAG neuronal responses to aversive stimuli.

Author Contributions

Conception. Caitlin M. Vander, Gillian A. Matthews, and Kay M. Tye

Surgical injections and implantations. Caitlin M. Vander Weele, Cody A. Siciliano, Isabella C. Espinel

Cell Counting. Caitlin M. Vander Weele, Isabella C. Espinel, Cody A. Siciliano

In vivo Calcium-Imaging recordings. Caitlin M. Vander Weele and Cody A. Siciliano

In vivo Calcium-Imaging analysis. Caitlin M. Vander Weele, Cody A. Siciliano, Praneeth Namburi, Eyal Y. Kimchi

Ex Vivo Electrophysiology. Gillian A. Matthews

In Vivo Electrophysiology Recordings. Caitlin M. Vander Weele and Anna Beyeler

In Vivo Electrophysiology Analysis. Caitlin M. Vander Weele, Anna Beleyer, Praneeth Namburi, Tony Burgos-Robles, Kay M. Tye

Histology. Caitlin M. Vander Weele, Gillian A. Matthews, Nancy Padilla

Confocal Microscopy and Cell Reconstructions. Caitlin M. Vander Weele and Gillian A. Matthews

Chapter 5

Dopamine in the prefrontal cortex enhances signal-to-noise for aversive stimuli via projections to the periaqueductal gray

Summary

In these studies, we provide a potential neural circuit mechanism by which dopamine may be translated into an aversive signal that promotes avoidance. First, using electrochemical approaches, we reveal the precise time course of tail pinch-evoked dopamine release in the mPFC. Second, we show that dopamine signaling in the mPFC biases behavioral responses to punishment-predictive stimuli, rather than reward-predictive cues. Third, in contrast to the well-characterized mPFC-NAc projection, we show that activation of mPFC-dPAG neurons is sufficient to drive place avoidance and defensive behaviors. Fourth, to determine the natural dynamics of individual mPFC neurons, we performed single-cell projection-defined microendoscopic calcium imaging to reveal a robust preferential excitation of mPFC-dPAG, but not mPFC-NAc, neurons to aversive stimuli. Finally, photostimulation of VTA dopamine terminals in the mPFC revealed an increase in signal-to-noise ratio in mPFC-dPAG neuronal activity during the processing of aversive, but not rewarding stimuli.

Discussion

Theories of mesocortical dopamine function suggest that dopamine neurotransmission in the mPFC supports behavioral flexibility (Euston et al., 2012; Miller and Cohen, 2001) and stimulus discrimination (Popescu et al., 2016; Williams and Goldman-Rakic, 1995). Several microdialysis studies have reported enhancements in extracellular dopamine release in the mPFC following exposure to rewarding stimuli, specifically food consumption (Ahn and Phillips,

1999; Bassareo et al., 2002; Hernandez and Hoebel, 1990; St. Onge et al., 2012), yet the relationship between reward and dopamine efflux in the mPFC is complex (Phillips et al., 2004). Paradoxically, non-psychostimulant addictive drugs (e.g., morphine, ethanol, nicotine) do not enhance dopamine release in the mPFC (Bassareo et al., 1996), despite their rewarding and reinforcing properties. Further, drugs that do enhance dopamine concentrations in the mPFC (e.g., antidepressants) are often not abused (Tanda et al., 1994). These data suggest that rewarding stimuli do not reliably evoke dopamine release in the mPFC. Further, microdialysis, the neurochemical recording tool utilized in these studies, typically entails sampling extracellular dialysate over a period of >10 minutes, which fails to provide a real-time time course of dopamine concentration. While these microdialysis studies suggest that that certain rewarding conditions may enhance tonic dopamine neurotransmission in the mPFC, the lack of temporal specificity occludes the conclusion that rewarding events evoke time-locked, phasic dopamine release.

Recently phasic dopamine responses were reported from VTA dopamine terminals in the mPFC in response to reward, measured by *in vivo* fiber photometry (Ellwood et al., 2017). Here they observed an increase in calcium signals in response to reward-predictive cues and reward-delivery. Importantly, bulk calcium signals, like those recorded by Ellwood and colleagues, have been shown in the striatum to faithfully reflect dopamine neurotransmission *in vivo* (Parker et al., 2016). Indeed, this pattern of responses looks similar to those recorded in the NAc using *in vivo* fast-scan cyclic voltammetry in a similar Pavlovian conditioning paradigm (Day et al., 2007). These data suggest that dopamine neurotransmission in the mPFC does play a role in reward-related processes, consistent with previous reports (Popescu et al., 2016).

However Ellwood and colleagues did not also investigate dopamine responsivity to aversive stimuli, omission of reward, or under competitive situations. Given the mesocortical dopamine pathway is uniquely sensitivity to stressful and aversive stimuli (Abercrombie et al., 1989; Kim et al., 2016; Lammel et al., 2011; Mantz et al., 1989; Thierry et al., 1976) and our

data show that mesocortical dopamine biases behavior toward aversion under competitive conditions, it remains plausible that dopamine neurotransmission functions differently in "safe" situations (i.e., in contexts where no aversive stimuli have been encountered). To our knowledge, the only study to examine fast dopamine activity in the mPFC to rewarding and aversive stimuli reported an enhancement in bulk GCaMP signals in VTA dopamine terminals in response to tail shock, but not reward delivery. The opposite pattern of responses was observed in the NAc, where dopamine terminals were activated by reward and inhibited by tail shock (Kim et al., 2016). Yet how this sensitivity is integrated into theories of mesocortical dopamine function has not been resolved, despite evidence suggesting it is important for efficient escape/avoidance behaviors (Sokolowski et al., 1994).

Threatening environmental stimuli require immediate disengagement from ongoing behavior and engagement of escape and avoidance strategies. Threat avoidance necessitates a robust strategy-switching signal, which requires tuning of valence-defined circuits. Our data suggest dopamine release may serve to sharpen responses to motivationally significant stimuli by simultaneously enhancing the signal-to-noise in aversion-encoding pathways and inhibiting pathways that contribute to other behaviors. Therefore, while it is still debated whether mesocortical dopamine release is innately aversive (Ellwood et al., 2017; Gunaydin et al., 2014; Popescu et al., 2016), our data suggest that dopamine in the mPFC primes neural circuits that encode aversive stimuli in order to promote avoidance and escape-related behavior.

The notion that dopamine can alter signal-to-noise is attractive, as dopamine-mediated increases in signal-to-noise could explain its diverse behavioral and cognitive functions – ranging from improvements in attention and working memory, as well as reduced schizophrenic hallucinations (Jensen et al., 2008). Despite the popularity of the signal-to-noise model for mPFC dopamine in computational and theoretical neuroscience (Cohen and Servan-Schreiber, 1992; Cohen et al., 2002; Durstewitz and Seamans, 2008; Rolls et al., 2008), the degree to

which it translates across brain functions is unknown. Support for dopamine-mediated signal-to-noise has been found *ex vivo* (Kroener et al., 2009; Seamans et al., 2001b), and *in vivo* during auditory stimulus discrimination (Popescu et al., 2016), working memory (Williams and Goldman-Rakic, 1995), and visual cortex orientation selectivity (Noudoost and Moore, 2011). Our data suggest that distinct mPFC ensembles are modulated by dopamine under certain conditions and experiences. The fine-tuning of valence-defined subpopulations can result in the vast array of computations and behavioral outcome attributed to the mPFC.

Dopamine in the mPFC has been linked to mood disorders, such as stress, anxiety, and depression (Arnsten, 2009; Tanda et al., 1994; Thierry et al., 1976) – raising the possibility that dopamine may change general affective states rather than transmitting a discrete aversive signal. Indeed, stressful and noxious stimuli increase dopamine release in the mPFC (Abercrombie et al.; Finlay et al., 1995; Bassareo et al., 2002) and recently Gunaydin and colleagues (2014) reported that activation of VTA dopamine terminals in the mPFC evoked an anxiety-like phenotype measured in the elevated plus maze. However, anti-depressant and anti-anxiety drugs with different mechanisms of action (e.g., fluoxetine, desipramine, imipramine, buspirone) consistently increase dopamine release in the mPFC (Tanda et al., 1994). Further, in stark contrast to reports by Gunaydin and colleagues (2014), another study has shown that selective dopamine depletion in the mPFC is anxiogenic in the elevated plus maze (Espejo, 1997). Of course, dopamine's postsynaptic effects depend the type of dopamine receptor it activates. Considering tonic and phasic stimulation parameters evoke different levels of dopamine in the mPFC (Ellwood et al., 2017) causing differential activation of D1- and D2-receptors (Dreyer et al., 2010, 2016), these disparate findings may be accounted for by varying degrees of mesocortical activation. Clearly a deeper investigation into the role of the mesocortical dopamine system in regulating mood is required.

The PAG has also been implicated in anxiety (Brandão et al., 2008; Fanselow, 1991; Jenck et al., 1995). We observed different effects on two tasks often classified as anxiety assays upon activation of mPFC projections to the dPAG. The open field test is an exploratory task that uses the relative time spent in the center versus the periphery of the apparatus as a proxy for the general anxiety level of the animal (for review, see: Calhoon and Tye, 2015), whereas the marble burying assay presents novel discrete stimuli that the animal may interpret as threatening and measures digging behavior (burying is a defensive behavior for rats and mice) (De Boer and Koolhaas, 2003). We speculate that the robust positive result observed in the marble burying assay juxtaposed with the negative result for the open field test suggests that the mPFC-dPAG projection may be selective for threat interpretation in the presence of discrete cues, but not general contextual cues. This would be consistent with our data showing that activation of dopamine terminals in the mPFC biases behavior toward aversion in response to discrete cues, but does not support aversion in traditional place preference / avoidance assays.

The observation that the mPFC-NAc pathway did not robustly encode sucrose reward, nor promote place preference was surprising given studies implicating this projection in these processes (Britt et al., 2012; Otis et al., 2017; Ye et al., 2016). However the NAc is a heterogeneous structure composed of anatomically distinct subregions, the NAc shell and core (Heimer et al., 1997). Considering different territories and cellular subtypes are differentially involved in reward and aversion in the NAc (Al-Hasani et al., 2015; Badrinarayan et al., 2012; Budygin et al., 2012; Kim et al., 2017) and that mPFC-NAc projectors may collateralize to other downstream targets (e.g., claustrum, insula, amygdala), it is possible that non-selective targeting sends mixed or irrelevant downstream signals. In addition, the mPFC also sends long-range GABAergic projections to the NAc and activation of this pathway evokes avoidance behavior (Lee et al., 2014), further complicating the interpretation of our present findings.

Considering the mPFC-NAc pathway can be further dissected into molecularly defined circuits (Kim et al., 2017), future studies should investigate these nuances.

Caveats

Calcium transients are linearly- and monotonically-related to action potentials (Chen et al., 2013; Otis et al., 2017). Our observed increase in calcium transient amplitude and decrease in frequency suggests that dopamine is modulating the pattern of mesocortical dopamine neuron firing, perhaps by increasing phasic bursting activity. However it is important to note that while neuromodulators, like dopamine, can act presynaptically to regulate the probability of action potential-evoked neurotransmitter release by changing the size and properties of presynaptic vesicle pools, dopamine also has indirect effects on release probability by influencing channels that impact action potential-evoked calcium influx (for review, see: Tritsch and Sabatini, 2012). Considering dopamine can alter intracellular calcium handling (Gee et al., 2012; Surmeier et al., 1995) and may directly modulate calcium channels, it is possible that dopamine may alter calcium activity without affecting spiking; thus, the interpretation of our calcium imaging results alone is limited. However, the addition of our *in vivo* electrophysiology data set showing an enhancement in neuronal responses to airpuff by dopamine in mPFC-dPAG projectors bolsters our claim that dopamine enhances signal-to-noise in this pathway.

Transgenic D1- and D2-receptor mouse lines identify cells with transcriptionally active dopamine receptor genes but most dopamine transgenic mouse lines were selected based on accurate D1- and D2-receptor transgene expression in striatal neurons (Ade et al., 2011; Shuen et al., 2008) – which many not translate into high-fidelity transgene expression in the cortex. Indeed, discrepancies have reported which highlight the importance of interpreting results from these lines with caution. For example, Zhang and colleagues (2010) reported over 90% and ~20% of mPFC neurons express D2- and D1-receptors, respectively, using a Drd2-

EGFP/Drd1a-tdTomato BAC transgenic line. These numbers greatly contrast with earlier reports of D1- and D2- mRNA expression (D1 = <20-40%; D2 = <25%) (Gaspar et al., 1995; Santana et al., 2009). Further, Zhang and colleagues (2010) do not report robust differences in layer localization, which also contrasts with previous reports (Gaspar et al., 1995). Given these disparities, results obtained with these transgenic lines should be interpreted with caution and with these caveats in mind – particularly when utilized outside of the striatum.

While out of the scope of the current investigation, the mPFC also expresses D3- and D4-receptors, a subtype of D2-type receptors, which profoundly impact behavior (for review, see: Lauzon and Laviolette, 2010; Nakajima et al., 2013). D3-expressing mPFC neurons do not co-express D1- or D2-receptors and are also located on mPFC-NAc projectors (Clarkson et al., 2017); however the precise behavioral function of this specific subpopulation of mPFC-NAc neuron has yet to be determined. D4-receptors have been implicated in the encoding of associative fear memories in the mPFC (Laviolette et al., 2005), but whether D4-receptors are expressed on either mPFC-NAc or mPFC-dPAG neurons is unknown. Investigation into the subpopulations is an interesting avenue for future research.

Claims regarding differential mPFC circuit regulation by dopamine *in vivo* are hampered by our current inability to interrogate the mPFC-NAc circuit in the same manner as the mPFC-dPAG circuit, using *in vivo* calcium imaging and electrophysiology with phototagging. Considering the VTA projects to the NAc, the use of two Cre-dependent systems within the same subject is impossible with the tools available. We made several attempts to use a Flp dependent system using a herpes simplex virus (HSV) preparation (HSV-Flp) and later, a CAV2-Flp, paired with a Flp-dependent GCaMP. We were unable to observe any recombination using the HSV virus to carry Flp – which we hypothesize may be due to HSV toxicity. While not currently feasible, *in vivo* characterization of dopamine's effect on this subpopulation is of great interest and should be the subject of future studies as new genetic-targeting tools become

available. However, we find *ex vivo* electrophysiology data to be consistent with previously reported *in vivo* recordings – also showing attenuated responses via a D2-dependent mechanism within the mPFC and NAc circuit (Brady and O'Donnell, 2004).

Clinical relevance

These findings have clinical relevance to neuropsychiatric disorders characterized by dopamine dysregulation in the mPFC. For example in schizophrenia, hyperdynamic mesocortical dopamine signaling may prime aversion-encoding pathways and underlie pathologies in paranoid schizophrenia, such as the tendency to assign negative motivational salience to otherwise neutral stimuli (Goldman-Rakic and Selemon, 1997; Howes and Kapur, 2009; Jensen et al., 2008; Winton-Brown et al., 2014). Our data suggest that mesocortical dopamine differentially tunes mPFC circuits and highlights the need for targeted dopamine therapies in projection-defined circuits in the mPFC.

Chapter 6

References

Abercrombie, E.D., Keefe, K.A., DiFrischia, D.S., and Zigmond, M.J. (1989). Differential effect of stress on in vivo dopamine release in striatum, nucleus accumbens, and medial frontal cortex. J. Neurochem. *52*, 1655–1658.

Ade, K.K., Wan, Y., Chen, M., Gloss, B., and Calakos, N. (2011). An Improved BAC Transgenic Fluorescent Reporter Line for Sensitive and Specific Identification of Striatonigral Medium Spiny Neurons. Front. Syst. Neurosci. *5*, 32.

Adolphs, R. (2009). The Social Brain: Neural Basis of Social Knowledge. Annu. Rev. Psychol. *60*, 693–716.

Ahn, S., and Phillips, A.G. (1999). Dopaminergic correlates of sensory-specific satiety in the medial prefrontal cortex and nucleus accumbens of the rat. J. Neurosci. Off. J. Soc. Neurosci. *19*, RC29.

Akerboom, J., Carreras Calderón, N., Tian, L., Wabnig, S., Prigge, M., Tolö, J., Gordus, A., Orger, M.B., Severi, K.E., Macklin, J.J., et al. (2013). Genetically encoded calcium indicators for multi-color neural activity imaging and combination with optogenetics. Front. Mol. Neurosci. *6*, 2.

Albanese, A., and Minciacchi, D. (1983). Organization of the ascending projections from the ventral tegmental area: a multiple fluorescent retrograde tracer study in the rat. J. Comp. Neurol. *216*, 406–420.

Al-Hasani, R., McCall, J.G., Shin, G., Gomez, A.M., Schmitz, G.P., Bernardi, J.M., Pyo, C.-O., Park, S.I., Marcinkiewcz, C.M., Crowley, N.A., et al. (2015). Distinct Subpopulations of Nucleus Accumbens Dynorphin Neurons Drive Aversion and Reward. Neuron *87*, 1063–1077.

de Almeida, J., Palacios, J.M., and Mengod, G. (2008). Distribution of 5-HT and DA receptors in primate prefrontal cortex: implications for pathophysiology and treatment. Prog. Brain Res. *172*, 101–115.

Anand, B.K., and Brobeck, J.R. (1951). Hypothalamic control of food intake in rats and cats. Yale J. Biol. Med. *24*, 123–140.

Arnsten, A.F.T. (2009). Stress signalling pathways that impair prefrontal cortex structure and function. Nat. Rev. Neurosci. *10*, 410.

Assareh, N., Sarrami, M., Carrive, P., and McNally, G.P. (2016). The organization of defensive behavior elicited by optogenetic excitation of rat lateral or ventrolateral periaqueductal gray. Behav. Neurosci. *130*, 406–414.

Badrinarayan, A., Wescott, S.A., Vander Weele, C.M., Saunders, B.T., Couturier, B.E., Maren, S., and Aragona, B.J. (2012). Aversive stimuli differentially modulate real-time dopamine transmission dynamics within the nucleus accumbens core and shell. J. Neurosci. Off. J. Soc. Neurosci. *32*, 15779–15790.

Bandler, R., and Carrive, P. (1988). Integrated defence reaction elicited by excitatory amino acid microinjection in the midbrain periaqueductal grey region of the unrestrained cat. Brain Res. *439*, 95–106.

Bandler, R., and Depaulis, A. (1988). Elicitation of intraspecific defence reactions in the rat from midbrain periaqueductal grey by microinjection of kainic acid, without neurotoxic effects. Neurosci. Lett. *88*, 291–296.

Bandler, R., Prineas, S., and McCulloch, T. (1985a). Further localization of midbrain neurones mediating the defence reaction in the cat by microinjections of excitatory amino acids. Neurosci. Lett. *56*, 311–316.

Bandler, R., Depaulis, A., and Vergnes, M. (1985b). Identification of midbrain neurones mediating defensive behaviour in the rat by microinjections of excitatory amino acids. Behav. Brain Res. *15*, 107–119.

Bannon, M.J., and Roth, R.H. (1983). Pharmacology of mesocortical dopamine neurons. Pharmacol. Rev. *35*, 53–68.

Bannon, M.J., Michaud, R.L., and Roth, R.H. (1981). Mesocortical dopamine neurons. Lack of autoreceptors modulating dopamine synthesis. Mol. Pharmacol. *19*, 270–275.

Bassareo, V., Tanda, G., Petromilli, P., Giua, C., and Chiara, G.D. (1996). Non-psychostimulant drugs of abuse and anxiogenic drugs activate with differential selectivity dopamine transmission in the nucleus accumbens and in the medial prefrontal cortex of the rat. Psychopharmacology (Berl.) *124*, 293–299.

Bassareo, V., De Luca, M.A., and Di Chiara, G. (2002). Differential Expression of Motivational Stimulus Properties by Dopamine in Nucleus Accumbens Shell versus Core and Prefrontal Cortex. J. Neurosci. Off. J. Soc. Neurosci. *22*, 4709–4719.

Bechara, A., Damasio, A.R., Damasio, H., and Anderson, S.W. (1994). Insensitivity to future consequences following damage to human prefrontal cortex. Cognition *50*, 7–15.

Bechara, A., Tranel, D., and Damasio, H. (2000). Characterization of the decision-making deficit of patients with ventromedial prefrontal cortex lesions. Brain *123*, 2189–2202.

Bechara, A., Damasio, H., Tranel, D., and Damasio, A.R. (2005). The Iowa Gambling Task and the somatic marker hypothesis: some questions and answers. Trends Cogn. Sci. *9*, 159–162; discussion 162-164.

Berger, B., Thierry, A.M., Tassin, J.P., and Moyne, M.A. (1976). Dopaminergic innervation of the rat prefrontal cortex: a fluorescence histochemical study. Brain Res. *106*, 133–145.

Bergson, C., Mrzljak, L., Lidow, M.S., Goldman-Rakic, P.S., and Levenson, R. (1995a). Characterization of subtype-specific antibodies to the human D5 dopamine receptor: studies in primate brain and transfected mammalian cells. Proc. Natl. Acad. Sci. U. S. A. *92*, 3468–3472.

Bergson, C., Mrzljak, L., Smiley, J.F., Pappy, M., Levenson, R., and Goldman-Rakic, P.S. (1995b). Regional, cellular, and subcellular variations in the distribution of D1 and D5 dopamine receptors in primate brain. J. Neurosci. Off. J. Soc. Neurosci. *15*, 7821–7836.

Berridge, K.C. (2007). The debate over dopamine's role in reward: the case for incentive salience. Psychopharmacology (Berl.) *191*, 391–431.

Berridge, K.C., and Robinson, T.E. (1998). What is the role of dopamine in reward: hedonic impact, reward learning, or incentive salience? Brain Res. Brain Res. Rev. *28*, 309–369.

Betley, J.N., Xu, S., Cao, Z.F.H., Gong, R., Magnus, C.J., Yu, Y., and Sternson, S.M. (2015). Neurons for hunger and thirst transmit a negative-valence teaching signal. Nature *521*, 180–185.

Beyeler, A., Namburi, P., Glober, G.F., Simonnet, C., Calhoon, G.G., Conyers, G.F., Luck, R., Wildes, C.P., and Tye, K.M. (2016). Divergent routing of positive and negative information from the amygdala during memory retrieval. Neuron *90*, 348–361.

Björklund, A., and Dunnett, S.B. (2007). Dopamine neuron systems in the brain: an update. Trends Neurosci. *30*, 194–202.

Botvinick, M.M., Cohen, J.D., and Carter, C.S. (2004). Conflict monitoring and anterior cingulate cortex: an update. Trends Cogn. Sci. *8*, 539–546.

Brady, A.M., and O'Donnell, P. (2004). Dopaminergic modulation of prefrontal cortical input to nucleus accumbens neurons in vivo. J. Neurosci. Off. J. Soc. Neurosci. *24*, 1040–1049.

Brandão, M.L., Zanoveli, J.M., Ruiz-Martinez, R.C., Oliveira, L.C., and Landeira-Fernandez, J. (2008). Different patterns of freezing behavior organized in the periaqueductal gray of rats: association with different types of anxiety. Behav. Brain Res. *188*, 1–13.

Brischoux, F., Chakraborty, S., Brierley, D.I., and Ungless, M.A. (2009). Phasic excitation of dopamine neurons in ventral VTA by noxious stimuli. Proc. Natl. Acad. Sci. *106*, 4894–4899.

Britt, J.P., Benaliouad, F., McDevitt, R.A., Stuber, G.D., Wise, R.A., and Bonci, A. (2012). Synaptic and behavioral profile of multiple glutamatergic inputs to the nucleus accumbens. Neuron *76*, 790–803.

Bromberg-Martin, E.S., Matsumoto, M., and Hikosaka, O. (2010). Dopamine in Motivational Control: Rewarding, Aversive, and Alerting. Neuron *68*, 815–834.

Brozoski, T.J., Brown, R.M., Rosvold, H.E., and Goldman, P.S. (1979). Cognitive deficit caused by regional depletion of dopamine in prefrontal cortex of rhesus monkey. Science *205*, 929–932.

Buchta, W.C., Mahler, S.V., Harlan, B., Aston-Jones, G.S., and Riegel, A.C. (2017). Dopamine terminals from the ventral tegmental area gate intrinsic inhibition in the prefrontal cortex. Physiol. Rep. *5*.

Budygin, E.A., Park, J., Bass, C.E., Grinevich, V.P., Bonin, K.D., and Wightman, R.M. (2012). Aversive stimulus differentially triggers subsecond dopamine release in reward regions. Neuroscience *201*, 331–337.

Buhle, J.T., Kober, H., Ochsner, K.N., Mende-Siedlecki, P., Weber, J., Hughes, B.L., Kross, E., Atlas, L.Y., McRae, K., and Wager, T.D. (2013). Common representation of pain and negative emotion in the midbrain periaqueductal gray. Soc. Cogn. Affect. Neurosci. *8*, 609–616.

Bunney, B.S., and Aghajanian, G.K. (1976). Dopamine and norepinephrine innervated cells in the rat prefrontal cortex: pharmacological differentiation using microiontophoretic techniques. Life Sci. *19*, 1783–1789.

Bunney, B.S., Chiodo, L.A., and Grace, A.A. (1991). Midbrain dopamine system electrophysiological functioning: a review and new hypothesis. Synap. N. Y. N *9*, 79–94.

Burgos-Robles, A., Vidal-Gonzalez, I., and Quirk, G.J. (2009). Sustained conditioned responses in prelimbic prefrontal neurons are correlated with fear expression and extinction failure. J. Neurosci. Off. J. Soc. Neurosci. *29*, 8474–8482.

Burgos-Robles, A., Bravo-Rivera, H., and Quirk, G.J. (2013). Prelimbic and infralimbic neurons signal distinct aspects of appetitive instrumental behavior. PloS One *8*, e57575.

Burgos-Robles, A., Kimchi, E.Y., Izadmehr, E.M., Porzenheim, M.J., Ramos-Guasp, W.A., Nieh, E.H., Felix-Ortiz, A.C., Namburi, P., Leppla, C.A., Presbrey, K.N., et al. (2017). Amygdala inputs to prefrontal cortex guide behavior amid conflicting cues of reward and punishment. Nat. Neurosci. *20*, 824–835.

Burton, M.J., Rolls, E.T., and Mora, F. (1976). Effects of hunger on the responses of neurons in the lateral hypothalamus to the sight and taste of food. Exp. Neurol. *51*, 668–677.

Cachope, R., and Cheer, J.F. (2014). Local control of striatal dopamine release. Front. Behav. Neurosci. *8*, 188.

Cachope, R., Mateo, Y., Mathur, B.N., Irving, J., Wang, H.-L., Morales, M., Lovinger, D.M., and Cheer, J.F. (2012). Selective activation of cholinergic interneurons enhances accumbal phasic dopamine release: setting the tone for reward processing. Cell Rep. *2*, 33–41.

Calhoon, G.G., and Tye, K.M. (2015). Resolving the neural circuits of anxiety. Nat. Neurosci. *18*, 1394–1404.

Calipari, E.S., Siciliano, C.A., Zimmer, B.A., and Jones, S.R. (2015). Brief intermittent cocaine self-administration and abstinence sensitizes cocaine effects on the dopamine transporter and increases drug seeking. Neuropsychopharmacol. Off. Publ. Am. Coll. Neuropsychopharmacol. *40*, 728–735.

Calipari, E.S., Bagot, R.C., Purushothaman, I., Davidson, T.J., Yorgason, J.T., Peña, C.J., Walker, D.M., Pirpinias, S.T., Guise, K.G., Ramakrishnan, C., et al. (2016). In vivo imaging identifies temporal signature of D1 and D2 medium spiny neurons in cocaine reward. Proc. Natl. Acad. Sci. U. S. A. *113*, 2726–2731.

Carr, D.B., O'Donnell, P., Card, J.P., and Sesack, S.R. (1999). Dopamine terminals in the rat prefrontal cortex synapse on pyramidal cells that project to the nucleus accumbens. J. Neurosci. Off. J. Soc. Neurosci. *19*, 11049–11060.

Carrive, P., Dampney, R.A., and Bandler, R. (1987). Excitation of neurones in a restricted portion of the midbrain periaqueductal grey elicits both behavioural and cardiovascular components of the defence reaction in the unanaesthetised decerebrate cat. Neurosci. Lett. *81*, 273–278.

Cass, W.A., and Gerhardt, G.A. (1995). In vivo assessment of dopamine uptake in rat medial prefrontal cortex: comparison with dorsal striatum and nucleus accumbens. J. Neurochem. *65*, 201–207.

Castro, D.C., and Berridge, K.C. (2014). Opioid hedonic hotspot in nucleus accumbens shell: mu, delta, and kappa maps for enhancement of sweetness "liking" and "wanting." J. Neurosci. Off. J. Soc. Neurosci. *34*, 4239–4250.

Chen, T.-W., Wardill, T.J., Sun, Y., Pulver, S.R., Renninger, S.L., Baohan, A., Schreiter, E.R., Kerr, R.A., Orger, M.B., Jayaraman, V., et al. (2013). Ultrasensitive fluorescent proteins for imaging neuronal activity. Nature *499*, 295–300.

Chiodo, L.A., Bannon, M.J., Grace, A.A., Roth, R.H., and Bunney, B.S. (1984). Evidence for the absence of impulse-regulating somatodendritic and synthesis-modulating nerve terminal autoreceptors on subpopulations of mesocortical dopamine neurons. Neuroscience *12*, 1–16.

Chudasama, Y., and Robbins, T.W. (2004). Dopaminergic modulation of visual attention and working memory in the rodent prefrontal cortex. Neuropsychopharmacol. Off. Publ. Am. Coll. Neuropsychopharmacol. *29*, 1628–1636.

Clarkson, R.L., Liptak, A.T., Gee, S.M., Sohal, V.S., and Bender, K.J. (2017). D3 Receptors Regulate Excitability in a Unique Class of Prefrontal Pyramidal Cells. J. Neurosci. Off. J. Soc. Neurosci. *37*, 5846–5860.

Cohen, J.D., and Servan-Schreiber, D. (1992). Context, cortex, and dopamine: A connectionist approach to behavior and biology in schizophrenia. Psychol. Rev. *99*, 45–77.

Cohen, J.D., Braver, T.S., and Brown, J.W. (2002). Computational perspectives on dopamine function in prefrontal cortex. Curr. Opin. Neurobiol. *12*, 223–229.

Cohen, J.Y., Haesler, S., Vong, L., Lowell, B.B., and Uchida, N. (2012). Neuron-type-specific signals for reward and punishment in the ventral tegmental area. Nature *482*, 85–88.

Cragg, S.J., and Rice, M.E. (2004). DAncing past the DAT at a DA synapse. Trends Neurosci. *27*, 270–277.

Creese, I., Burt, D.R., and Snyder, S.H. (1976). Dopamine receptor binding predicts clinical and pharmacological potencies of antischizophrenic drugs. Science *192*, 481–483.

Day, J.J., Roitman, M.F., Wightman, R.M., and Carelli, R.M. (2007). Associative learning mediates dynamic shifts in dopamine signaling in the nucleus accumbens. Nat. Neurosci. *10*, 1020–1028.

De Boer, S.F., and Koolhaas, J.M. (2003). Defensive burying in rodents: ethology, neurobiology and psychopharmacology. Eur. J. Pharmacol. *463*, 145–161.

DeFelipe, J., and Fariñas, I. (1992). The pyramidal neuron of the cerebral cortex: morphological and chemical characteristics of the synaptic inputs. Prog. Neurobiol. *39*, 563–607.

Deng, H., Xiao, X., and Wang, Z. (2016). Periaqueductal Gray Neuronal Activities Underlie Different Aspects of Defensive Behaviors. J. Neurosci. Off. J. Soc. Neurosci. *36*, 7580–7588.

Deroche, V., Le Moal, M., and Piazza, P.V. (1999). Cocaine self-administration increases the incentive motivational properties of the drug in rats. Eur. J. Neurosci. *11*, 2731–2736.

Descarries, L., Lemay, B., Doucet, G., and Berger, B. (1987). Regional and laminar density of the dopamine innervation in adult rat cerebral cortex. Neuroscience *21*, 807–824.

Di Chiara, G., Loddo, P., and Tanda, G. (1999). Reciprocal changes in prefrontal and limbic dopamine responsiveness to aversive and rewarding stimuli after chronic mild stress: implications for the psychobiology of depression. Biol. Psychiatry *46*, 1624–1633.

Dias, R., Robbins, T.W., and Roberts, A.C. (1996a). Dissociation in prefrontal cortex of affective and attentional shifts. Nature *380*, 69–72.

Dias, R., Robbins, T.W., and Roberts, A.C. (1996b). Primate analogue of the Wisconsin Card Sorting Test: effects of excitotoxic lesions of the prefrontal cortex in the marmoset. Behav. Neurosci. *110*, 872–886.

Dias, R., Robbins, T.W., and Roberts, A.C. (1997). Dissociable forms of inhibitory control within prefrontal cortex with an analog of the Wisconsin Card Sort Test: restriction to novel situations and independence from "on-line" processing. J. Neurosci. Off. J. Soc. Neurosci. *17*, 9285–9297.

Douglas, R.J., and Martin, K.A.C. (2004). Neuronal circuits of the neocortex. Annu. Rev. Neurosci. *27*, 419–451.

Dreyer, J.K., and Hounsgaard, J. (2013). Mathematical model of dopamine autoreceptors and uptake inhibitors and their influence on tonic and phasic dopamine signaling. J. Neurophysiol. *109*, 171–182.

Dreyer, J.K., Herrik, K.F., Berg, R.W., and Hounsgaard, J.D. (2010). Influence of phasic and tonic dopamine release on receptor activation. J. Neurosci. Off. J. Soc. Neurosci. *30*, 14273–14283.

Dreyer, J.K., Vander Weele, C.M., Lovic, V., and Aragona, B.J. (2016). Functionally Distinct Dopamine Signals in Nucleus Accumbens Core and Shell in the Freely Moving Rat. J. Neurosci. Off. J. Soc. Neurosci. *36*, 98–112.

Dubuisson, D., and Dennis, S.G. (1977). The formalin test: a quantitative study of the analgesic effects of morphine, meperidine, and brain stem stimulation in rats and cats. Pain *4*, 161–174.

Dunbar, R.I.M. (2009). The social brain hypothesis and its implications for social evolution. Ann. Hum. Biol. *36*, 562–572.

Durstewitz, D., and Seamans, J.K. (2008). The dual-state theory of prefrontal cortex dopamine function with relevance to catechol-o-methyltransferase genotypes and schizophrenia. Biol. Psychiatry *64*, 739–749.

Ellwood, I.T., Patel, T., Wadia, V., Lee, A.T., Liptak, A.T., Bender, K.J., and Sohal, V.S. (2017). Tonic or Phasic Stimulation of Dopaminergic Projections to Prefrontal Cortex Causes Mice to Maintain or Deviate from Previously Learned Behavioral Strategies. J. Neurosci. Off. J. Soc. Neurosci. *37*, 8315–8329.

Espejo, E.F. (1997). Selective dopamine depletion within the medial prefrontal cortex induces anxiogenic-like effects in rats placed on the elevated plus maze. Brain Res. *762*, 281–284.

Euston, D.R., Gruber, A.J., and McNaughton, B.L. (2012). The role of medial prefrontal cortex in memory and decision making. Neuron *76*, 1057–1070.

Fallon, J.H. (1981). Collateralization of monoamine neurons: mesotelencephalic dopamine projections to caudate, septum, and frontal cortex. J. Neurosci. Off. J. Soc. Neurosci. *1*, 1361–1368.

Fanselow, M.S. (1991). The Midbrain Periaqueductal Gray as a Coordinator of Action in Response to Fear and Anxiety. In The Midbrain Periaqueductal Gray Matter, (Springer, Boston, MA), pp. 151–173.

Fields, H.L., Hjelmstad, G.O., Margolis, E.B., and Nicola, S.M. (2007). Ventral tegmental area neurons in learned appetitive behavior and positive reinforcement. Annu. Rev. Neurosci. *30*, 289–316.

Finlay, J.M., Zigmond, M.J., and Abercrombie, E.D. (1995). Increased dopamine and norepinephrine release in medial prefrontal cortex induced by acute and chronic stress: effects of diazepam. Neuroscience *64*, 619–628.

Franklin, T.B., Silva, B.A., Perova, Z., Marrone, L., Masferrer, M.E., Zhan, Y., Kaplan, A., Greetham, L., Verrechia, V., Halman, A., et al. (2016). Prefrontal cortical control of a brainstem social behavior circuit. BioRxiv 073734.

Gabbott, P.L., Dickie, B.G., Vaid, R.R., Headlam, A.J., and Bacon, S.J. (1997). Local-circuit neurones in the medial prefrontal cortex (areas 25, 32 and 24b) in the rat: morphology and quantitative distribution. J. Comp. Neurol. *377*, 465–499.

Gabbott, P.L.A., Warner, T.A., Jays, P.R.L., Salway, P., and Busby, S.J. (2005). Prefrontal cortex in the rat: projections to subcortical autonomic, motor, and limbic centers. J. Comp. Neurol. *492*, 145–177.

Gao, W.J., Krimer, L.S., and Goldman-Rakic, P.S. (2001). Presynaptic regulation of recurrent excitation by D1 receptors in prefrontal circuits. Proc. Natl. Acad. Sci. U. S. A. *98*, 295–300.

Garris, P.A., and Wightman, R.M. (1994). Different kinetics govern dopaminergic transmission in the amygdala, prefrontal cortex, and striatum: an in vivo voltammetric study. J. Neurosci. *14*, 442–450.

Garris, P.A., Collins, L.B., Jones, S.R., and Wightman, R.M. (1993). Evoked extracellular dopamine in vivo in the medial prefrontal cortex. J. Neurochem. *61*, 637–647.

Gaspar, P., Bloch, B., and Le Moine, C. (1995). D1 and D2 receptor gene expression in the rat frontal cortex: cellular localization in different classes of efferent neurons. Eur. J. Neurosci. *7*, 1050–1063.

Gee, S., Ellwood, I., Patel, T., Luongo, F., Deisseroth, K., and Sohal, V.S. (2012). Synaptic activity unmasks dopamine D2 receptor modulation of a specific class of layer V pyramidal neurons in prefrontal cortex. J. Neurosci. Off. J. Soc. Neurosci. *32*, 4959–4971.

Ghosh, K.K., Burns, L.D., Cocker, E.D., Nimmerjahn, A., Ziv, Y., Gamal, A.E., and Schnitzer, M.J. (2011). Miniaturized integration of a fluorescence microscope. Nat. Methods *8*, 871–878.

Goldman-Rakic, P.S., and Selemon, L.D. (1997). Functional and anatomical aspects of prefrontal pathology in schizophrenia. Schizophr. Bull. *23*, 437–458.

Goldman-Rakic, P.S., Leranth, C., Williams, S.M., Mons, N., and Geffard, M. (1989). Dopamine synaptic complex with pyramidal neurons in primate cerebral cortex. Proc. Natl. Acad. Sci. U. S. A. *86*, 9015–9019.

González-Burgos, G., Kröner, S., Krimer, L.S., Seamans, J.K., Urban, N.N., Henze, D.A., Lewis, D.A., and Barrionuevo, G. (2002). Dopamine modulation of neuronal function in the monkey prefrontal cortex. Physiol. Behav. *77*, 537–543.

Gorelova, N.A., and Yang, C.R. (2000). Dopamine D1/D5 receptor activation modulates a persistent sodium current in rat prefrontal cortical neurons in vitro. J. Neurophysiol. *84*, 75–87.

Grace, A.A., and Bunney, B.S. (1984). The control of firing pattern in nigral dopamine neurons: single spike firing. J. Neurosci. Off. J. Soc. Neurosci. *4*, 2866–2876.

Grace, A.A., Floresco, S.B., Goto, Y., and Lodge, D.J. (2007). Regulation of firing of dopaminergic neurons and control of goal-directed behaviors. Trends Neurosci. *30*, 220–227.

Granon, S., Passetti, F., Thomas, K.L., Dalley, J.W., Everitt, B.J., and Robbins, T.W. (2000). Enhanced and impaired attentional performance after infusion of D1 dopaminergic receptor agents into rat prefrontal cortex. J. Neurosci. Off. J. Soc. Neurosci. *20*, 1208–1215.

Gregoriou, G.G., Rossi, A.F., Ungerleider, L.G., and Desimone, R. (2014). Lesions of prefrontal cortex reduce attentional modulation of neuronal responses and synchrony in V4. Nat. Neurosci. *17*, 1003–1011.

Groenewegen, H.J., Wright, C.I., and Uylings, H.B. (1997). The anatomical relationships of the prefrontal cortex with limbic structures and the basal ganglia. J. Psychopharmacol. Oxf. Engl. *11*, 99–106.

Gulledge, A.T., and Jaffe, D.B. (1998). Dopamine decreases the excitability of layer V pyramidal cells in the rat prefrontal cortex. J. Neurosci. Off. J. Soc. Neurosci. *18*, 9139–9151.

Gulledge, A.T., and Jaffe, D.B. (2001). Multiple effects of dopamine on layer V pyramidal cell excitability in rat prefrontal cortex. J. Neurophysiol. *86*, 586–595.

Gunaydin, L.A., Grosenick, L., Finkelstein, J.C., Kauvar, I.V., Fenno, L.E., Adhikari, A., Lammel, S., Mirzabekov, J.J., Airan, R.D., Zalocusky, K.A., et al. (2014). Natural neural projection dynamics underlying social behavior. Cell *157*, 1535–1551.

Haber, S.N., and Fudge, J.L. (1997). The primate substantia nigra and VTA: integrative circuitry and function. Crit. Rev. Neurobiol. *11*, 323–342.

Halladay, L.R., and Blair, H.T. (2015). Distinct ensembles of medial prefrontal cortex neurons are activated by threatening stimuli that elicit excitation vs. inhibition of movement. J. Neurophysiol. *114*, 793–807.

Hamid, A.A., Pettibone, J.R., Mabrouk, O.S., Hetrick, V.L., Schmidt, R., Vander Weele, C.M., Kennedy, R.T., Aragona, B.J., and Berke, J.D. (2016). Mesolimbic dopamine signals the value of work. Nat. Neurosci. *19*, 117–126.

Han, S.-W., Kim, Y.-C., and Narayanan, N.S. (2017). Projection targets of medial frontal D1DR-expressing neurons. Neurosci. Lett. *655*, 166–171.

Heidbreder, C.A., and Groenewegen, H.J. (2003). The medial prefrontal cortex in the rat: evidence for a dorso-ventral distinction based upon functional and anatomical characteristics. Neurosci. Biobehav. Rev. *27*, 555–579.

Heien, M.L.A.V., Phillips, P.E.M., Stuber, G.D., Seipel, A.T., and Wightman, R.M. (2003). Overoxidation of carbon-fiber microelectrodes enhances dopamine adsorption and increases sensitivity. The Analyst *128*, 1413–1419.

Heimer, L., Alheid, G.F., de Olmos, J.S., Groenewegen, H.J., Haber, S.N., Harlan, R.E., and Zahm, D.S. (1997). The accumbens: beyond the core-shell dichotomy. J. Neuropsychiatry Clin. Neurosci. *9*, 354–381.

Henze, D.A., González-Burgos, G.R., Urban, N.N., Lewis, D.A., and Barrionuevo, G. (2000). Dopamine increases excitability of pyramidal neurons in primate prefrontal cortex. J. Neurophysiol. *84*, 2799–2809.

Hoover, W.B., and Vertes, R.P. (2007). Anatomical analysis of afferent projections to the medial prefrontal cortex in the rat. Brain Struct. Funct. *212*, 149–179.

Horvitz, J.C. (2000). Mesolimbocortical and nigrostriatal dopamine responses to salient non-reward events. Neuroscience *96*, 651–656.

Howes, O.D., and Kapur, S. (2009). The dopamine hypothesis of schizophrenia: version III--the final common pathway. Schizophr. Bull. *35*, 549–562.

Ikemoto, S. (2007). Dopamine reward circuitry: two projection systems from the ventral midbrain to the nucleus accumbens-olfactory tubercle complex. Brain Res. Rev. *56*, 27–78.

Jenck, F., Moreau, J.L., and Martin, J.R. (1995). Dorsal periaqueductal gray-induced aversion as a simulation of panic anxiety: elements of face and predictive validity. Psychiatry Res. *57*, 181–191.

Jennings, J.H., Ung, R.L., Resendez, S.L., Stamatakis, A.M., Taylor, J.G., Huang, J., Veleta, K., Kantak, P.A., Aita, M., Shilling-Scrivo, K., et al. (2015). Visualizing hypothalamic network dynamics for appetitive and consummatory behaviors. Cell *160*, 516–527.

Jensen, J., Willeit, M., Zipursky, R.B., Savina, I., Smith, A.J., Menon, M., Crawley, A.P., and Kapur, S. (2008). The formation of abnormal associations in schizophrenia: neural and behavioral evidence. Neuropsychopharmacol. Off. Publ. Am. Coll. Neuropsychopharmacol. *33*, 473–479.

Käenmäki, M., Tammimäki, A., Myöhänen, T., Pakarinen, K., Amberg, C., Karayiorgou, M., Gogos, J.A., and Männistö, P.T. (2010). Quantitative role of COMT in dopamine clearance in the prefrontal cortex of freely moving mice. J. Neurochem. *114*, 1745–1755.

Keithley, R.B., and Wightman, R.M. (2011). Assessing Principal Component Regression Prediction of Neurochemicals Detected with Fast-Scan Cyclic Voltammetry. ACS Chem. Neurosci. *2*, 514–525.

Keithley, R.B., Mark Wightman, R., and Heien, M.L. (2009). Multivariate concentration determination using principal component regression with residual analysis. TrAC Trends Anal. Chem. *28*, 1127–1136.

Kerney, M., Smaers, J.B., Schoenemann, P.T., and Dunn, J.C. (2017). The coevolution of play and the cortico-cerebellar system in primates. Primates J. Primatol. *58*, 485–491.

Kim, C.K., Yang, S.J., Pichamoorthy, N., Young, N.P., Kauvar, I., Jennings, J.H., Lerner, T.N., Berndt, A., Lee, S.Y., Ramakrishnan, C., et al. (2016). Simultaneous fast measurement of circuit dynamics at multiple sites across the mammalian brain. Nat. Methods *13*, 325–328.

Kim, C.K., Ye, L., Jennings, J.H., Pichamoorthy, N., Tang, D.D., Yoo, A.-C.W., Ramakrishnan, C., and Deisseroth, K. (2017). Molecular and Circuit-Dynamical Identification of Top-Down Neural Mechanisms for Restraint of Reward Seeking. Cell *170*, 1013-1027.e14.

Klapoetke, N.C., Murata, Y., Kim, S.S., Pulver, S.R., Birdsey-Benson, A., Cho, Y.K., Morimoto, T.K., Chuong, A.S., Carpenter, E.J., Tian, Z., et al. (2014). Independent optical excitation of distinct neural populations. Nat. Methods *11*, 338–346.

Kritzer, M.F., and Goldman-Rakic, P.S. (1995). Intrinsic circuit organization of the major layers and sublayers of the dorsolateral prefrontal cortex in the rhesus monkey. J. Comp. Neurol. *359*, 131–143.

Kroener, S., Chandler, L.J., Phillips, P.E.M., and Seamans, J.K. (2009). Dopamine modulates persistent synaptic activity and enhances the signal-to-noise ratio in the prefrontal cortex. PloS One *4*, e6507.

Lammel, S., Hetzel, A., Häckel, O., Jones, I., Liss, B., and Roeper, J. (2008). Unique properties of mesoprefrontal neurons within a dual mesocorticolimbic dopamine system. Neuron *57*, 760–773.

Lammel, S., Ion, D.I., Roeper, J., and Malenka, R.C. (2011). Projection-specific modulation of dopamine neuron synapses by aversive and rewarding stimuli. Neuron *70*, 855–862.

Lammel, S., Lim, B.K., Ran, C., Huang, K.W., Betley, M.J., Tye, K.M., Deisseroth, K., and Malenka, R.C. (2012). Input-specific control of reward and aversion in the ventral tegmental area. Nature *491*, 212–217.

Lauzon, N.M., and Laviolette, S.R. (2010). Dopamine D4-receptor modulation of cortical neuronal network activity and emotional processing: Implications for neuropsychiatric disorders. Behav. Brain Res. *208*, 12–22.

Laviolette, S.R., Lipski, W.J., and Grace, A.A. (2005). A subpopulation of neurons in the medial prefrontal cortex encodes emotional learning with burst and frequency codes through a dopamine D4 receptor-dependent basolateral amygdala input. J. Neurosci. Off. J. Soc. Neurosci. *25*, 6066–6075.

Lee, A.T., Vogt, D., Rubenstein, J.L., and Sohal, V.S. (2014a). A class of GABAergic neurons in the prefrontal cortex sends long-range projections to the nucleus accumbens and elicits acute avoidance behavior. J. Neurosci. Off. J. Soc. Neurosci. *34*, 11519–11525.

Lee, A.T., Gee, S.M., Vogt, D., Patel, T., Rubenstein, J.L., and Sohal, V.S. (2014b). Pyramidal neurons in prefrontal cortex receive subtype-specific forms of excitation and inhibition. Neuron *81*, 61–68.

Lidow, M.S., Goldman-Rakic, P.S., Gallager, D.W., and Rakic, P. (1991). Distribution of dopaminergic receptors in the primate cerebral cortex: quantitative autoradiographic analysis using [3H]raclopride, [3H]spiperone and [3H]SCH23390. Neuroscience *40*, 657–671.

Lindquist, M.A., Spicer, J., Asllani, I., and Wager, T.D. (2012). Estimating and testing variance components in a multi-level GLM. NeuroImage *59*, 490–501.

Mansouri, F.A., Tanaka, K., and Buckley, M.J. (2009). Conflict-induced behavioural adjustment: a clue to the executive functions of the prefrontal cortex. Nat. Rev. Neurosci. *10*, 141–152.

Mantz, J., Thierry, A.M., and Glowinski, J. (1989). Effect of noxious tail pinch on the discharge rate of mesocortical and mesolimbic dopamine neurons: selective activation of the mesocortical system. Brain Res. *476*, 377–381.

Matsumoto, M., and Hikosaka, O. (2009). Two types of dopamine neuron distinctly convey positive and negative motivational signals. Nature *459*, 837–841.

Matthews, G.A., Nieh, E.H., Vander Weele, C.M., Halbert, S.A., Pradhan, R.V., Yosafat, A.S., Glober, G.F., Izadmehr, E.M., Thomas, R.E., Lacy, G.D., et al. (2016). Dorsal Raphe Dopamine Neurons Represent the Experience of Social Isolation. Cell *164*, 617–631.

McCutcheon, J.E., Ebner, S.R., Loriaux, A.L., and Roitman, M.F. (2012). Encoding of aversion by dopamine and the nucleus accumbens. Front. Neurosci. *6*, 137.

Meyer, C.T., Padmala, S., and Pessoa, L. (2017). Tracking dynamic threat imminence. BioRxiv 183798.

Michel, P.P., Hirsch, E.C., and Hunot, S. (2016). Understanding Dopaminergic Cell Death Pathways in Parkinson Disease. Neuron *90*, 675–691.

Milham, M.P., Banich, M.T., Webb, A., Barad, V., Cohen, N.J., Wszalek, T., and Kramer, A.F. (2001). The relative involvement of anterior cingulate and prefrontal cortex in attentional control depends on nature of conflict. Brain Res. Cogn. Brain Res. *12*, 467–473.

Miller, E.K., and Cohen, J.D. (2001). An Integrative Theory of Prefrontal Cortex Function. Annu. Rev. Neurosci. *24*, 167–202.

Milner, B. (1963). Effects of Different Brain Lesions on Card Sorting: The Role of the Frontal Lobes. Arch. Neurol. *9*, 90–100.

Mizoguchi, K., Yuzurihara, M., Ishige, A., Sasaki, H., Chui, D.H., and Tabira, T. (2000). Chronic stress induces impairment of spatial working memory because of prefrontal dopaminergic dysfunction. J. Neurosci. Off. J. Soc. Neurosci. *20*, 1568–1574.

Mobbs, D., Petrovic, P., Marchant, J.L., Hassabis, D., Weiskopf, N., Seymour, B., Dolan, R.J., and Frith, C.D. (2007). When fear is near: threat imminence elicits prefrontal-periaqueductal gray shifts in humans. Science *317*, 1079–1083.

Mobbs, D., Yu, R., Rowe, J.B., Eich, H., FeldmanHall, O., and Dalgleish, T. (2010). Neural activity associated with monitoring the oscillating threat value of a tarantula. Proc. Natl. Acad. Sci. U. S. A. *107*, 20582–20586.

Muly, E.C., Szigeti, K., and Goldman-Rakic, P.S. (1998). D1 receptor in interneurons of macaque prefrontal cortex: distribution and subcellular localization. J. Neurosci. Off. J. Soc. Neurosci. *18*, 10553–10565.

Murugan, M., Jang, H.J., Park, M., Miller, E.M., Cox, J., Taliaferro, J.P., Parker, N.F., Bhave, V., Hur, H., Liang, Y., et al. (2017). Combined Social and Spatial Coding in a Descending Projection from the Prefrontal Cortex. Cell *171*, 1663-1677.e16.

Nakajima, S., Gerretsen, P., Takeuchi, H., Caravaggio, F., Chow, T., Le Foll, B., Mulsant, B., Pollock, B., and Graff-Guerrero, A. (2013). The potential role of dopamine D_3 receptor neurotransmission in cognition. Eur. Neuropsychopharmacol. J. Eur. Coll. Neuropsychopharmacol. *23*, 799–813.

Nieh, E.H., Matthews, G.A., Allsop, S.A., Presbrey, K.N., Leppla, C.A., Wichmann, R., Neve, R., Wildes, C.P., and Tye, K.M. (2015). Decoding neural circuits that control compulsive sucrose seeking. Cell *160*, 528–541.

Nieh, E.H., Vander Weele, C.M., Matthews, G.A., Presbrey, K.N., Wichmann, R., Leppla, C.A., Izadmehr, E.M., and Tye, K.M. (2016). Inhibitory Input from the Lateral Hypothalamus to the Ventral Tegmental Area Disinhibits Dopamine Neurons and Promotes Behavioral Activation. Neuron *90*, 1286–1298.

Niv, Y. (2007). Cost, benefit, tonic, phasic: what do response rates tell us about dopamine and motivation? Ann. N. Y. Acad. Sci. *1104*, 357–376.

Nolan, K.A., Bilder, R.M., Lachman, H.M., and Volavka, J. (2004). Catechol O-methyltransferase Val158Met polymorphism in schizophrenia: differential effects of Val and Met alleles on cognitive stability and flexibility. Am. J. Psychiatry *161*, 359–361.

Nomikos, G.G., and Spyraki, C. (1988). Cocaine-induced place conditioning: importance of route of administration and other procedural variables. Psychopharmacology (Berl.) *94*, 119–125.

Noonan, M.P., Mars, R.B., Sallet, J., Dunbar, R.I.M., and Fellows, L.K. (2018). The structural and functional brain networks that support human social networks. Behav. Brain Res.

Noudoost, B., and Moore, T. (2011). Control of visual cortical signals by prefrontal dopamine. Nature *474*, 372–375.

Okubo, Y., Suhara, T., Suzuki, K., Kobayashi, K., Inoue, O., Terasaki, O., Someya, Y., Sassa, T., Sudo, Y., Matsushima, E., et al. (1997a). Decreased prefrontal dopamine D1 receptors in schizophrenia revealed by PET. Nature *385*, 634–636.

Okubo, Y., Suhara, T., Sudo, Y., and Toru, M. (1997b). Possible role of dopamine D1 receptors in schizophrenia. Mol. Psychiatry *2*, 291–292.

Otis, J.M., Namboodiri, V.M.K., Matan, A.M., Voets, E.S., Mohorn, E.P., Kosyk, O., McHenry, J.A., Robinson, J.E., Resendez, S.L., Rossi, M.A., et al. (2017). Prefrontal cortex output circuits guide reward seeking through divergent cue encoding. Nature *543*, 103–107.

Paspalas, C.D., and Goldman-Rakic, P.S. (2005). Presynaptic D1 dopamine receptors in primate prefrontal cortex: target-specific expression in the glutamatergic synapse. J. Neurosci. Off. J. Soc. Neurosci. *25*, 1260–1267.

Penit-Soria, J., Audinat, E., and Crepel, F. (1987). Excitation of rat prefrontal cortical neurons by dopamine: an in vitro electrophysiological study. Brain Res. *425*, 263–274.

Phillips, P.E.M., Stuber, G.D., Heien, M.L.A.V., Wightman, R.M., and Carelli, R.M. (2003). Subsecond dopamine release promotes cocaine seeking. Nature *422*, 614–618.

Pnevmatikakis, E.A., Soudry, D., Gao, Y., Machado, T.A., Merel, J., Pfau, D., Reardon, T., Mu, Y., Lacefield, C., Yang, W., et al. (2016). Simultaneous Denoising, Deconvolution, and Demixing of Calcium Imaging Data. Neuron *89*, 285–299.

Popescu, A.T., Zhou, M.R., and Poo, M.-M. (2016). Phasic dopamine release in the medial prefrontal cortex enhances stimulus discrimination. Proc. Natl. Acad. Sci. U. S. A. *113*, E3169-3176.

Resendez, S.L., Jennings, J.H., Ung, R.L., Namboodiri, V.M.K., Zhou, Z.C., Otis, J.M., Nomura, H., McHenry, J.A., Kosyk, O., and Stuber, G.D. (2016). Visualization of cortical, subcortical and deep brain neural circuit dynamics during naturalistic mammalian behavior with head-mounted microscopes and chronically implanted lenses. Nat. Protoc. *11*, 566–597.

Rice, M.E., and Cragg, S.J. (2004). Nicotine amplifies reward-related dopamine signals in striatum. Nat. Neurosci. *7*, 583–584.

Ridderinkhof, K.R., van den Wildenberg, W.P.M., Segalowitz, S.J., and Carter, C.S. (2004). Neurocognitive mechanisms of cognitive control: The role of prefrontal cortex in action selection, response inhibition, performance monitoring, and reward-based learning. Brain Cogn. *56*, 129–140.

Roberts, D.C., Corcoran, M.E., and Fibiger, H.C. (1977). On the role of ascending catecholaminergic systems in intravenous self-administration of cocaine. Pharmacol. Biochem. Behav. *6*, 615–620.

Robinson, D.L., Venton, B.J., Heien, M.L.A.V., and Wightman, R.M. (2003). Detecting Subsecond Dopamine Release with Fast-Scan Cyclic Voltammetry in Vivo. Clin. Chem. *49*, 1763–1773.

Roeper, J. (2013). Dissecting the diversity of midbrain dopamine neurons. Trends Neurosci. *36*, 336–342.

Roitman, M.F., Stuber, G.D., Phillips, P.E.M., Wightman, R.M., and Carelli, R.M. (2004). Dopamine operates as a subsecond modulator of food seeking. J. Neurosci. Off. J. Soc. Neurosci. *24*, 1265–1271.

Roitman, M.F., Wheeler, R.A., Wightman, R.M., and Carelli, R.M. (2008). Real-time chemical responses in the nucleus accumbens differentiate rewarding and aversive stimuli. Nat. Neurosci. *11*, 1376–1377.

Rolls, E.T., Loh, M., Deco, G., and Winterer, G. (2008). Computational models of schizophrenia and dopamine modulation in the prefrontal cortex. Nat. Rev. Neurosci. *9*, 696–709.

Romanski, L.M., Bates, J.F., and Goldman-Rakic, P.S. (1999a). Auditory belt and parabelt projections to the prefrontal cortex in the rhesus monkey. J. Comp. Neurol. *403*, 141–157.

Romanski, L.M., Tian, B., Fritz, J., Mishkin, M., Goldman-Rakic, P.S., and Rauschecker, J.P. (1999b). Dual streams of auditory afferents target multiple domains in the primate prefrontal cortex. Nat. Neurosci. *2*, 1131–1136.

Rossi, A.F., Bichot, N.P., Desimone, R., and Ungerleider, L.G. (2007). Top down attentional deficits in macaques with lesions of lateral prefrontal cortex. J. Neurosci. Off. J. Soc. Neurosci. *27*, 11306–11314.

Salamone, J.D., and Correa, M. (2012). The mysterious motivational functions of mesolimbic dopamine. Neuron *76*, 470–485.

Salamone, J.D., and Correa, M. (2018). Parsing the Role of Mesolimbic Dopamine in Specific Aspects of Motivation: Behavioral Activation, Invigoration, and Effort-Based Decision Making. In Advances in Motivation Science, (Elsevier), p.

Salamone, J.D., Correa, M., Farrar, A., and Mingote, S.M. (2007). Effort-related functions of nucleus accumbens dopamine and associated forebrain circuits. Psychopharmacology (Berl.) *191*, 461–482.

Sangha, S., Robinson, P.D., Greba, Q., Davies, D.A., and Howland, J.G. (2014). Alterations in reward, fear and safety cue discrimination after inactivation of the rat prelimbic and infralimbic cortices. Neuropsychopharmacol. Off. Publ. Am. Coll. Neuropsychopharmacol. *39*, 2405–2413.

Santana, N., and Artigas, F. (2017). Laminar and Cellular Distribution of Monoamine Receptors in Rat Medial Prefrontal Cortex. Front. Neuroanat. *11*, 87.

Santana, N., Mengod, G., and Artigas, F. (2009). Quantitative analysis of the expression of dopamine D1 and D2 receptors in pyramidal and GABAergic neurons of the rat prefrontal cortex. Cereb. Cortex N. Y. N 1991 *19*, 849–860.

Satpute, A.B., Wager, T.D., Cohen-Adad, J., Bianciardi, M., Choi, J.-K., Buhle, J.T., Wald, L.L., and Barrett, L.F. (2013). Identification of discrete functional subregions of the human periaqueductal gray. Proc. Natl. Acad. Sci. U. S. A. *110*, 17101–17106.

Sawaguchi, T., and Goldman-Rakic, P.S. (1991). D1 dopamine receptors in prefrontal cortex: involvement in working memory. Science *251*, 947–950.

Schultz, W. (2013). Updating dopamine reward signals. Curr. Opin. Neurobiol. *23*, 229–238.

Schultz, W., Dayan, P., and Montague, P.R. (1997). A Neural Substrate of Prediction and Reward. Science *275*, 1593–1599.

Schultz, W., Stauffer, W.R., and Lak, A. (2017). The phasic dopamine signal maturing: from reward via behavioural activation to formal economic utility. Curr. Opin. Neurobiol. *43*, 139–148.

Seamans, J.K., and Yang, C.R. (2004). The principal features and mechanisms of dopamine modulation in the prefrontal cortex. Prog. Neurobiol. *74*, 1–58.

Seamans, J.K., Gorelova, N., Durstewitz, D., and Yang, C.R. (2001a). Bidirectional dopamine modulation of GABAergic inhibition in prefrontal cortical pyramidal neurons. J. Neurosci. Off. J. Soc. Neurosci. *21*, 3628–3638.

Seamans, J.K., Durstewitz, D., Christie, B.R., Stevens, C.F., and Sejnowski, T.J. (2001b). Dopamine D1/D5 receptor modulation of excitatory synaptic inputs to layer V prefrontal cortex neurons. Proc. Natl. Acad. Sci. U. S. A. *98*, 301–306.

Séguéla, P., Watkins, K.C., and Descarries, L. (1988). Ultrastructural features of dopamine axon terminals in the anteromedial and the suprarhinal cortex of adult rat. Brain Res. *442*, 11–22.

Senn, V., Wolff, S.B.E., Herry, C., Grenier, F., Ehrlich, I., Gründemann, J., Fadok, J.P., Müller, C., Letzkus, J.J., and Lüthi, A. (2014). Long-range connectivity defines behavioral specificity of amygdala neurons. Neuron *81*, 428–437.

Seong, H.J., and Carter, A.G. (2012). D1 receptor modulation of action potential firing in a subpopulation of layer 5 pyramidal neurons in the prefrontal cortex. J. Neurosci. Off. J. Soc. Neurosci. *32*, 10516–10521.

Sesack, S.R., and Bunney, B.S. (1989). Pharmacological characterization of the receptor mediating electrophysiological responses to dopamine in the rat medial prefrontal cortex: a microiontophoretic study. J. Pharmacol. Exp. Ther. *248*, 1323–1333.

Sesack, S.R., Deutch, A.Y., Roth, R.H., and Bunney, B.S. (1989). Topographical organization of the efferent projections of the medial prefrontal cortex in the rat: an anterograde tract-tracing study with Phaseolus vulgaris leucoagglutinin. J. Comp. Neurol. *290*, 213–242.

Sesack, S.R., Hawrylak, V.A., Matus, C., Guido, M.A., and Levey, A.I. (1998). Dopamine axon varicosities in the prelimbic division of the rat prefrontal cortex exhibit sparse immunoreactivity for the dopamine transporter. J. Neurosci. Off. J. Soc. Neurosci. *18*, 2697–2708.

Shuen, J.A., Chen, M., Gloss, B., and Calakos, N. (2008). Drd1a-tdTomato BAC transgenic mice for simultaneous visualization of medium spiny neurons in the direct and indirect pathways of the basal ganglia. J. Neurosci. Off. J. Soc. Neurosci. *28*, 2681–2685.

Sierra-Mercado, D., Padilla-Coreano, N., and Quirk, G.J. (2011). Dissociable roles of prelimbic and infralimbic cortices, ventral hippocampus, and basolateral amygdala in the expression and extinction of conditioned fear. Neuropsychopharmacol. Off. Publ. Am. Coll. Neuropsychopharmacol. *36*, 529–538.

da Silva, J.A., Tecuapetla, F., Paixão, V., and Costa, R.M. (2018). Dopamine neuron activity before action initiation gates and invigorates future movements. Nature *554*, 244–248.

Sokolowski, J.D., McCullough, L.D., and Salamone, J.D. (1994). Effects of dopamine depletions in the medial prefrontal cortex on active avoidance and escape in the rat. Brain Res. *651*, 293–299.

St Onge, J.R., Ahn, S., Phillips, A.G., and Floresco, S.B. (2012). Dynamic fluctuations in dopamine efflux in the prefrontal cortex and nucleus accumbens during risk-based decision making. J. Neurosci. Off. J. Soc. Neurosci. *32*, 16880–16891.

Stuber, G.D., Hnasko, T.S., Britt, J.P., Edwards, R.H., and Bonci, A. (2010). Dopaminergic terminals in the nucleus accumbens but not the dorsal striatum corelease glutamate. J. Neurosci. Off. J. Soc. Neurosci. *30*, 8229–8233.

Stuber, G.D., Sparta, D.R., Stamatakis, A.M., van Leeuwen, W.A., Hardjoprajitno, J.E., Cho, S., Tye, K.M., Kempadoo, K.A., Zhang, F., Deisseroth, K., et al. (2011). Excitatory transmission from the amygdala to nucleus accumbens facilitates reward seeking. Nature *475*, 377–380.

Surmeier, D.J., Bargas, J., Hemmings, H.C., Nairn, A.C., and Greengard, P. (1995). Modulation of calcium currents by a D1 dopaminergic protein kinase/phosphatase cascade in rat neostriatal neurons. Neuron *14*, 385–397.

Tanda, G., Carboni, E., Frau, R., and Di Chiara, G. (1994). Increase of extracellular dopamine in the prefrontal cortex: a trait of drugs with antidepressant potential? Psychopharmacology (Berl.) *115*, 285–288.

Thierry, A.M., Tassin, J.P., Blanc, G., and Glowinski, J. (1976). Selective activation of mesocortical DA system by stress. Nature *263*, 242–244.

Tovote, P., Esposito, M.S., Botta, P., Chaudun, F., Fadok, J.P., Markovic, M., Wolff, S.B.E., Ramakrishnan, C., Fenno, L., Deisseroth, K., et al. (2016). Midbrain circuits for defensive behaviour. Nature *534*, 206–212.

Tritsch, N.X., and Sabatini, B.L. (2012). Dopaminergic modulation of synaptic transmission in cortex and striatum. Neuron *76*, 33–50.

Tritsch, N.X., Granger, A.J., and Sabatini, B.L. (2016). Mechanisms and functions of GABA co-release. Nat. Rev. Neurosci. *17*, 139–145.

Ungless, M.A., Magill, P.J., and Bolam, J.P. (2004). Uniform inhibition of dopamine neurons in the ventral tegmental area by aversive stimuli. Science *303*, 2040–2042.

Vander Weele, C.M., Porter-Stransky, K.A., Mabrouk, O.S., Lovic, V., Singer, B.F., Kennedy, R.T., and Aragona, B.J. (2014). Rapid dopamine transmission within the nucleus accumbens: dramatic difference between morphine and oxycodone delivery. Eur. J. Neurosci. *40*, 3041–3054.

Verney, C., Alvarez, C., Geffard, M., and Berger, B. (1990). Ultrastructural Double-Labelling Study of Dopamine Terminals and GABA-Containing Neurons in Rat Anteromedial Cerebral Cortex. Eur. J. Neurosci. *2*, 960–972.

Vertes, R.P. (2004). Differential projections of the infralimbic and prelimbic cortex in the rat. Synap. N. Y. N *51*, 32–58.

Vincent, S.L., Khan, Y., and Benes, F.M. (1993). Cellular distribution of dopamine D1 and D2 receptors in rat medial prefrontal cortex. J. Neurosci. Off. J. Soc. Neurosci. *13*, 2551–2564.

Volkow, N.D., Wise, R.A., and Baler, R. (2017). The dopamine motive system: implications for drug and food addiction. Nat. Rev. Neurosci. *18*, 741–752.

Weinberger, D.R., Berman, K.F., and Chase, T.N. (1988a). Mesocortical dopaminergic function and human cognition. Ann. N. Y. Acad. Sci. *537*, 330–338.

Weinberger, D.R., Berman, K.F., and Illowsky, B.P. (1988b). Physiological dysfunction of dorsolateral prefrontal cortex in schizophrenia. III. A new cohort and evidence for a monoaminergic mechanism. Arch. Gen. Psychiatry *45*, 609–615.

Wilkinson, L.S., Dias, R., Thomas, K.L., Augood, S.J., Everitt, B.J., Robbins, T.W., and Roberts, A.C. (1997). Contrasting effects of excitotoxic lesions of the prefrontal cortex on the behavioural response to D-amphetamine and presynaptic and postsynaptic measures of striatal dopamine function in monkeys. Neuroscience *80*, 717–730.

Williams, G.V., and Goldman-Rakic, P.S. (1995). Modulation of memory fields by dopamine D1 receptors in prefrontal cortex. Nature *376*, 572–575.

Winton-Brown, T.T., Fusar-Poli, P., Ungless, M.A., and Howes, O.D. (2014). Dopaminergic basis of salience dysregulation in psychosis. Trends Neurosci. *37*, 85–94.

Wise, R.A. (2006). Role of brain dopamine in food reward and reinforcement. Philos. Trans. R. Soc. Lond. B. Biol. Sci. *361*, 1149–1158.

Wise, R.A. (2008). Dopamine and reward: the anhedonia hypothesis 30 years on. Neurotox. Res. *14*, 169–183.

Witten, I.B., Steinberg, E.E., Lee, S.Y., Davidson, T.J., Zalocusky, K.A., Brodsky, M., Yizhar, O., Cho, S.L., Gong, S., Ramakrishnan, C., et al. (2011). Recombinase-driver rat lines: tools, techniques, and optogenetic application to dopamine-mediated reinforcement. Neuron *72*, 721–733.

Yang, C.R., and Seamans, J.K. (1996). Dopamine D1 receptor actions in layers V-VI rat prefrontal cortex neurons in vitro: modulation of dendritic-somatic signal integration. J. Neurosci. Off. J. Soc. Neurosci. *16*, 1922–1935.

Yang, C.R., Seamans, J.K., and Gorelova, N. (1996). Electrophysiological and morphological properties of layers V-VI principal pyramidal cells in rat prefrontal cortex in vitro. J. Neurosci. Off. J. Soc. Neurosci. *16*, 1904–1921.

Ye, L., Allen, W.E., Thompson, K.R., Tian, Q., Hsueh, B., Ramakrishnan, C., Wang, A.-C., Jennings, J.H., Adhikari, A., Halpern, C.H., et al. (2016). Wiring and Molecular Features of Prefrontal Ensembles Representing Distinct Experiences. Cell *165*, 1776–1788.

York, D.H. (1973). Motor responses induced by stimulation of the substantia nigra. Exp. Neurol. *41*, 323–330.

Zahrt, J., Taylor, J.R., Mathew, R.G., and Arnsten, A.F. (1997). Supranormal stimulation of D1 dopamine receptors in the rodent prefrontal cortex impairs spatial working memory performance. J. Neurosci. Off. J. Soc. Neurosci. *17*, 8528–8535.

Zhang, H., and Sulzer, D. (2004). Frequency-dependent modulation of dopamine release by nicotine. Nat. Neurosci. *7*, 581–582.

Zhang, S.P., Bandler, R., and Carrive, P. (1990). Flight and immobility evoked by excitatory amino acid microinjection within distinct parts of the subtentorial midbrain periaqueductal gray of the cat. Brain Res. *520*, 73–82.

Zhang, Z.-W., Burke, M.W., Calakos, N., Beaulieu, J.-M., and Vaucher, E. (2010). Confocal Analysis of Cholinergic and Dopaminergic Inputs onto Pyramidal Cells in the Prefrontal Cortex of Rodents. Front. Neuroanat. *4*, 21.

Zhou, P., Resendez, S.L., Rodriguez-Romaguera, J., Jimenez, J.C., Neufeld, S.Q., Giovannucci, A., Friedrich, J., Pnevmatikakis, E.A., Stuber, G.D., Hen, R., et al. (2018). Efficient and accurate extraction of in vivo calcium signals from microendoscopic video data. ELife *7*.